The University of Nottingham

Confocal Raman imaging of live cells

by Alina Zoladek

Thesis submitted to the University of Nottingham

for the degree of Doctor of Philosophy

July 2011

School of Physics and Astronomy

"I have had my results for a long time: but I do not yet know how I am to arrive at them"

Carl Friedrich Gauss (1777–1855)

Abstract

The objective of this thesis is to present the development of Raman microscopy for biochemical imaging of living cells. The main aim was to construct a Raman micro-spectrometer with the ability to perform time-course spectral measurements for the non-invasive study of biochemical processes in individual cells. The work can be divided into two parts: first, the development and characterization of the instrument; and second, completion of two experiments that demonstrate the suitability of Raman technique for studies of live cells. Instrumental development includes the design of optics and software for automated measurement. The experiments involve data collection and development of mathematical methods for analysis of the data.

Chapter One provides an overview of techniques used in cell biology, with a special focus on Raman spectroscopy. It also highlights the importance of experiments on living cells, especially at the single cell level. Chapter Two explains the theoretical background of Raman spectroscopy. Furthermore, it presents the Raman spectroscopy techniques suitable for cell and biological studies. Chapter Three details the instrumentation and software development. The main parts of the confocal Raman micro-spectrometer, as designed for studying living cells, are: inverted microscope, 785 nm laser and high quality optics, environmental enclosure for maintaining physiological conditions during measurements of cells, and fluorescence wide-field microscopy facility for validation and confirmation of biochemical findings by Raman studies. Chapter Four focuses on the evaluation of the performance of the Raman setup and explains calibration and analysis methods applied to the data. Chapter Five and Six describe experiments performed on living cells. Chapter Five focuses on studies of the immunological synapse formed between primary dendritic and T cells indicating the polarisation of actin. Chapter Six describes time-course experiment performed on cancerous cells in the early phases of the apoptosis process, which enabled detection of the DNA condensation and accumulation of unsaturated lipids. Chapter Seven summarizes the work and gives concluding remarks.

List of publication

A. Zoladek, R. Johal, S. Garcia-Nieto, F. Pascut, K. Shakesheff, A. Ghaemmaghami and I. Notingher, "Label-free molecular imaging of immunological synapse between dendritic and T-cells by Raman micro-spectroscopy", *Analyst*, 2010, in press, published online: 18 October 2010

A. Zoladek, F. Pascut, P. Patel and I. Notingher, "Non-Invasive Time-Course Imaging of Apoptotic Cells by Confocal Raman Micro-Spectroscopy", *Journal of Raman Spectroscopy*, 2010, in press, published online: 24 June 2010

A. Zoladek, F. Pascut, P. Patel and I. Notingher, "Development of Raman Imaging System for time-course imaging of single living cells", *Spectroscopy* 24, 2010, 131-136

M. Larraona-Puy, A.Ghita, **A. Zoladek**, W. Perkins, S. Varma, I. H. Leach, A. A. Koloydenko, H. Williams and I. Notingher, "Discrimination between basal cell carcinoma and hair follicles in skin tissue sections by Raman micro-spectroscopy", *Journal of Molecular Structure*, submitted August 2010.

M. Larraona-Puy, A. Ghita, **A. Zoladek**, W. Perkins, S. Varma, I. H. Leach, A. A. Koloydenko, H. Williams, and I. Notingher, "Development of Raman microspectroscopy for automated detection and imaging of basal cell carcinoma", *Journal of Biomedical Optics* 14(5), 2009

M. L. Mather, S. P. Morgan, D. E. Morris, Q. Zhu, J. Kee, **A. Zoladek**, J. A. Crowe, I. Notingher, D. J. Williams, and P. A. Johnson, "Raman spectroscopy and rotating orthogonal polarization imaging for non-destructive tracking of collagen deposition in tissue engineered skin and tendon", *Proc. SPIE 7179*, 2009

S. Verrier, **A. Zoladek**, I. Notingher, "Raman micro-spectroscopy as a non-invasive cell viability test", in: *Methods in Molecular Biology*, edited by: M. Stoddart, Springer: New York, in press (to be published early 2011)

Acknowledgments

There are a number of people who deserve thanks for their help and support throughout my time here. Firstly, I would like to thank my supervisor Dr Ioan Notingher for his help all the way through this project. Next, I wanted to thank members of our little "Raman group": Claire, Marta, Adrian, Banyat and Cristian for their help throughout. I would also like to mention the school's technical support team, without their help the development of the experimental apparatus would not be possible. Appreciations also go to Prof. Poulam Patel, Dr Ramneek Johal, Dr Samuel Garcia-Nieto and Dr Amir Ghaemmaghami for their patience when explaining biological aspects and work over the years.

I would also like to thank my friends in the department, past and present, who have helped in their own way and make my time here more enjoyable, Matt, Karina, Marta W, Alex, Rich, Luis, Adam, Andy P, Andy S., James and Pete. Further, I would like to thank to Magda, Paweł and Ania for their friendship and support throughout.

Last but not least, I would like to thank Szczepan for a helping hand and always being there for me, and my family – Mum, Dad, and Leszek, for their continuous support and encouragement.

Dedicated to my Dad

Contents

List of figures

Chapter 1.

Research background

"Everything that living things do can be understood in terms of the jiggling and wiggling of atoms"

Richard Feynman (1918-1988)

In this chapter the need for experiments on living cells is disputed and an outline the thesis provided. Further, a broad overview of the techniques used in cell studies is presented together with a literature review on Raman spectroscopy for cell studies.

1.1 Introduction

Cells are the elemental units of life and studies linking cellular biochemistry and biological activity of cells are crucial to understanding biological systems. Many cell based assays have been developed to access specific information, but they are based on averaged data over large cell populations. Nevertheless, it is well known that even in the same type of cells variability exists between individual specimens. Therefore, in recent years much emphasis has been put on the analysis of individual cells. In addition, variation in biochemical or physiological characteristics such as the presence, state or activity of particular components is often time dependent, therefore there is a need for easily applicable methods for time course experiments whereby discrete and dynamic events in living cells can be observed.

Conventional label-free microscopy techniques (e.g., phase-contrast, dark field) can provide morphological information about cells over extended periods of time. However, these techniques lack the chemical specificity needed for understanding molecular processes. The majority of techniques available for molecular imaging of individual cells provide only single snap-shots because of the invasive procedures they require. Molecular specific techniques based on antibody conjugation (e.g., fluorescence imaging), require cell fixation as most molecules of interest are found inside the cell. Transgenic strategies to express markers, such as green fluorescent protein, from specific promoters have been recently developed; however, genetic manipulation of cells requires laborious protocols and may interfere with the normal behaviour of cells. In addition, fluorescence imaging is not a quantitative method because it relies on measurements of emission intensity, which suffers from high variability related to preparation protocols or photo-bleaching.

The most promising techniques for time-course measurements of living cells are Raman-based probes. Raman spectroscopy is based on inelastic scattering of light by vibrating molecules. It can be used for a wide range of applications: pharmaceuticals, forensic science and material characterisation. Raman-based techniques are well suited for studying live cells as they are non-invasive and water solutions (buffers and culture media) do not interfere with experiments. Thus, there is no need for cell labelling or other cell modification prior to measurements.

The major aim of the work described in this thesis is to study the biochemical processes in living cells in real time by Raman micro-spectroscopy mapping and to adapt this spectroscopic method for cell biology studies. Development of a novel inverted Raman micro-spectrometer with the ability to perform multi-hour spectral measurements on living cells is presented. This system combines a confocal Raman micro-spectrometer and fluorescence microscope with a cell incubator enclosure allowing measurement of cells over an extended time period. The work is divided into two parts. The first part concerns the instrumental development of the spectrometer, which includes design and alignment of all parts of the spectrometer, and software development for instrument automation. The second part involves performing two different experiments to illustrate the feasibility of this Raman micro-spectroscopy system for *in vitro* studies of cells. These were studies of interactions of white blood cells (T-cells and dendritic cells) during immunological synapse formation and lengthen in time experiment on cancerous cells (MDA-MB-231) which undergo drug-induced apoptosis.

In addition, an extensive overview on techniques used in cell studies is presented in this chapter, emphasising the need for experiments on living cells. A literature review on Raman spectroscopy for cell studies is also provided. Chapter 2 explains the theoretical background of Raman spectrometry. Chapter 3 gives details on instrumentation and setup of the Raman system optimised for live cell studies. This also includes software development. Chapter 4 explains performance characterisation of the system, calibration and analysis methods applied to the spectral data. Next, chapters 5 and 6 show details of experiments performed. Chapter 7 summarizes the work and gives details on possible future research directions.

1.2 Techniques to study cells

1.2.1 Cells – basic knowledge

The cell is the structural and functional unit of all living organisms. Each cell is somewhat self-maintaining; it can take nutrients and convert them into energy, carry out specialized functions and reproduce. Nearly all diseases start from cellular abnormalities that originated in biochemical

intracellular changes. Cell cycle dynamics are closely related in all aspects of health and disease, and have justly received vital attention in biomedical research [1].

Cells are enclosed in a cell membrane made from a phospholipid bilayer, which separates the interior of a cell from its environment. It acts as a semi-permeable barrier, allowing some chemicals to pass in or out of the cell while blocking others, and also maintains the electrical potential of the cell. Inside the cell most of its volume is taken up by the cytoplasm in which organelles are arranged. The most important organelle is the nucleus, where DNA (deoxyribonucleic acid) is located and RNA (ribonucleic acid) is transcribed. The nucleus controls all cellular activities. Other important sub-cellular components are mitochondria, which converts nutrients into usable energy by ATP (adenosine triphosphate) production; the endoplasmic reticulum (ER), which is important for protein synthesis; ribosomes, where the RNA translates into proteins; the Golgi apparatus, where proteins and other molecules are prepared for transport outside of the cell, and the cytoskeleton, which is built of actin and other protein filaments inside the cell, giving it its shape [1, 2] .

The shapes of living cells, even from the same species, are quite varied. Some cells, such as neurons, are long and others, such as T-cells are quite round. The size of cells is also related to their functions [2].

Tissues are a collection of cells with specialized functions that are similar morphologically and which produce similar intercellular substances. Usually there are a few specific types of cells within a tissue. There are four basic types of tissue: muscle, nerve, epidermal (e.g. dermis), and connective (e.g. bones). Specific tissues working together as a unit are components of body organs, which performs functions that none of the component tissues can perform alone. This cooperative interaction of different tissues is a basic feature of animals. The heart, eye or skin are examples of organs [2, 3].

Knowledge of cell components and how cells work is fundamental to all biological sciences. Understanding the similarities and differences between cell types is particularly important to a

number of biological fields including fundamental cell biology, medical imaging, tissue engineering and pharmacology. *In vitro* testing of new pharmaceuticals is an important stage in drug development, required prior to *in vivo* animal testing [4]. Changes in cell cycle induced by drugs are routinely investigated to aid in pharmaceutical development, including identification of anti-cancer agents which disrupt cell cycle mechanisms. Testing aims to establish the efficacy of the drugs but also to identify any toxic effects on cells [5]. The study of single cell behaviour in a specified chemical or biological environment holds important significance in the development of cell-based sensors, as it reveals a range of responses from each individual cell under stimulation [5, 6].

1.2.2 Common techniques in cell studies

There are many techniques to study cells [7], including a few well established optical microscopy techniques, such as dark field, phase contrast and confocal microscopy. Evanescent wave techniques are a novel approach to increase resolution normally restricted by the diffraction limit in normal optical approaches. Total internal reflectance microscopy (TIRM) and near-field scanning microscopy (NSOM) are examples of this. The optical microscopy techniques usually allow time-course and even video measurements of cells as usually they are non-invasive. However, they provide information only on the sample layout and no chemical information can be obtained.

The fundamental difference between near-field and conventional optical microscopy is the size and depth of the area that is illuminated, which is within a few tens of nanometres. The principal components of an NSOM setup are the light source, which is focused into a single mode optical fiber, the nanometer-sized scanning tip, the feedback mechanism, the detector, and the piezoelectric sample stage, to sense and record interactions within the sample. The scanning tip, which is the illuminating source, is usually a stretched optical fibre coated with metal or just a standard atomic force microscopy (AFM) cantilever with a hole in the middle; the radius of the tip has to be less than one-third of the imaging light wavelength. In NSOM, a necessary condition is that the tip is closer to the specimen than the wavelength of the illuminating radiation, so that the light propagation is evanescent and parallel to the specimen surface. This method is usually combined

together with other techniques, like AFM, fluorescence or Raman spectroscopy, to enhance information obtained from cells [8]. NSOM has typically been limited to specimens that are accessible by a local probe. It has a very low working distance and shallow depth of field and is therefore limited to studying surfaces [8, 9].

A variety of electron microscopes, in which a beam of electrons is used to illuminate a sample, are employed in cell biology studies. Electron microscopes have much greater resolving power than light microscopes, as the wavelength of an electron beam can be much smaller than that of an optical photon. Transmission electron microscope (TEM) has been used to study lipid vesicles in animal cells [10] or cell-substrate interactions [11] and the scanning electron microscope (SEM) has been used to study cell proliferation on various materials [12].The main drawbacks of electron microscopy techniques are that they require special sample preparations. The sample has to be conductive, therefore biological species under investigation are usually coated with gold. For TEM the sample has to be very thin and sectioning of cells has to be applied, and in most cases, samples have to be viewed in vacuum [13].

The study of mechanical behaviour and responses to physical stimulus by cells are important for building up tissue models and understanding better cellular processes such as guiding and managing adhesion, differentiation or cell motility [14]. Cell biomechanics can be studied by various techniques including cell-cell and cell-substrate contact and deformation, optical stretching, magnetic traps and AFM. Optical tweezers or traps are an essential tool to immobilize animal or bacterial cells in suspensions. Combined with other methods this allows manipulation or even 'micro-surgery' of living cells [9, 15].

1.2.3 Molecular specificity in cell measurements

The methods mentioned above provide a reasonably good picture of the structures inside the cell and of cell mechanics, but do not provide chemical information on the samples. Most of the biological assays currently available for cell chemistry studies rely on techniques such as immunochemistry, which requires the reaction of an antibody (usually fluorophores or enzymes) directed against the protein of interest; western blot which is used to detect specific proteins in a

given sample (proteins are separated from the sample and then probed using antibodies specific to the target); the polymerase chain reaction (PCR) technique, which allows the amplification of specific regions of a DNA strand; transfection, which involves introducing foreign DNA genes into a cell; and cell fractionation, which is the method of separation of cell organelles. These methods are invasive, as they require the use of labels, cell fixation or cell lysis. Experiments are expensive and time consuming and time-course experiments on the same cells cannot be performed. Additionally, the majority of these techniques cannot be applied to single cells and can be performed only in cell suspensions where a vast amount of cells are under investigation, therefore they provide an average information of the cell population [2, 16].

Magnetic resonance imaging (MRI) is a diagnostic technique used mostly in medicine to produce high quality anatomical images of the human body by application of strong magnetic fields and non-ionizing radiation in the radio frequency range. Recent developments in new contrast agents (magnetic nanoparticles) allowed for this technique to be applied to cell studies (CMRI). CMRI can track the temporal and spatial migration of cells labelled with the contrast particles within organs and tissues [17, 18]. Nonetheless, this method could also be used to visualize single cells and their organelles *in vitro* with good resolution [18]. Effects of MRI agents on cell behaviour and proliferation or the homogeneity of labelling among cell populations are still not fully understood and are still under investigation by various research groups.

Fluorescence microscopy is one of the most important research tools in modern cell biology and is routinely used in single cell studies and imaging. In most cases, the component of interest in the cell is specifically labelled with a fluorescent molecule called a fluorophore. The specimen is illuminated with light of a specific wavelength which is absorbed by the fluorophores, and then light is emitted at a longer wavelength. Fluorescence microscopy offers chemically specific contrast, as a vast number of fluorescent labels and quantum dots have been developed to monitor cellular functions and activities. The majority of these labels are non toxic and therefore allow the study of living cells. Optical detection is very fast and various technologies have been implemented for high-throughput screening. Additional information can be obtained by examining polarization

or phase discrimination features. Moreover, imaging can be performed in three dimension by multi-photon excitation [19] or confocal laser scanning [20, 21]. Conventional fluorescence microscopy, as in the widefield and laser scanning confocal spectroscopy techniques mentioned above, rely on illumination of fluorophore-labelled specimens with a broad cone of light. The limited spatial resolution often makes it difficult to differentiate between individual specimen details that are overwhelmed by background fluorescence from outside the focal plane. One approach to selectively illuminate and excite fluorophores in a restricted specimen region is total internal fluorescence microscopy (TIRFM). TIRFM employs the unique properties of induced evanescent waves. The excitation light beam travels at a high incident angle through the solid glass coverslip, where the cells adhere. At a specific critical angle, the beam of light is totally reflected from the glass/water interface, rather than passing through and being refracted. The reflection generates a very thin electromagnetic evanescent field (usually less than 200 nanometers), which has an identical frequency to that of the incident light. Total internal reflection fluorescence can be employed to investigate the interaction of molecules with surfaces; therefore it is well suited for selective visualization of contact regions between individual cells and the substrate. TIRF, with enhanced depth resolution and its remarkable reduction of detection volumes, allows single-molecule detection (e.g. of cellular receptors located in the cell membrane [22]). Novel applications have concentrated on the imaging of exocytosis or endocytosis, measurements of adhesion foci of microtubules, studies of the localization, activity and structural arrangement of specific ion channels and cell membrane dynamics [22-24]. Also NSOM is used together with fluorescence to enhance the resolution of imaged structures (down to 10nm). This method was used, for example, to study ion transport channels in cells [25].

Although the techniques mentioned above are able to detect small changes in cell activity, such as low levels of toxicity, they may need modifications for specific cellular responses. Fluorescence microscopy uses labels so the information obtained depends on the particular bindings of the fluorophores used and molecules of interest. Using artificial labels on cells can be invasive, as they require cell fixation and permeabilisation of membrane. Also there is the problem of photo-toxicity

which could cause cell death. Photo-bleaching and artefacts, due to introducing a fluorescent probe into a cell, may alter the physical and chemical conditions of the cell.

1.2.4 Label free chemical imaging of cells

Optical methods using light in the visible and near-infrared regions are particularly attractive as they enable non-invasive sampling of cells. For example, variations in the intensity of the light emitted by bioluminescent bacteria can be used to detect toxic chemicals such as polycyclic aromatic hydrocarbons and phenols or water pollution [25, 26]. Transgenic strategies to express markers, such as green fluorescent protein, from specific promoters have been also developed [27-29]. However, genetic manipulation of cells requires laborious protocols to be developed to ensure molecular specificity, which may interfere with the normal behaviour of cells. In addition, fluorescence and bioluminescence imaging is not a quantitative method because it relies on measurements of emission intensity, which could suffer from high variability related to preparation protocols or photo-bleaching.

The molecular specificity and sensitivity of imaging mass spectrometry (MS) has been employed for direct mapping and imaging of biomolecules present in cells and tissues. MS is based upon the motion of a charged particle (ions) in an electric or magnetic field to measure the masses and relative concentrations of atoms and molecules. The latest advancement led to development of MS imaging techniques with resolutions suitable for analysis of cell. Scanning microprobe matrix-assisted laser desorption/ionization mass spectroscopy (SMALDI-MS), secondary ion mass spectrometry mass spectroscopy (SIMS) and electrospray ionization mass spectroscopy (ESI-MS) were successfully used for single cell imaging [30-34]. The crucial part of MS imaging is sample handling and preparation. The sample has to be introduced into the ionization source, then obtained ions are separated depending on their mass-to-charge in the analyzer and either the charge induced or the current produced is recorded on the detector. Due to short-life and high reactiveness of ions their formation and manipulation is usually conducted in a vacuum. The method of sample exposition to the ionization source often depends on the method being used, as well as the type and complexity of the sample. Mass spectrometry is a promising method for the characterization of

proteins, oligosaccharides and nucleic acids which are relatively large molecules with high molecular weights [32, 35, 36]. However, precision is dependent on subtle variations in sample preparation, as well as temperature and pressure fluctuations within the mass spectrometer [36]. Besides, this is an invasive technique and cannot be used for time-lapse experiments on live cells.

Recent developments in biomedical vibrational spectroscopy now permit the non-invasive imaging of cells and tissues within both the laboratory and clinical setting [37-39]. In the commonly used infrared absorption spectroscopy, infrared (IR) light excites certain vibrational frequencies of molecules and is absorbed. IR spectroscopy has difficulty with measurements in aqueous solutions because water interacts strongly with the IR radiation, consequently most of the experiments are performed on dry fixed cell samples [9, 40]. IR spectroscopy, and its derivatives like FTIR (Fourier-Transform IR) or IR with synchrotron radiation sources, have been used in cell studies [41] for example the quantification of water in single living cells [42], cell-cycle-dependent variations in spectra of cells [43], and characterization of human corneal stem cells [44]. Although, the spatial resolution achievable is of order a few microns, it is usually too large for cell mapping. In addition, synchrotron radiation is not easily available and is extremely expensive to run [45].

Raman spectroscopy is an analytical technique based on the inelastic scattering of laser photons by molecules, thus providing a fingerprint of the intrinsic chemical composition of a cell without the need for cell labelling or other cell modification. Raman spectra are very specific and can be used for both qualitative and quantitative applications. The main advantage of Raman spectroscopy compared to other techniques is that it has potential for high chemical specificity without sample preparation, damage or contact. Additionally, Raman spectrum is not specific to only one chemical, but all components within the sample. The technique is well suited for studying live cells as water solutions (buffers and culture media) do not interfere with experiments and cells can be analysed without causing cell damage [46, 47].

1.3 Raman spectroscopy in cell studies – literature review

Raman spectra are very specific and can be used for both qualitative and quantitative applications. Thus, Raman spectroscopy has been applied to a number of various fields, including analytical chemistry, material science, geology, etc [48, 49]. There are a number of applications in forensic science and police investigations, e.g. for drug recognitions [50], art history and cultural preservation for paint identification [51], and archaeology (i.e. it was used for the analysis of historical specimens like the hair of Isaac Newton [52] and the mummified skin of an Iceman [53]).

The use of Raman spectroscopy for biomedical applications has grown significantly in the recent years. Its attractiveness comes from the ability to provide quantitative information about the biochemical and morphological states of cells and tissues, as a Raman spectrum represents a "chemical fingerprint" of the measured sample, in a minimally invasive or non-invasive manner and with almost no sample preparation. However, despite the rich chemical information content, Raman spectroscopy is not yet widely used in cell biology studies. This is mostly due to the fact that the Raman signal is inherently weak because of the small cross section of the transitions involved. With modern instruments, concentrations of approximately 10^{-3} M can be detected but a long acquisition time is required, which makes the procedure more difficult to apply in real-time investigations [49]. In the beginning there was a substantial scepticism that Raman signals could be observed at levels of laser power that would not produce severe tissue and cell damage. Powerful lasers focused on microscale areas led to increases in temperature in most tissues. As most biomolecules exhibit a minimum absorption of light in the NIR domain, using an excitation wavelength in this region will minimize the risks of sample heating and/or photochemical interactions [39, 54]. Therefore, since the development of high-power near-infrared lasers, 785 nm lasers have become an attractive choice for Raman spectroscopy of cells and tissues. While visible lasers induce cell death even at low laser powers and short exposure time, there is evidence that 785 nm does not induce cell damage in this power range and exposure times typical to Raman spectral imaging [55, 56]. Most cell types and other biological materials exhibit strong fluorescence background, which could cover the Raman peaks. The use of the 785 nm laser wavelength avoids

or greatly reduces the fluorescence excitation, which allows strong Raman signals of cells to be obtained [46, 49, 57].

The Raman spectrum of a cell is a complex superposition of spectra from all of the molecules exposed to laser illumination. In most cases it is not possible to assign peaks in the spectrum to particular biochemical components. Nevertheless, Raman spectra can still be used as highly specific spectroscopic fingerprints, enabling the identification of cells. Cells of different type or in different morphological states will vary in their overall molecular composition. Raman spectra reveal the overall molecular composition, and so spectra will differ depending on the concentration of the molecules. Pathological changes in molecular composition or structure are reflected in the spectra, enabling development of diagnostic tools based on Raman spectroscopy [58-60].

Although interesting spectral information has been obtained from suspensions of cells [61], single cell spectra offer important information concerning specific biological functions, cellular interactions with their microenvironment (with other cells, drugs, biomaterials etc.), as well as variation within a population. Raman micro-spectroscopy has been used to examine single fixed [62, 63], dried [64], cytospun [65] and living cells [42, 66-68] grown or deposited on an appropriate "Raman-transparent" substrates (usually MgF_2 or CaF_2 slides). Recent reports showed the capability of Raman microscopy to study nucleic acids in cells under different conditions [61, 67], sense molecular changes during cell death [69-72], study the interaction of cells with toxic agents [67, 73], mark differences between active and non active T-lymphocytes [74], classify eukaryotic and bacterial cells [47, 62, 75, 76], and study plant cells [77]. A combination of optical tweezers and Raman micro-spectroscopy was used to determine the biochemistry of individual bacteria [63] and red blood cells in suspension [15, 78]. Biochemical variations in virus infected cells trapped optically [79] and acoustically [80] are also under investigation. This setup has potential for the examination of drug-cell interactions [81], and cell response to mechanical stress. Composite scaffold materials for cell growth [82] or collagen-carbon nanotubes for tissue engineering [83] were also investigated.

The majority of the work presented above was completed on only one or a few different points in the cell. This method reveals some information about biochemical composition but does not provide information on spatial distribution. In addition, the information could be misleading as the biochemistry of cells is not uniform and different points in the cell will differ from each other. For that reason a new approach in Raman spectroscopy, which gives better understanding of cellular changes is spectral mapping, also called hyperspectral imaging. The ability to accomplish Raman micro-spectroscopy mapping allows a much better understanding of the biochemistry and morphology of specimens under investigation.

Spectral images are constructed from several point spectra collected at different spatial positions within a cell. A spectrum is collected at each pixel by moving the sample typically in a raster pattern with small step increments. Commonly, a collection of hundreds or thousands of spectra is required to completely characterize a cellular system. The laser can be focused to a diffraction-limited spot size (usually ~1 μm), and at such a high spatial resolution, spectra of subcellular organelles can be obtained with features dominated by a single biochemical component. The number of spectra required to image the cell depends upon the resolution required (this is stepsize between every measurement point), number of spectra required per cell (which depends on cell type, morphology and size) and on the integration time of each spectrum. Spectra from different cellular locations can be averaged to generate a spectral biochemical representation of the cell revealing the structure and arrangement of subcellular organelles, and can provide insight into cellular biochemical dynamics [69, 84, 85].

Taking advantage of the high-spatial resolution of optical microscopes, Raman spectral imaging has been used for imaging cell organelles like mitochondria [86], lipid droplets [87] the nucleus [88], distribution of various molecules in eukaryotic cells [69] and reaction of cells to drugs [85, 89].

Furthermore, multiplexed Raman imaging with specifically prepared nanotubes from different carbon isotopes was reported as an alternative method to fluorescence labelling of certain receptors

[90]. Hybrid confocal Raman and fluorescence microscopes using quantum dots as a fluorescent label was also considered to study the biochemistry of single cells [91].

However, the above mentioned studies were carried out on fixed cells (which are chemically preserved for the investigation). Fixing and drying can introduce artefacts which distort Raman spectra, potentially obscuring both qualitative and quantitative analytical results [92-94]. In addition, fixing the cells does not allow time-lapse measurements of cellular events. Therefore Raman imaging studies on living cells is the best solution. Although it could be difficult to perform experiments in good conditions to maintain cell viability for extended periods of time during measurements (i.e. temperature and CO_2 level, avoiding contamination).

Recent studies reported Raman mapping on living cells. Preliminary study of imaging live lung cancer cells with 2 μm stepsize and acquisition time of 10 s at every point was reported [95], giving a total acquisition time of 50 minutes for a single cell. A dependence of the delivery ability of nanotubes was observed upon probing the interaction of SWNTs with single living T- cells by micro-Raman spectroscopic imaging [96]. However, the nanotubes were used as Raman labels with relatively strong Raman signal in comparison to signal from cell itself. The new confocal Raman fast slit scanning imaging method with visible 532 nm laser was considered for investigating drug interaction with living cells [97, 98] with single cell time acquisition of less than 5 minutes. Spectral time-course imaging of living HeLa cells within a 20 minutes time span was performed [99]. A laser light in the visible range was also used for studies of phenotypic heterogeneity of live microbial populations [100]. Confocal Raman spectroscopy was used to investigate the effect of ultraviolet radiation on human sperm cells [101]. Although the Raman imaging of live cells in the studies presented above was not established in cell culture growth media, but on dried cells or cells in buffer solutions (e.g. PBS or DMSO), which maintain cells alive even for few hours but they do not provide condition for normal cells growth. Recently, the development of microbioreactors for Raman microscopy examination of human bone marrow stromal cells was presented. The potential of the cells being monitored non-invasively during proliferation, differentiation, and development into tissues was demonstrated [102].

Raman spectroscopy has a number of advantages over other analytical techniques to study cells, even though the Raman effect is a very weak process, making it difficult to measure low concentrations of a substance and it can be swamped by fluorescence. Due to its ability in studying samples at the micro- and nanoscale level in real time and its non-destructiveness to biological samples, the use of Raman micro-spectroscopy remains a growing interest in cell biology research. Raman spectroscopy can work on cells in aqueous solutions (contrary to other cell-biology techniques, e.g. IR spectroscopy) with no special sample preparation needed. There are various Raman spectroscopy techniques which are suitable to study certain information. This literature review was focused on Raman microscopy and Raman confocal microscopy. Other Raman effect based techniques which were used for cell measurements will be discussed briefly at the end of the next chapter.

Since Raman spectroscopy methods have been used for many years there are a number of recent excellent reviews of Raman spectroscopy as a tool in life science and biomedical research [46, 47, 103-108].

The objective of this thesis is to present the development of Raman microscopy for biochemical imaging of living cells. The work has been motivated in part by the increasing interest in label-free chemical imaging of individual live cells. In particular, the investigation focused on the spectral imaging of live cells in their physiological conditions over extended time periods. The main aim of this thesis has been the development of a dedicated confocal Raman micro-spectrometer for high resolution non-invasive chemical imaging of biochemical processes in individual cells. The instrument overcome the main limitations of commercial systems and enabled two different detailed studies on live cells and integration of the fluorescence imaging system made it possible to confirm the Raman findings and check viability of cells after laser irradiation. The pro-longed measurements of cells were established by imaging of junctions between two types of primary cells from blood and time-course experiment over few hours was showed for the first time on cancerous cells undergoing apoptosis process.

Chapter 2.

Raman spectroscopy

"It is the theory that decides what we can observe"

Albert Einstein (1879 - 1955)

Raman spectroscopy is an optical technique used to study vibrational, rotational and other low-frequency vibrations of molecules. It relies on the inelastic scattering of monochromatic light when it interacts with matter and has become an important analytical tool for scientific research.

In this chapter a theoretical background of Raman spectrometry will be given together with an introduction of different types of Raman spectroscopy which potentially could be used for the study of cells.

2.1 History of Raman spectroscopy

The technique of Raman spectroscopy was discovered more than 80 years ago. It was predicted by Adolf G. Smekal in 1923, although it was not observed until February 1928. Experimental evidence of the phenomenon was first reported by Professor Chandrasekhra V. Raman and his co-worker Kariamanickam S. Krishnan from Calcutta [59]. Later, the same year, it was also reported independently by Grigory Landsberg and Leonid Mandelstam in Moscow [49, 59].

The first Raman "instrument" used monochromatic sunlight (produced using a narrow band photographic filter) as a light source, a 'crossed' filter to block scattered light, and the human eye as a detector. C.V. Raman and K. S. Krishnan found that, when a benzene sample was irradiated by this intense monochromatic light source, light of changed frequency passed through the crossed filter. [49, 58, 59]

It was instantly clear that this discovery was one of great importance. The explanation of this new radiation gave a further proof of the quantum nature of light, as it requires the use of photons and their change in energy as they interacted with the atoms in a particular molecule. In 1928, in a lecture about a new type of light scattering, Professor Raman said: *"We are obviously at the fringe of a fascinating new region of experimental research, which promises to throw light on diverse problems relating to radiation and wave theory, X-ray optics, atomic and molecular spectra, fluorescence and scattering, thermodynamics and chemistry. It all remains to be worked out"* [109]. The phenomenon was called the 'Raman effect' and for this discovery Raman received the Nobel Prize in Physics in 1930 [49, 59].

A systematic theory of the Raman Effect was developed by Czech physicist George Placzek between 1930 and 1934. His pioneering work provided a quantum formulation of Raman light scattering [110].

The Raman Effect was the subject of intensive research in the first decade after its discovery. However, activity in this field decreased sharply after World War II in favour of infrared spectroscopy. Raman spectroscopy could no longer compete with infrared spectroscopy as a

routine analytical tool. During the war, infrared spectroscopy was enhanced by the development of sensitive detectors and advances in electronics, while improvement in Raman measurements had to wait until the discovery of the laser [49, 111].

The gradual development of Raman spectroscopy instrumentation focused on improving light sources, wavelength selectors and optical filters, and detectors for the scattered light. In the 1930s, after experimentations with helium, lead and zinc lamps, the mercury arc lamp became the major light excitation source for Raman studies. From 1962 lasers were introduced to Raman spectroscopy as a convenient, high quality source of light. Gas lasers became popular and more recently good quality diode-lasers and solid state lasers have been used for Raman spectroscopy [37, 48].

Prism based spectrographs were used as wavelength selectors in early Raman instrumentation. Developments began with the use of a single monochromator, followed by the use of double and triple monochromators. In 1968 holographic gratings appeared, adding efficiency in the collection of Raman scattering to commercial Raman instruments. Currently the most popular wavelength selector is a Czerny-Turner spectrograph with holographic or ruled gratings [48, 111].

Early in the development of Raman systems detection of light was performed with photographic plates, using long exposure times (tens of hours or even days). In the late 1930's the introduction of photomultiplier tubes (PMT), which convert entering photons into an electric signal, offered an alternative to the photographic plate. In early Raman spectrometers the Raman signal was detected separately for each frequency. This time-consuming single-channel technique was eventually superseded by multiple-channel detection and more lately by simultaneous detection across a wide frequency range using charge-coupled devices (CCDs) [9, 59]. Recent advancement in CCD technologies allows detection of photons in the near infrared with high sensitivity and relatively low dark current noise [111].

In the late 1950s, the first methods for interpreting vibrational spectra of model biomolecules were developed and detailed studies on structure correlations in Raman spectroscopy were reported.

Today, as described in Chapter 1, Raman spectroscopy has become a well-established technique with widespread applications in many fields especially biochemical and medical research [9, 48, 58].

2.2 Theory of the Raman effect

When monochromatic radiation is incident upon a sample this light will interact with the sample in some fashion; it may be reflected, absorbed or scattered. In quantum mechanics the scattering is described as an excitation to a virtual (or forbidden) state lower in energy than a real electronic transition with nearly immediate de-excitation (it occurs in 10^{-14} seconds or less) [9, 48]. Figure 2-1, known as a Jablonski diagram, illustrates electronic and vibrational energy levels of a molecule and transitions between the excited and the ground state.

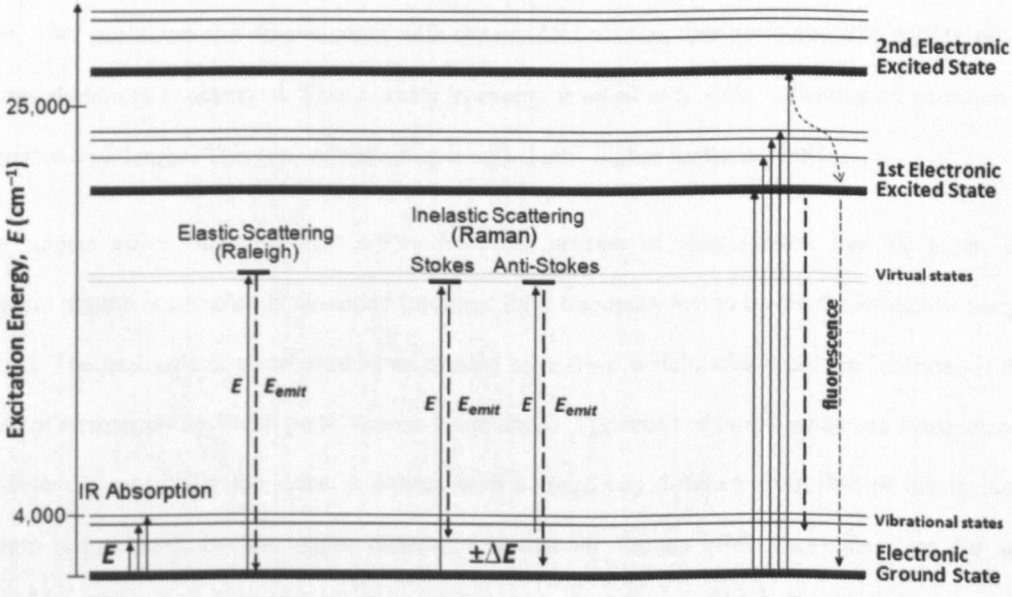

Figure 2-1. Jablonski energy diagram of electronic energy transitions (adapted after [112]).

The basic theory of Raman Spectroscopy comes from the principle of the inelastic scattering of light (Raman scattering) as opposed to elastic scattering of light (Rayleigh scattering). Most of the scattered light has the same frequency as the incident light, hence it experience the Rayleigh scatter phenomenon, where there is no change in energy. Elastically scattered photons have the same energy as the light source, which could be expressed as:

$$E = hv \qquad \text{Equation 2-1}$$

where υ is the frequency of the laser light and h is Planck's constant.

However, a small part of the incoming radiation (approximately ~1 x 10^{-7} of the scattered light) is scattered inelastically. This inelastic scattering is known as Raman scattering. In this case photons are scattered from molecules with frequencies different from and usually lower than the frequency of the incident photons. If the molecule is excited from its ground state to the forbidden or virtual state and then relaxes back and finishes on the first vibrational level of the ground state then an energy difference ΔE is lost from the initial energy of the light source giving a scattered photon energy equal to $E - \Delta E$. Since this energy is smaller, the wavelength of the scattered light is longer and this process is known as Stokes emissions. If, however, the molecule starts in the first vibrational level of the ground electronic state when it is irradiated and drops back onto the ground state, after excitation and de-excitation with the incident photon, then an increase in energy of the scattered photons is observed. This increase in energy is equal to $E + \Delta E$ indicating an emission of a shorter wavelength. This type of transition is called anti-Stokes scattering [48]

The Raman effect fundamentally differs from the process of fluorescence. For the latter, the incident photon is completely absorbed (incident light frequency has to match the available energy states). The molecule is transferred to an excited state from which, after a certain lifetime (of the order of nanoseconds), it can go to various lower states. The result of both Raman and fluorescence processes is essentially the same: a photon with a frequency different from that of the incident photon is produced, but the major difference is that the Raman effect can take place for any frequency of the incident light and it occurs immediately [48, 49].

In general at room temperature Rayleigh scattering is ~10^6 times more intense than Stokes and anti-Stokes scattering [113]. Stokes lines are usually more intense than anti-Stokes lines due to a higher population of the lowest ground state compared to the population of the first vibrational level of the lowest ground state. The ratio of anti-Stokes to Stokes lines increases with temperature as according to Boltzmann population of states, molecules appear in the first vibrational level of the

ground state more often. Anti-Stokes scattering has the advantage over Stokes scattering in that it is not affected by florescence. Despite this fact it is the Stokes shift which is most often observed in Raman spectroscopy as at room temperatures more photons undergo Stokes scattering [48, 114, 115].

Moreover, as shown schematically in Figure 2-2, the scattered radiation occurs over all directions. It also has observable changes in its polarization along with its wavelength [37, 48].

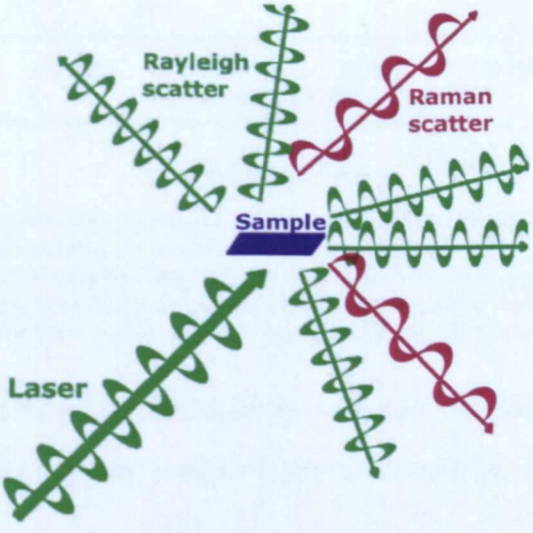

Figure 2-2. Schematic illustration of scattering, which occurs in all directions from the sample.

The frequency differences between the excitation radiation and the Raman scattered radiation is known as the Raman shift. Raman shifts are reported in units of wavenumber (cm^{-1}) and are defined by:

$$\Delta(cm^{-1}) = 10^{-7}\left(\frac{1}{\lambda_0} - \frac{1}{\lambda_R}\right) \qquad \textbf{Equation 2-2}$$

where Δ is the Raman Shift, λ_o is the laser wavelength, and λ_R is the Raman radiation wavelength in nanometres. These units are very useful as they do not dependent on excitation source – this means that the spectra collected with different wavelength excitation sources can be easily compared [48].

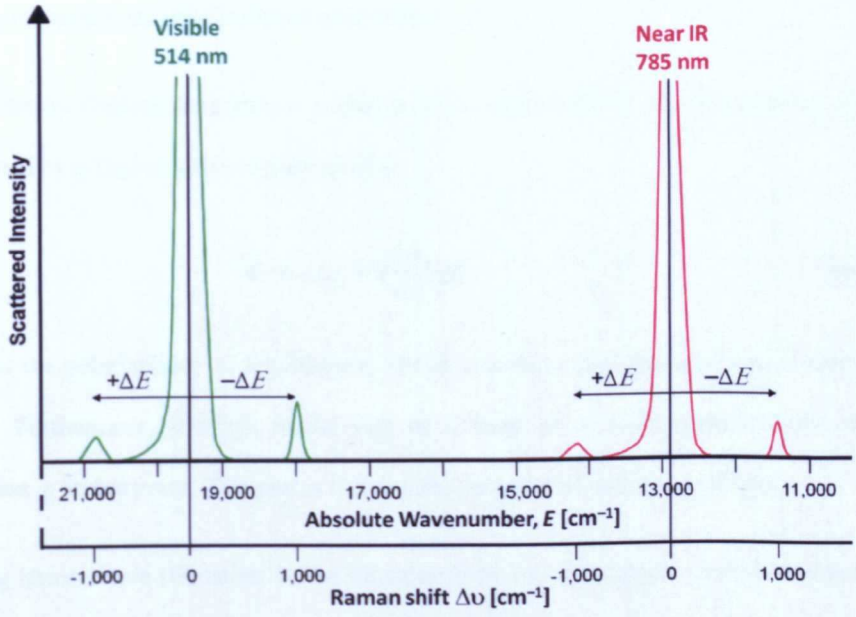

Figure 2-3. Schematic representation of two Raman spectra excited with the green 514 nm and 785 nm laser lines. In the example spectrum, notice that the Stokes and anti-Stokes lines are equally displaced from the Rayleigh line. This occurs because in either case one vibrational quantum of energy is gained or lost. Also, note that the anti-Stokes line is much less intense than the Stokes line and that the spectrum excited with visible laser is more intense than the NIR one (adapted after [112]).

Classically, Raman scattering can be explained as the interaction of the electromagnetic field of the incident radiation, $\boldsymbol{E}$, with a molecule. Consider the incident electric field of the laser light as:

$$\boldsymbol{E} = \boldsymbol{E_0}\cos(2\pi\nu_0 t) \qquad \textbf{Equation 2-3}$$

where ν_0 is the frequency of the laser light and $\boldsymbol{E_0}$ is the electric field magnitude.

The incident electric field induces an electric dipole moment, $\boldsymbol{P}$, in the molecule:

$$\boldsymbol{P} = \alpha\boldsymbol{E} \qquad \textbf{Equation 2-4}$$

Molecular polarizability α may be interpreted as the deformability of the electron cloud by the external electric field. In general, α is a tensor and depends on the electric field $\boldsymbol{E}$. However, for simplicity the tensor properties of α are neglected here.

Charge distribution in the material oscillates at some frequency, ν, about their equilibrium positions:

$$q = q_0\cos(2\pi\nu t) \qquad \textbf{Equation 2-5}$$

where q_0 is the amplitude of vibrational oscillations.

However, the oscillations may induce a change in the polarizability of the molecule; this can be approximated by a Taylor series expansion of α:

$$\alpha = \alpha_0 + (\frac{\partial \alpha}{\partial q})_0 q \qquad \text{Equation 2-6}$$

where α_0 is the polarizability at equilibrium, which is a static part that produces elastic Rayleigh scattering. Furthermore, $(\partial\alpha/\partial q)_0$ is the rate of change of α with respect to the oscillating displacement q at this point. This part is responsible for inelastic scattering of light.

Combining terms above (Equation 2-3 to Equation 2-6) and simplifying (owing to: $\cos\alpha\cos\beta = [cos(\alpha-\beta) + cos(\alpha+\beta)]/2$) gives:

$$\boldsymbol{P} = \alpha_0 \boldsymbol{E_0} \cos(2\pi t v_0) + \frac{1}{2}(\frac{\partial \alpha}{\partial q})_0 q_0 \boldsymbol{E_0}[\cos\{2\pi t(v_0 - v)\} + \cos\{2\pi t(v_0 + v)\}]$$

Equation 2-7

This demonstrates that light will be scattered at three distinguished frequencies. The first of these terms represents Rayleigh scattering, which is the same frequency as the incident light, v_0 and has a magnitude proportional to α_0. The second term corresponds to Raman scattering – inelastically scattered light which contains two frequency shifts: Stokes, which occurs at $(v_0 - v)$ and anti-Stokes Raman scattering at $(v_0 + v)$ [49, 114, 116].

2.3 Vibrational spectroscopy - selection rules

As a tool for characterization of chemical composition Raman spectroscopy is closely related to infrared (IR) spectroscopy. IR and Raman spectroscopy both measure the vibrational energies of molecules. In IR absorption spectroscopy the molecule absorbs light of a specific frequency that corresponds to the vibrational excitation. In Raman scattering the vibrating group in the molecule interacts with light. IR adsorption and Raman spectroscopy are complementary techniques, however they only yield a partial description of the internal vibrational motion of a molecule, as they are governed by different selection rules [48, 49].

A selection rule is a condition restricting the physical properties of the initial and final system that is necessary for a process to occur with a nonzero probability. Molecular vibrations which are accompanied by a change in electric dipole moment can be observed experimentally in the infrared. Raman scattering will only occur when vibrations change the polarizability of a molecule. Figure 2-4 illustrates the Raman active symmetric stretch of the CO_2 molecule as an example. Since there is no change in the dipole moment this vibration is not visible in the IR-spectrum yet it is visible in the Raman spectrum [48, 58].

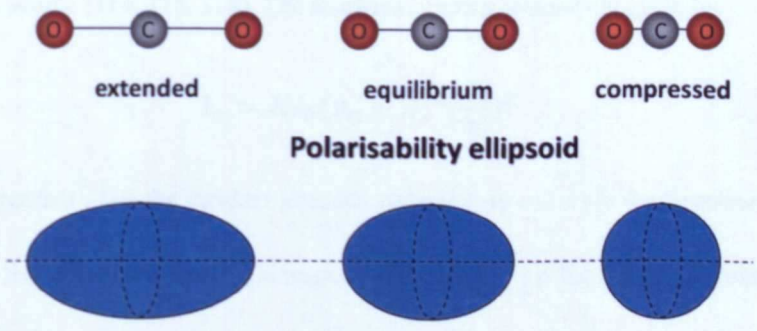

Figure 2-4. Vibrational Raman active symmetric stretch of CO_2 molecule (adapted after [117]).

Accordingly, the selection rule for a molecule to be Raman active is that the rate of change in polarizability must not be zero. The mathematical expression is obtained from the second term of Equation 2-7 and it is represented by the following factor:

$$\left(\frac{\partial \alpha}{\partial q}\right)_0 \neq 0 \qquad \textbf{Equation 2-8}$$

The polarizability depends on how tightly the electrons are bounded to the nuclei. In the symmetric stretch the strength of electron binding is different between the minimum and maximum inter-nuclear distances. Therefore the polarizability changes during the vibration and this vibrational mode scatters Raman light (the vibration is Raman active). In the asymmetric stretch the electrons are more easily polarized in the bond that expands but are less easily polarized in the bond that compresses. There is no overall change in polarizability and the asymmetric stretch is Raman inactive [48, 49, 58].

The polarizability is a function of the shape and size of the molecule. It usually varies with spatial direction and it is independent of any permanent dipole moment. For atoms, where the symmetry is spherical, the polarizability will be the same in all directions and it can be expressed by a scalar quantity. For molecules, the polarizability will not be the same along all directions and therefore it is more accurately expressed as a tensor which takes into account the possible variation in polarization [48, 116].

The intensity of Raman bands depends on the polarizability and also on the power and frequency of the initial light source [114, 115, 118]. The Raman scattering intensity is given by:

$$I_R = KI_0(\nu_0 - \nu)^4(\frac{\partial\alpha}{\partial q})^2 \qquad \textbf{Equation 2-9}$$

where K is a constant , I_0 is the incident intensity radiation, ν_0 and ν are the frequencies of incident laser light and the vibration of molecule respectively, and $\left(\frac{\partial\alpha}{\partial q}\right)$ is the change in polarizability. The value of the constant of proportionality, K, is dependent on the efficiency at which Raman-scattered light may be collected, as well as a number of other factors.

The frequency of molecular vibrations is very small in comparison to the frequency of excitation, i.e. $\nu_0 >> \nu$, hence the term $(\nu_0 - \nu)^4$ can be approximated as ν_0^4 or subsequently as λ_o^{-4}. The Raman signal intensity therefore depends inversely on the fourth power of the incident light wavelength, so that lasers with shorter wavelengths give a stronger Raman signal intensity [49, 114, 118].

The vibrations of a highly polar moiety, such as the O-H bond, are usually weak and for this reason, water is only weakly Raman active and therefore does not interfere with Raman spectroscopy of biological samples measured in aqueous solutions. Highly Raman active molecules contain moieties with distributed electron clouds, such as carbon-carbon double bonds. Bending or stretching the bond changes the distribution of electron density substantially and causes a large change in the induced dipole moment [49].

Vibrational Raman spectroscopy is not only limited to intra-molecular vibrations. Crystal lattice vibrations and other motions (e.g. rotational) are also Raman active. Figure 2-5 shows an example of the difference in Raman spectra due to crystal lattice vibrations [58, 114].

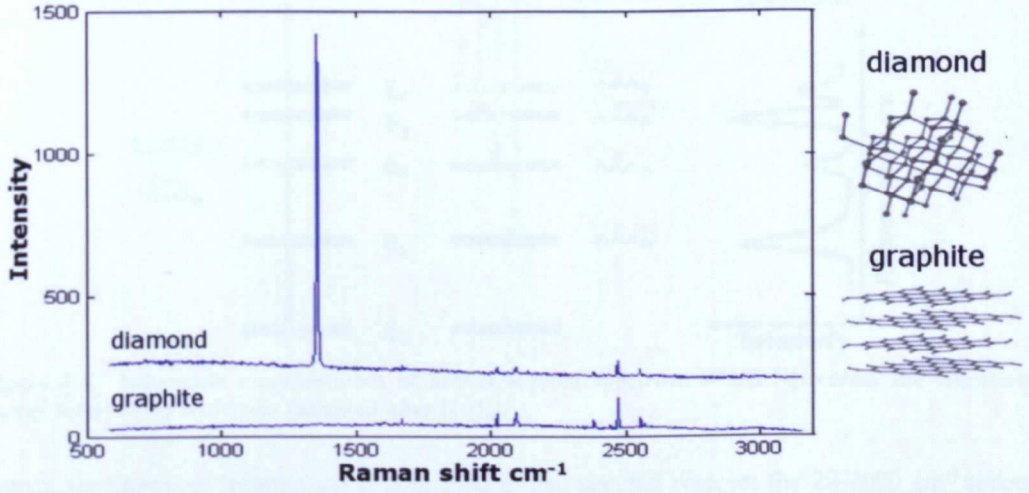

Figure 2-5. Raman spectra of two allotropic forms of carbon: diamond and graphite. This illustrates the significant differences in Raman spectra caused by crystal lattice vibrations. Excitation: 633 nm He-Ne laser, acquisition time: diamond 1 s; graphite 10 s.

2.4 Raman spectroscopy principles

Raman spectroscopy based techniques have many advantages, including a high chemical specificity and the ability to provide quantitative information about the sample in a minimally invasive or non-invasive manner with little or no sample preparation. The technique is well suited for studying live cells as water based solutions (buffers and culture media) do not interfere with experiments and there is no need for cell labelling or other cell modification [46, 47].

Raman spectroscopy does not provide direct elemental composition of a sample. The change in frequency of the scattered photon provides chemical and structural information which is characteristic of the chemical bonds or molecules present in the material. The Raman spectrum of a sample contains a set of peaks that are characteristic to different energies and therefore to frequency shifts (shown in Figure 2-6). Analysis of the scattered frequencies can give information on the material chemical composition, state and aggregation of the sample and even in some cases details of factors such as stress, orientation, and temperature [48, 114].

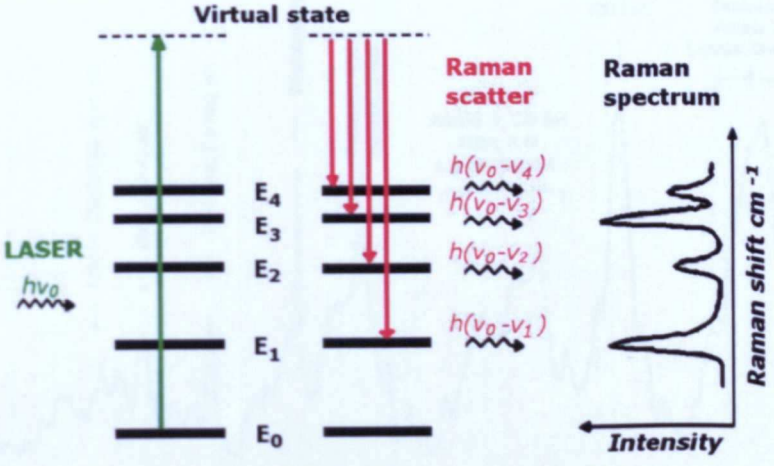

Figure 2-6. Schematic representation of Stokes Raman spectrum which represents the vibrational energy levels of the molecules (adapted after [103]).

Raman spectroscopic information is contained in two spectral regions: the 20-2000 cm^{-1} spectral interval, often referred to as the fingerprint region, which is very rich in spectroscopic information, and the 2000-4000 cm^{-1} region, or high wavenumber (HWVN) region, which contains the CH-, OH-, and NH-stretching vibrations. Spectral information on the majority of biomolecules contained inside cells, and therefore the region which nearly all research groups focus on, is in the fingerprint region in the range of 500-2000 cm^{-1} [39, 48, 49].

The Raman spectrum of a cell is a complex superposition of spectra arising from all molecules exposed to laser interaction and is dominated by peaks corresponding to proteins, lipids, nucleic acids and carbohydrates (see appendix 1 for details of Raman band assignments). Cells of different type or those in a different physiological state will vary in their overall molecular composition and this will be reflected in Raman spectra, as its shape depends on concentration of the biomolecules [58-60]. An example of a Raman spectrum of a cell (T-cell) with major peaks assigned and representative spectra of the major biomolecules contained within cells are shown in the Figure 2-7.

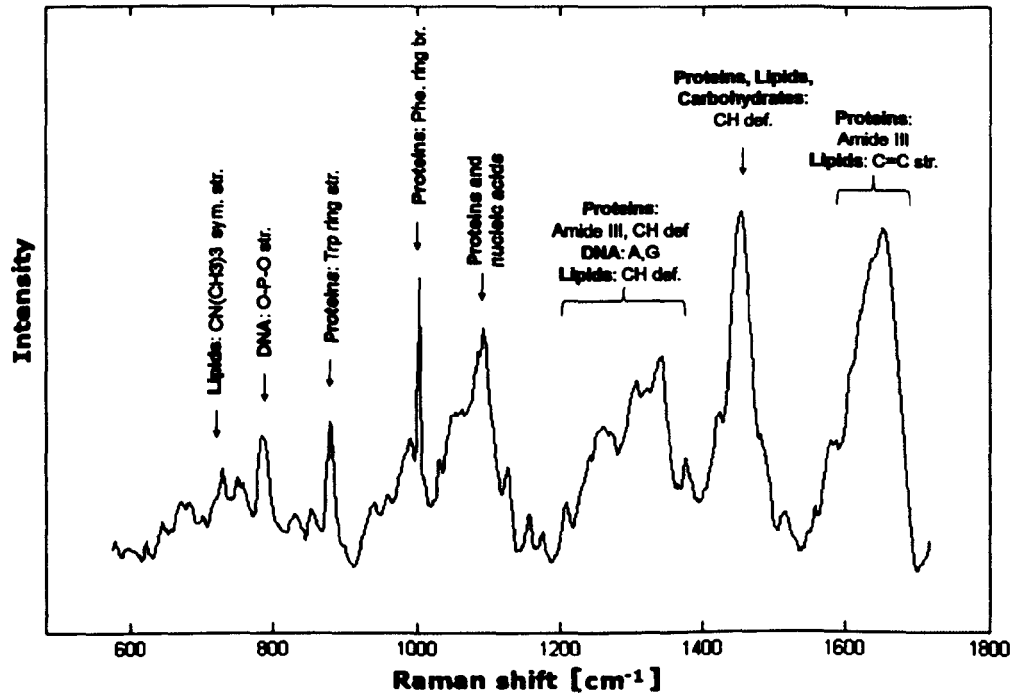

Figure 2-7. Typical spectrum of cell (T-cell) showing high heterogeneity of cells.

In the majority of cases Raman measurements of cells were completed on only one or a few different points (usually with extended laser focus) in the cell [71, 107]. This method reveals some information about biochemical composition of a cell but it can be misleading due to high intra-cellular variability, therefore different points in the cell will differ from each other. Another possible approach is to obtain an average signal from the entire cell by the use of expanded (in planar plate) laser focal spots [56, 85], or by fast scanning of the laser light over the whole cell [92]. In such methods the average acquisition times are usually of tens of seconds to ensure spectra with suitable signal-to-noise ratio. A new advance in Raman spectroscopy, which gives better understanding of localized cellular changes, is spectral mapping, also called hyperspectral imaging. The ability to accomplish Raman micro-spectroscopy mapping provides an understanding of biochemistry and morphology of specimens under investigation. Images are constructed from point spectra collected at different spatial positions within a cell. A spectrum is collected at each pixel by moving the sample typically in a raster pattern with small step increments. The laser can be focused to a diffraction-limited spot size. Such high spatial resolutions allow spectra to be obtained from sub-cellular organelles with features dominated by a single biochemical component. Commonly,

collection of hundreds or thousands of spectra is required to completely characterize a cellular system. The acquisition time of each spectrum has to be reasonably short so that the measurement time required for the entire cell will be sensible, usually integration times of around 1-2 s are used. Since a complete Raman spectrum is associated with each pixel, Raman maps can be used to generate chemical images revealing the structure and arrangement of sub-cellular organelles, and can provide insight into cellular biochemical dynamics. In addition, spectra from different cellular locations can be averaged to generate a spectral biochemical representation of the cell [69, 84, 85].

2.5 Types of Raman spectroscopy used in cell and biomedical studies

There are a number of different types of Raman spectroscopy and microscopy techniques. Most of these techniques have potential to study cells and tissues. These methods are outlined briefly in the following sections:

2.5.1 Non-resonant Raman microscopy (RM) & Confocal Raman microscopy (CRM)

In non-resonant Raman microscopy (RM) or micro-spectroscopy (RMS) a spectrometer is combined with an optical microscope to provide higher spatial resolution and collection of the Raman signal from micrometric samples. The Raman frequency shift is analyzed at different points on the sample to resolve regions with different chemical composition in a sample [49, 114].

Confocal alignment uses an additional aperture to block out-of-focus light and thus improve spatial resolution. The Raman scattering from the out-of-focus points from the sample is refracted by the microscope objective and blocked-up at the pinhole aperture. Consequentially, total amount of scattered light transmitted to the detector is reduced by a few orders of magnitude but without affecting the focal brightness. The resulting Raman spectrum therefore contains Raman signals which arise almost exclusively from a point (the focal point of the laser) within the bulk of the sample. This technique greatly reduces background signal making the Raman peaks clearer and providing an increase in resolution, especially in an axial direction [20, 119, 120].

The possibility of generating two-dimensional and three-dimensional images of a sample, using various features, is an evident advantage over either traditional spectroscopy or microscopy [20, 57,

58]. The CRM has been used for imaging on fixed (cell organelles [86-88], and reaction of cells to drugs [69, 85, 89]) and live cells (cell cycle dynamics [66, 99], drug and radiation effect on cells [97, 98, 101]).

A confocal Raman micro-spectrometer has been developed for the work presented in this thesis and details of its design and implementation will be discussed in more detail in the next chapters of this thesis.

2.5.2 Raman optical activity (Polarised Raman)

Raman scattering is partially polarized. This effect is most easily seen with an excitation source which is itself plane polarized. Raman optical activity is a technique which compares the different polarisations of Raman scattered light from chiral and highly aligned molecules such as those found in biology, in order to determine more about their structure. To obtain the information about the polarization of scattered light from samples additional features, namely a polarizer and analyser filter, have to be added to the Raman system. This technique probes additional information to conventional Raman spectroscopy because it is sensitive to the molecular ordering of sample components and can also be combined with amplifying techniques such as resonance and surface enhancement [48].

The polarised Raman technique was recently used for studies of horse heart cytochrome c [121], crystallised molecules involved in photosynthesis process [122], and for probing basal cell carcinoma (BCC) of skin tissues [123].

2.5.3 Resonance Raman (RR)

Many (especially coloured) substances absorb laser beam energy and generate strong fluorescence emission which can overwhelm the Raman spectra. This is one of the central problems in Raman spectroscopy especially when UV and visible lasers are used. Nevertheless, it was discovered that instead of fluorescence some types of coloured molecules could produce strong Raman scattering under certain conditions. This effect is known as the resonance Raman effect.

The resonance Raman effect occurs when the excitation laser frequency is chosen in such a way that it crosses the frequencies of electronic excited states and resonates with them. The intensity of Raman bands is enhanced three-to-five orders of magnitude. The highest intensity of resonance Raman signal is obtained when the laser frequency equals the first vibrational level of the second electronic excited state. To obtain this type of resonance effect tunable lasers are the most appropriate choice of excitation source. However, even when the frequency of the laser does not exactly match the desired electronic excited states, impressive enhancement of the Raman signal can occur [46, 48].

The enhancement of spontaneous Raman bands is not equal. The highest level of enhancement is experienced by molecules with a chromophoric group embedded in them. Due to the high level of light absorption of these groups chromophores are responsible for the molecular coloration. Chromophoric groups are parts of many proteins; therefore RR allows high specificity where normal scattering Raman techniques fail due to the high complexity of the proteins being studied. The charge-transfer transitions of the metal complex in chromophores usually enhance metal-ligand stretching modes, together with some of the modes associated with the ligand only. Consequently, in a molecule with thousands of vibrational modes, RR spectroscopy allows the study of only a few vibrational modes at a time. This reduces the complexity of the spectrum and allows easier identification of an unknown protein. The main disadvantage of the RR spectroscopy is the increased risk of fluorescence and photo-degradation of the sample due to the increased energy of the excitation laser photons.

The application of resonance Raman spectroscopy includes studies of optically trapped erythrocytes [124, 125] and cells contaminated with malaria viruses [126] detection of cytochrome c in living cells [99, 127] and of the carotenoid antioxidant substances in the living human skin.[128].

2.5.4 Fourier transform Raman spectroscopy (FT Raman)

A near-IR FT Raman instrument consists of a continuous-wave 1064nm Nd:YAG laser as a source and instead of using dispersive gratings or wavelength analysis an NIR-optimized Michelson

interferometer fitted with high efficacy Ge or InGaAs detector is employed. The FT Raman method requires high laser powers of 0.5 to 1 W and the measurement provides an interferogram that can be transformed to a Raman spectrum by calculating the Fourier transformation (FT). The FT-Raman approach reveals several attractive features: almost complete fluorescence rejection (due to the use of an excitation laser which is in a frequency region where most materials do not absorb light), high frequency accuracy (due to the use of an internal reference laser), and the FT's multiplex and throughput advantages (which allow simultaneous detection of all scattered wavelengths of light as it is not restricted by the dispersion of gratings). However, aqueous solutions which are often used in measurements of cells absorb significant amounts of the near IR radiation used in FT Raman. This can lead to transformations of the relative intensities of bands in the spectra. Another disadvantage is that FT-Raman can only be used for studying large samples as FT-Raman microscopes have a typical resolution which is worse than 5 μm and long integration times are required since the Raman signal is $\sim \lambda^{-4}$. This method is therefore well suited for imaging of tissue compounds and was used for studies of skin [53, 129] but is unsuitable for the imaging and study of single cells [48, 57, 114].

2.5.5 Coherent anti-Stokes Raman spectroscopy (CARS)

CARS is a type of non-linear Raman spectroscopy. Instead of the traditional single laser, two very strong collinear lasers are used to irradiate a sample. The frequency of the first laser is usually constant. However, the frequency of the second laser can be tuned in a way such that the frequency difference between the two lasers exactly equals the frequency of a Raman active mode of interest. This particular mode will be strongly enhanced in the final Raman signal. CARS is therefore limited in that only one strong Raman peak of interest can be obtained. In this technique a monochromator is not necessarily required as a wide band interference filter and a detector behind the filter can work in its place [48, 130].

The technique is particularly useful when used in fast optical imaging as applied to particular chemicals; no complicated spectral analysis techniques are required. Due to the abundance of C-H bonds in lipids, CARS is perfectly suited for rapid imaging and analysis of the lipid content in

living cells [45, 131]. CARS was used to study lipid droplets organelles [131-133], dynamics of organelles during cell division [134] or the dying process of yeast cells [72]. More recently broadband CARS has been developed [135, 136], but still the spectral resolution and accuracy is much lower than in conventional Raman.

2.5.6 Surface- and tip-enhanced Raman spectroscopy (SERS & TERS)

SERS and TERS utilize the following effect: the Raman signal from molecules adsorbed on certain metal surfaces can be five-to-six orders of magnitude stronger than the Raman signal from the same molecules in bulk volume. The exact reason for such dramatic improvement is still under discussion, but most papers suggests that the enhancement of Raman signal occurs due to the local electromagnetic field enhancement that is provided by optically active rough metallic surfaces or nanoparticles in close proximity to the Raman active molecules.

One disadvantage of these techniques resides in the interpretation of the spectra it produces. The signal enhancement is so dramatic that very weak Raman bands which are unnoticeable in non-resonant Raman spectra can appear in the enhanced spectra. Some trace contaminants can also contribute additional peaks. Moreover, because of chemical interactions with metal surfaces, certain peaks, which are strong in conventional Raman, might not be present in SERS or TERS at all. The non-linear character of signal intensity as a function of concentration complicates matters even further [48, 114, 137-139].

In all applications of SERS the choice of an appropriate surface substrate is very important. The most popular and universally used substrates employed for SERS are electrochemically-etched silver electrodes and silver and gold colloids with average particle sizes below 20 nm. TERS, on the other hand, usually uses sharp gold plated atomic force microscopy (AFM) tips. During recent years, it has been demonstrated that surface- enhanced Raman scattering (SERS) can open new capabilities for creating new labels particularly for the study of living cells [106, 140-143]. The new class of labels for live cells studies used gold nanoparticles and particular reporters [141]. Furthermore, pH-sensitive plasmonic-active fiber-optic nanoprobes suitable for intracellular

bioanalysis in single living cells were also reported [142]. Additionally the surface of fixed bacterial cells was studied by SERS [144] and TERS [145] combined with AFM imaging.

Chapter 3.

Instrumental development

If Edison had a needle to find in a haystack, he would proceed at once with the diligence of the bee to examine straw after straw until he found the object of his search... I was a sorry witness of such doings, knowing that a little theory and calculation would have saved him ninety per cent of his labor"

Nikola Tesla (1856 - 1943)

The objective of this chapter is to present the development of a Raman micro-spectrometer for the biochemical analysis and imaging of living cells. Details of the setup components with emphasis on issues to consider when working with living cells and of the software development, which allows spectral imaging of the samples will be discussed.

3.1 Major components

The major concerns when building a Raman setup for the study of living cells are: high collection efficiency (to counteract the intrinsically low Raman signal); avoiding cell damage (this depends on the wavelength and power of the excitation source), timing (a short acquisition time is essential for fast spectral imaging); maintaining proper conditions for cells during the experiment (temperature, CO_2 concentration and sterilisation are all important factors). Existing, commercially available Raman instruments are not suitable for prolonged experiments on living cells as they do not fulfil many of these requirements.

A high sensitivity Raman micro-spectrometer with the ability to perform time-course spectral measurements for non-invasive studies of biochemical processes in living cells has been developed. This has included instrumental design and development, purchase and assembly of all parts of the spectrometer and the development of software to automate the system and allow spectral imaging. The experimental setup has been continually modified and developed to optimize the instrumentation for the investigating of living cells.

As shown on the schematic diagram in Figure 3-1 modern Raman setups typically consist of four major components:

1. Excitation source (laser).
2. Sample illumination system and light collection optics (microscope, mirrors and lenses).
3. Wavelength selector (filters and spectrograph with gratings).
4. Detector (CCD).

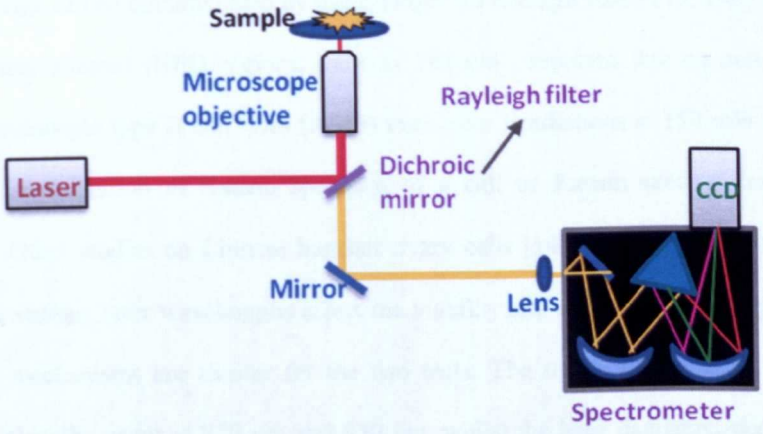

Figure 3-1. Simplified schematic of a typical Raman micro-spectrometer.

In this section all components of our system will be discussed in detail along with the important issues which arise when setting up a Raman spectrometer for live-cell imaging. Milestones in the setup development will be discussed and schematics presented in the following sub-chapters.

3.1.1 Laser

Lasers are universally used excitation source in modern Raman spectroscopy. A laser is a quantum-mechanical device that produces coherent radiation; energy is amplified to extremely high intensities by process called stimulated emission. A laser emits light in a narrow, low-divergence beam and with a well-defined wavelength. Laser beams are highly monochromatic and almost completely linearly polarised [146, 147].

Biomolecules inside cells and culture media are sensitive to light and this makes the choice of laser wavelength crucial for studying living cells. Two effects in particular need to be considered: cell photo-damage, which is a light-induced reduction in cell viability, and excitation of fluorescence emission, which can swamp any underlying Raman spectrum to such an extent that it is no longer detectable.

The efficiency of Raman scattering depends inversely on the fourth power of the incident light wavelength (Equation 2-9), indicating that the use of shorter wavelengths is preferred. However, shorter wavelengths result in an increased tendency for laser-induced damage and studies showed that visible lasers can induce cell death even at low laser powers and short exposure times [55].

Cell photo-damage can be circumvented by using longer wavelength lasers [55, 146]. Studies using lasers in the near-infrared (NIR) regions, such as 785 nm , reported that no cell damage was induced on pneumocyte type II cell lines (A549) even after irradiations at 150 mW and exposure times typical for collection of Raman spectrum of a cell or Raman spectral imaging (10-20 minutes) [56]. Other studies on Chinese hamster ovary cells [148] and E. Coli bacteria [149] to determine how various laser wavelengths affect the viability and cloning of cells suggests that the photo-damage mechanisms are similar for the two cells. The results demonstrate that the most damaging wavelengths occur at 870 nm and 930 nm, whilst the least damaging occur at 970 nm and 830 nm. However, wavelengths of less than 800 nm were not studied. The power density for these studies were higher than in most Raman micro-spectroscopy studies due to the higher numerical aperture objectives used in optical tweezers (1.2-1.3 NA) [148, 149].

The responses of CCDs, which are used as detectors, also depends on wavelength and have higher sensitivity in the visible range than in NIR [146, 150, 151]. Therefore, visible lasers allow shorter imaging times. The superior beam quality of single transversal mode solid-state (532 nm) and gas lasers (488 nm, 514 nm, 647 nm) produces smaller, diffraction limited laser spots on the sample, which allows better spatial resolution in the Raman spectral images [69, 88, 152].

However, light sources with longer wavelengths give much weaker signals and subsequently longer integration times and higher laser powers may be required when NIR lasers are employed as excitation sources for live-cell studies. Nevertheless, the advantage of a NIR source is that cell damage can be avoided and the spectra are almost fluorescence free. Irradiation of biological samples with a visible laser (i.e. green 514 nm) can promote this fluorescence, and the Raman signal may be no longer detectable [46, 153]. In such cases the use of a laser in the NIR may provide a solution. With lower photon energy, a NIR laser may not promote the electronic transition (and hence the fluorescence) thus reducing the background signal and allowing the Raman scattering to be detected. Figure 3-2 shows spectra of collagen, which produces a broad fluorescence background when 514 nm laser is used and no fluorescence when NIR 785 nm laser is used.

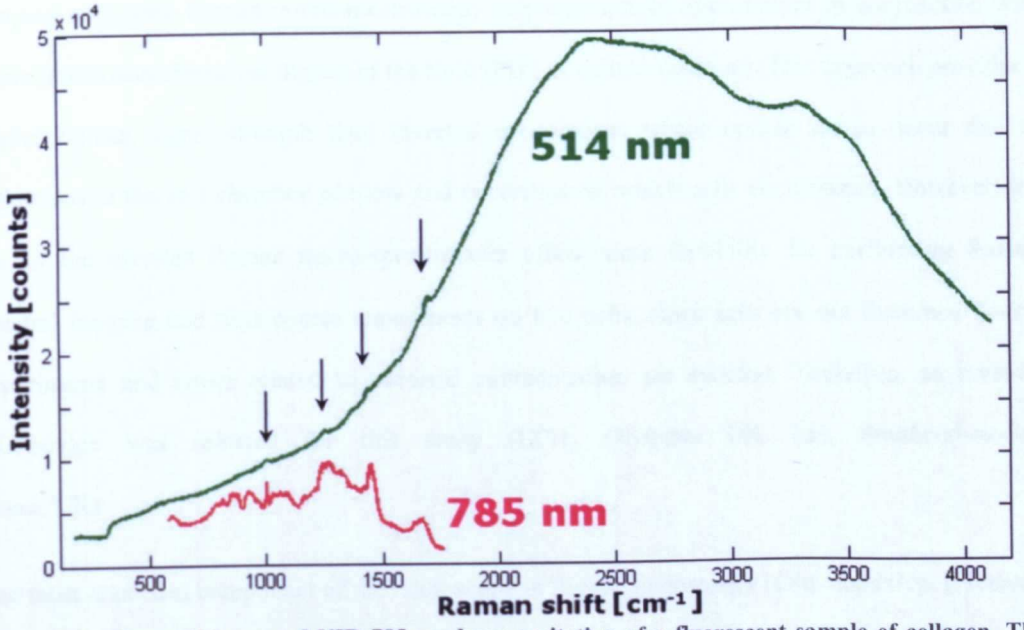

Figure 3-2. Green 514 nm and NIR 785 nm laser excitation of a fluorescent sample of collagen. The strong background seen with the green laser swamps the Raman signal almost completely, whereas the 785 nm excitation still enables the Raman signal to be detected.

Nevertheless, recent studies on fixed and live cells in buffer solutions using visible lasers [69, 88, 99, 152] suggest that the fluorescence background may be more often caused by cell culture media rather than cellular components. Therefore, the possibility that certain culture media may not produce fluorescence emission when excited by visible lasers cannot be excluded.

Considering the features discussed the choice of 785 nm as the Raman excitation wavelength appears to be the optimum utilitarian compromise. The laser chosen for our system is a continuous wave GaAs diode (XTRA, Toptica Photonics, Munich, Germany) laser with 785 nm wavelength and maximum power measured at 355 mW (~170 mW before objective) ; the laser beam diameter is 2.2 mm and quality factor given by manufacturer is $M^2 \sim 1.7$. The quality factor of a laser beam is a measure of beam focusability. The M^2 for ideal diffraction-limited Gaussian beam is 1. All actual laser beams have quality factor values greater than one, but for good quality lasers the value is close to 1.

3.1.2 Collection optics

A set of high quality mirrors and lenses combined with an optical microscope simultaneously allows sample illumination and collection of the scattered light. The majority of published work on

imaging cells with Raman micro-spectroscopy employs upright microscopes in conjunction with water immersion objectives dipped in the fluid (PBS or culture medium). This approach provides a higher Raman signal strength than inverted microscopes where optical losses occur due to reflections at the cell-chamber window and coverslips on which cells are cultured. However, the use of the inverted Raman micro-spectrometer offers more flexibility for performing Raman spectral imaging and time-course experiments on live cells, since cells are not disturbed during experiments and issues related to bacterial contamination are avoided. Therefore, an inverted microscope was selected for this study (IX71, Olympus UK Ltd, Southend-on-Sea Essex, UK).

The most important component of the microscope in Raman microscopy is the objective. It focuses the laser beam onto the sample as well as collects the resultant Raman scattered light from the sample. For Raman spectral imaging of cells the following characteristic of the objective was considered: i) high numerical aperture (NA) allowing high resolution and collection of light, ii) low background. The resolution of a microscope objective is defined as the smallest distance between two points on a specimen that can still be distinguished as two separate entities. The total resolution of a microscope system is dependent upon the numerical aperture; the higher the numerical aperture of the system, the better the resolution. [119]

Numerical aperture is generally the most important design criterion (other than magnification) to consider when selecting a microscope objective. Values range from 0.1 for very low magnification objectives (1x to 4x) to as much as 1.6 for high-performance objectives utilizing specialized immersion oils [49]. As numerical aperture values increase for a series of objectives of the same magnification, generally a greater light-gathering ability and increase in resolution is observed.

Mathematically, the numerical aperture is expressed as:

$$NA = n \sin \theta \qquad \text{Equation 3-1}$$

where NA is the numerical aperture, n is the refractive index of the medium between the cover glass and the objective front lens and θ is one-half the angular aperture. From Equation 3-1, the

numerical aperture increases with both angular aperture and the refractive index of the imaging medium [48].

Objectives that use water as an imaging medium are also available for applications with living cells in culture or sections of tissue immersed in physiological saline solution. By using an immersion medium with a refractive index similar to that of the glass coverslip, image degradation due to thickness variations of the cover glass are practically eliminated whereby rays of wide obliquity no longer undergo refraction and are more readily collected by the objective. Light rays passing through the specimen encounter a homogeneous medium between the cover-slip and immersion medium and are not refracted as they enter the lens, but only as they leave its upper surface.

Since Raman scattering is much weaker, when using a NIR 785 nm laser the choice of glass in the objective is especially important to maintain high transmittance of the NIR light. After trying several objectives it was found that a 60x magnification water-immersion objective with 0.9 NA and 2 mm working distance offered the best performance for cells imaging applications (LUMPLFL60xW/IR/0.90, Olympus, UK). This was preferred as it has special IR glass, which has good transmittance in the NIR region and it uses water as immersion medium. Water immersion is preferred over oil, as it does not contribute strong Raman peaks that could overwhelm the signal from the measured sample as opposed to immersion oils. Other objectives (e.g. phase contrast or dry lower magnification objectives) are available in our system and are used for easier identification of cells or fluorescence microscopy measurements.

3.1.3 Rayleigh filters

Since spontaneous Raman scattering is relatively weak, one difficulty in Raman spectroscopy comes from separating Raman photons from the intense Rayleigh scattering. However, the major problem here is not Rayleigh scattering itself, but the fact that the intensity of stray light from the Rayleigh scattering may exceed the intensity of useful Raman signal in close proximity to the laser wavelength [48]. For this reason the Rayleigh scattering must be removed.

Filters play a crucial role in enabling high-quality Raman spectroscopy measurements. In many simple laboratory layouts, the only filters needed are a laser-transmitting filter to remove all undesired light from the laser spectral output (such as broadband spontaneous emission or plasma lines) and a laser-blocking filter inserted between the sample and the spectrometer to ensure that no Rayleigh-scattered laser light reaches the detection system.

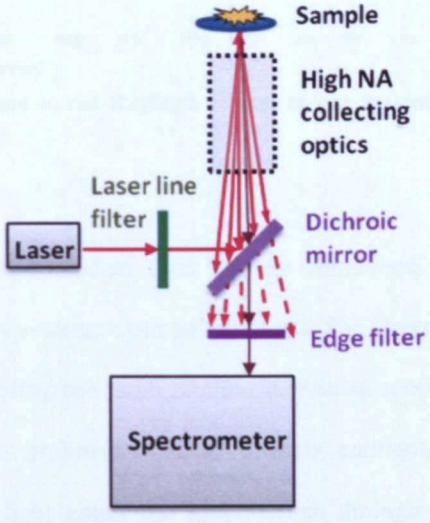

Figure 3-3. Schematics of filters setup in imaging Raman system.

However, in many high-performance Raman systems (such as those with microscopic imaging capabilities) complex focusing and collection optics are used to couple the system to the sample region. For these systems, it is desirable for the excitation laser beam and the Raman-shifted signal light to share a common light path. Figure 3-3 shows how this layout can be accomplished with a dichroic beamsplitter used in conjunction with a high-pass edge filter.

Semrock's (Semrock, Inc., Rochester, New York, USA) RazorEdge Dichroic beamsplitter and Ultrasteep Raman Longpass filter were chosen for our setup. The efficiency designs of the filters for 785nm laser line are shown in Figure 3-4. Beamsplitters reflect a standard laser line incident at 45° (98% reflectivity in s-polarization and 90% in p-polarization) whilst efficiently passing the longer Raman-shifted wavelengths. Edge filters cut light especially close to one side of the laser wavelength and have a sharp edge allowing observation of the smallest Stokes shifts and have the largest blocking of the laser line for maximum laser rejection.

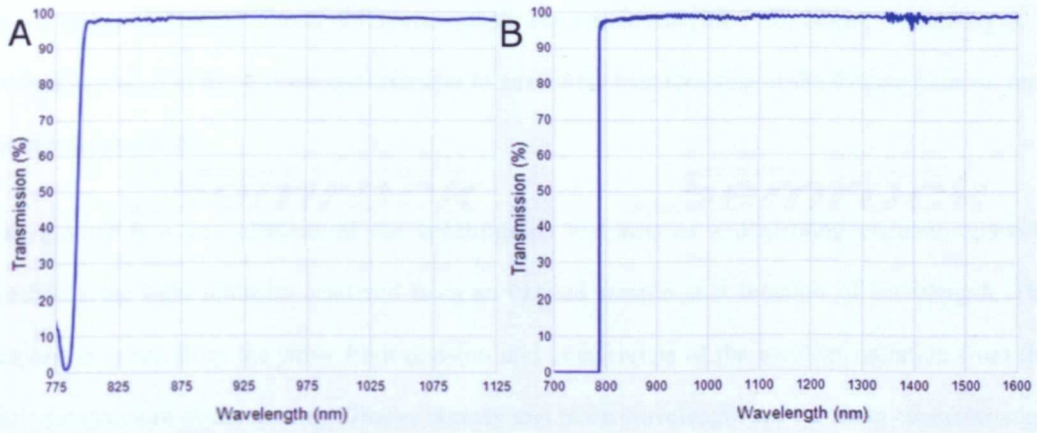

Figure 3-4. Design of filters used to cut Rayleigh scatter in our system: A. Dichroic mirror [154], B. High-pass edge filter [155].

3.1.4 Spectrograph

The spectrograph separates the incident light into its component wavelengths so the relative amounts of radiation at each wavelength can be measured. The Czerny-Turner spectrograph is one of the most widely used spectrograph configuration in Raman spectroscopy. The Czerny-Turner spectrograph uses mirrors as collimators in an off-axis configuration and employs a planar reflective grating. Focussed light enters the spectrograph through an entrance slit and is then collimated and shone on a grating which disperses that light. The light is then focused onto a photo sensitive CCD detector, which detects the Raman spectrum, as illustrated in Figure 3-5.

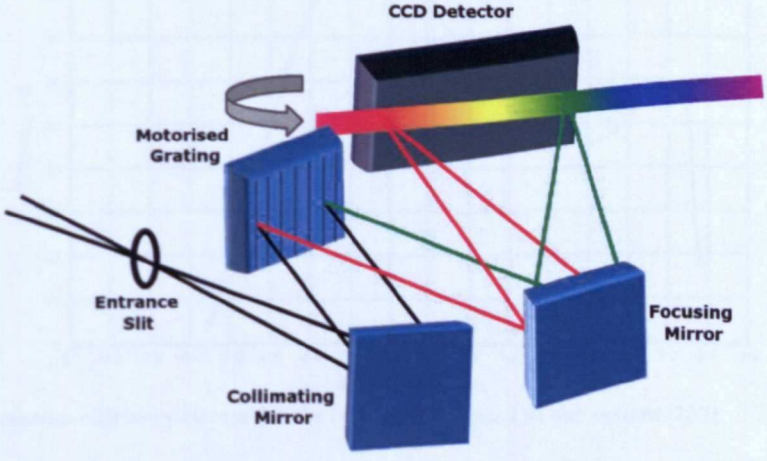

Figure 3-5. Schematic illustration of the interior components of a spectrograph.

In our system a Czerny Turner f/4 spectrograph was employed (SR-303i; Andor Technology). A f/4 lens is placed in front of the spectrometer to ensure the best focusing of the Raman photons onto the spectrograph slit.

The grating is a key element of the spectrograph and acts as a dispersing element, spatially spreading the light intensity scattered from an excited sample as a function of wavelength. The dispersion arises from the wave front division and interference of the incident radiation from the periodic structure of the grating. Groove density and blaze wavelength are the main characteristics. The former is defined as the number of grooves per unit length and blaze wavelength is the wavelength at which grating has maximum efficiency.

Spectral resolution, the ability to distinguish two closely spaced peaks, is determined by a combination of the size of the entrance slit and the diffraction grating groove density [156]. Therefore whilst reducing slit width enhances resolution, it reduces light throughput which will ultimately degrade the signal-to-noise ratio (SNR). Furthermore, spectral resolution increases as groove density increases, however at the expense of spectral range [48, 156].

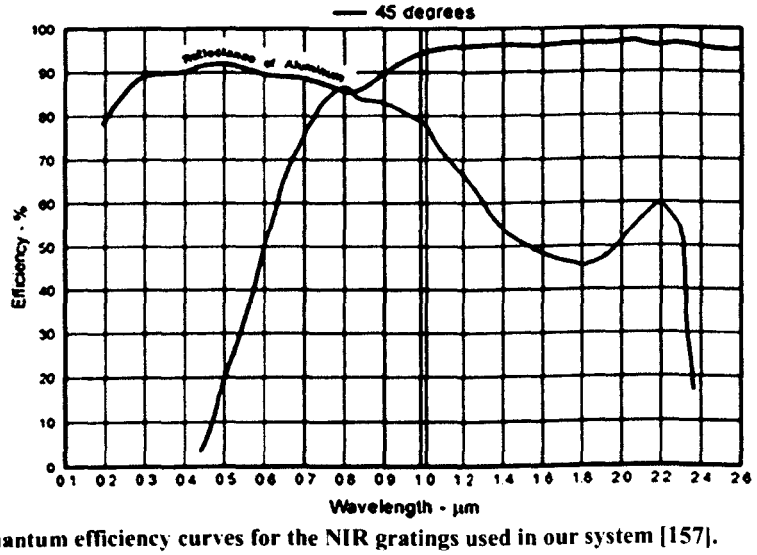

Figure 3-6. Quantum efficiency curves for the NIR gratings used in our system [157].

Our system consists of one grating which is optimized to operate in the NIR spectrum. The grating size is 64mm x 64mm, has a groove density of 830 lines/mm, and a blaze wavelength of 820nm

(Newport-Corp, Richardson Gratings, Rochester, New York, USA). The quantum efficiency of the grating as provided by the manufacturer is shown in Figure 3-6.

3.1.5 Detector

Currently, charge coupled devices (CCDs) are the most commonly used detectors in Raman spectroscopy. CCDs are silicon-based semiconductor devices arranged as an array of photosensitive elements (in our system an array of 1024 x 127 elements each 26x26 μm in size). Each element generates photoelectrons and stores them as an electrical charge. The charge stored on each individual pixel is a function of the number of photons striking that pixel and then read by an analogue-to-digital converter. CCD cameras are ideally suited for rapid, multi-channel, low-light applications such as Raman spectroscopy [48].

Sensitivity and performance of CCD detectors are rapidly improving and modern CCD cameras are able to detect photons in the NIR area. The CCD used in our system is Andor's iDus back illuminated deep depletion CCD camera for NIR region (DU401A, Andor Technology plc., Belfast, UK), which provides both thermoelectric and water cooling enabling the detector to be cooled to -100°C. This detector has maximum sensitivity over the desired range of wavelengths, in this case the NIR region (700-900 nm) and gradually declines outside this range. For the quantum efficiency of the CCD is showed in Figure 3-7.

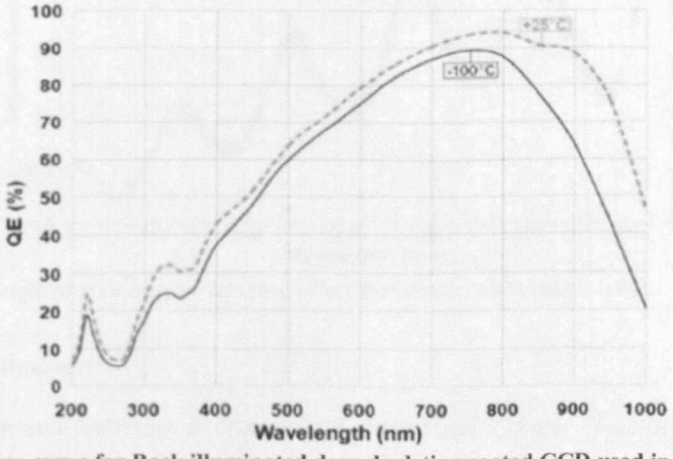

Figure 3-7. Efficiency curve for Back illuminated deep depletion coated CCD used in our system [158].

To improve the SNR, high performance CCD detectors should be cooled to reduce noise known as dark current, which is a slow and steady growth of unwanted signal generated by the heat inside the detector. The advantage of back illuminated chips is that the surface is clear of obstruction (the back of the CCD has no electrodes), therefore is more sensitive. Deep depletion means that the CCD has a deeper photoactive region, which is known as the depleted region. That allows the measurement of photons which otherwise might pass right through the chip and not be detected. One drawback of back illuminated CCDs is the fringing or etaloning effect (see in Figure 3-8). Fringing is a resonant effect that occurs at NIR wavelengths (the silicon becomes increasingly transparent) allowing the light to reflect back and forth between the two surfaces, setting up a standing wave pattern. Amplitude can be lost at the reflective surfaces or absorbed into the silicon body of the device, but at longer wavelengths sufficient amplitude survives to lead to unwanted fringes of constructive or destructive interference which artificially modulate a spectrum. The amount of the resulting fringing patterns depends on optical factors such as the parallel nature of light impinging on the sensor and of the relative shot noise of the signal. This effect could modify or absolutely cover the Raman signal [48, 49].

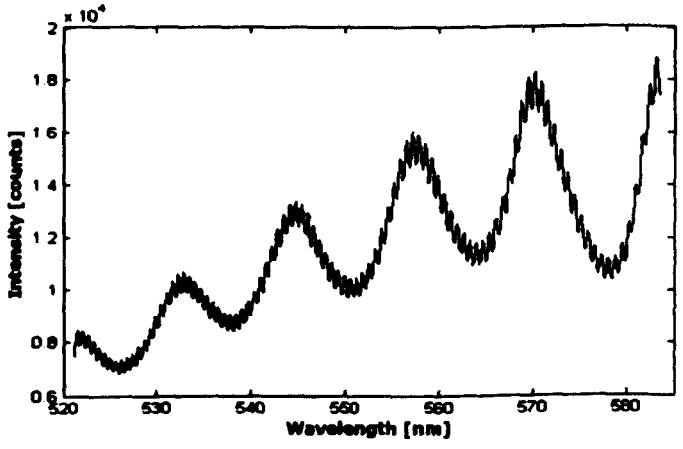

Figure 3-8. An example of etaloning or fringing effect that covers all Raman signal.

3.1.6 Optical alignment

Accurate alignment and focussing is crucial with any optical system. Alignment is achieved by guiding the light and appropriately positioning and securing each piece of optical equipment, namely laser, microscope, spectrometer, detector and every mirror and lens, in the light path. The

alignment and focussing of the system is completed in two parts. Firstly the laser is aligned into the microscope through a system of mirrors onto a sample. The laser is aligned directly through the centre of the objective, so that when the focussing of the objective is varied the laser spreads in concentric circles and ideally is in focus when the sample is in focus. Good alignment of the laser into the microscope and onto the sample means that the maximum power available from that laser can be focussed into the smallest area possible (see Figure 3-9). This will ensure the greatest excitation of the sample and in turn strong Raman scattering.

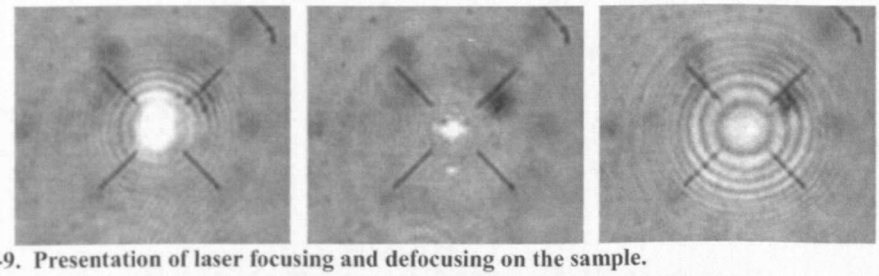

Figure 3-9. Presentation of laser focusing and defocusing on the sample.

Subsequently, the collection of the resulting signal from the sample is performed. In order to align the scattering though the centre of all the optics, into the spectrometer and focussed at the entrance slit and similarly on the CCD, an image from the microscope is followed along this path. Proper alignment makes it possible to image the laser spot onto a few pixels of the CCD (figure Figure 3-10). Good alignment of this scattering into the spectrometer and onto the CCD is important for focussing and collecting the entire signal whilst restricting background and noise.

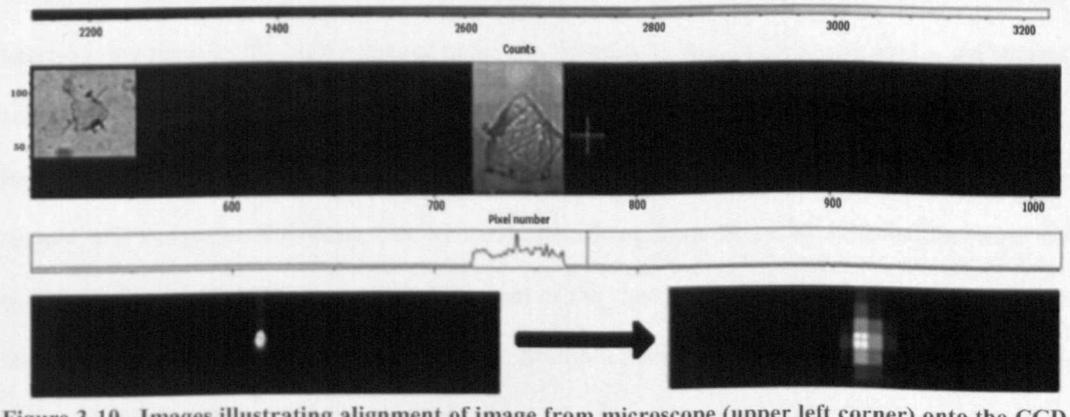

Figure 3-10. Images illustrating alignment of image from microscope (upper left corner) onto the CCD (upper image) and then focusing the image with the lens into single pixel (bottom images).

3.1.7 Light gathering and noise

The ability to extract analytical information from the Raman spectra is usually limited by the collection of high signal-to-noise ratio (SNR) spectra. Transmission of light through optical system is the fraction of light intensity that is accurately collected into the input and effectively received at the output. Ideally, this is the result of the optical efficiencies of all optical components in the optical path, but actually it is less, down to blocked or lost light, such as light that falls outside the acceptance aperture of an optical element. Optical throughput, also termed etendue, specifies the geometric capability of an optical system to transmit radiation. In an optical system the numeric value of the etendue is calculated as the product of the entrance aperture and the solid angle through which light is accepted:

$$E = A\,\Omega \qquad \textbf{Equation 3-2}$$

where E is etendue; A is the area of the entrance aperture and Ω is the solid angle.

For instance, magnification of an image changes the image area and solid angle but not the optical throughput. Thus the etendue of an entire optical system cannot exceed the smallest etendue at any point. A perfect optical system produces an image with the same etendue as the source [48, 49, 114].

Raman scattering is a very weak effect and the output spectrum is a combination of signal from the sample as well as noise. The source of limiting noise is an important consideration in Raman spectroscopy because the high levels of noise can severely reduce or even overwhelm the Raman signal. The observed spectral noise can be divided into two causes: additive and multiplicative noise. Additive noise or system background is always present, regardless of the presence of a sample, and comprises dark current as well as noise arising from the empty surrounding (when no sample is present). Additive noise is independent of the signal strength, whilst multiplicative noise increases proportionately with signal strength. Multiplicative background is associated with shot noise. Thermal motion of electrons in electrical circuits and straight light falling onto detector counting as shot noise. Its magnitude is proportional to the square root of the signal [48, 151].

SNR compares the level of a desired signal to the level of background noise. The higher the ratio, the less protruding the background noise is. A CCD plays an important role in improving SNR. Background noise can be reduced by using longer exposure time, averaging acquired spectra and also by not using the entire CCD chip. When the signal is properly focused onto the detector it is possible to use only a few tracks instead of the whole chip of the CCD. Figure 3-11 demonstrates the Raman scattered light focused only on a few rows of pixels of the CCD detector. Only a certain number of rows (~10) are set as spectral readout without losing any spectral information.

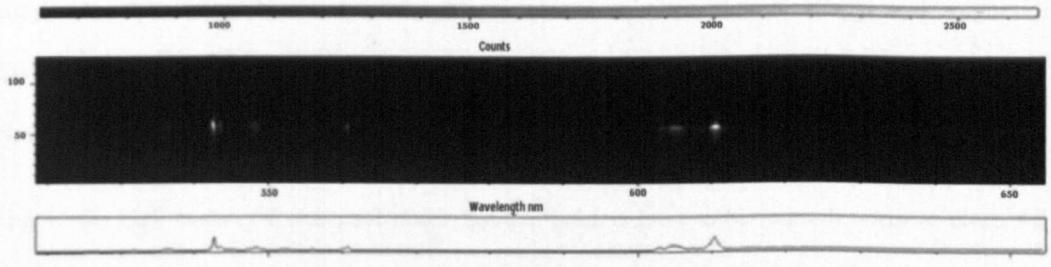

Figure 3-11. CCD image illustrating the focusing of Raman signal to few rows on the CCD chip.

3.2 Biological issues in live cells measurement

3.2.1 Maintaining cell viability

Cell culture is the complex process by which cells are grown and maintained under controlled conditions. Culture conditions can vary widely for each cell type and changing conditions for a particular cell type can result in different characteristics. The major environmental conditions important to keeping cell culture healthy are: an appropriate temperature (usually 37°C) and gas mixture (for mammalian cells typically 5% CO_2) . A cell incubation chamber was installed over the microscope (Solent Scientific Limited, Segensworth, UK) to maintain the cells in the correct conditions for prolonged studies by Raman micro-spectroscopy. The environmental chamber is designed for use with Olympus inverted microscope and painted black to minimise any straight light hitting the sample during measurements.

Culture contaminants may be biological (bacteria, moulds and yeast) or chemical (toxical substances e.g. some metal ions, plastics) and they can cause undesirable effects on the cell culture and consequently on the quality of the study. The use of the inverted microscope and cell chamber

permit sterile conditions to be kept during the course of the experiment. Additionally, cleaning procedures were established in our lab and the use of especially design sample holders for living cell experiments was essential.

3.2.2 Sample holder

The use of an inverted microscope requires the construction of special sample holders for the imaging of cells. Normal glass or plastic flasks used in cell biology cannot be used due to thickness and high Raman signal produced by these materials. Usually cells attach and grow well on substrates with lower Raman spectra such as quartz, calcium fluoride (CaF_2) and magnesium fluoride (MgF_2) [95, 159]. All these materials were considered to form the bottom of our cell chamber.

Due to the high costs of Raman substrates sample holders have to be reusable, easy to clean with possibility of sterilisation in an autoclaving process. In the Figure 3-12 the design of the sample holder is shown.

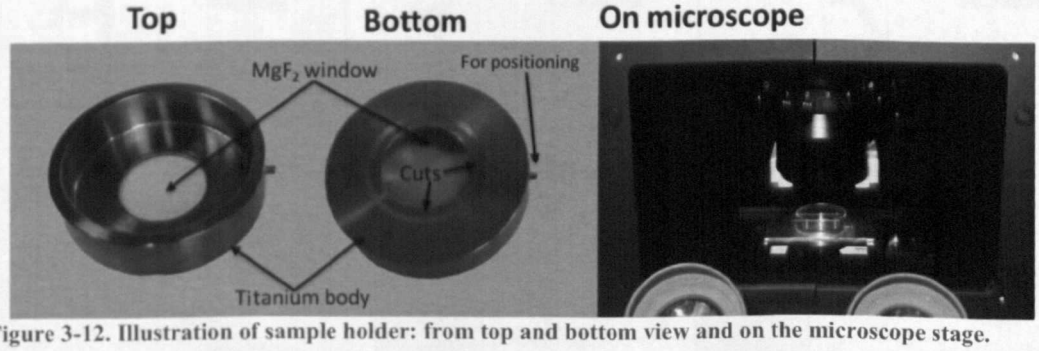

Figure 3-12. Illustration of sample holder: from top and bottom view and on the microscope stage.

The bottom of the sample holder was made from thin (0.17 mm) MgF_2 slides as it was found to be the best material for Raman studies on biological samples. The sample chamber body material has to be non toxic for cells, therefore medical grade titanium was chosen. At the bottom of the holder precise cuts were made to allow repositioning of the sample on the microscope stage in order to be able to find exactly the same cells which were used for Raman analysis for fluorescence microscopy imaging.

3.2.3 Cross validation – immune-fluorescence

Raman micro-spectrometry is not yet a well established technique in cell biology; therefore there is a need for validation and confirmation of biochemical findings by Raman studies with an independent technique, which is well recognized in cell biology. Therefore, wide field fluorescence microscopy imaging system (Olympus UK Ltd., Southend-on-Sea, UK) was added to the Raman setup. This included a Hg lamp and a sensitive CCD camera with a broad set of fluorescence filters enabling the use of several fluorescent dyes. In this way Raman spectral images could be compared with the fluorescence images of the same cells.

3.3 Setup developments

The experimental setup was continually developed to optimise the performance. The major stages of our setup developments are shown in Figure 3-13.

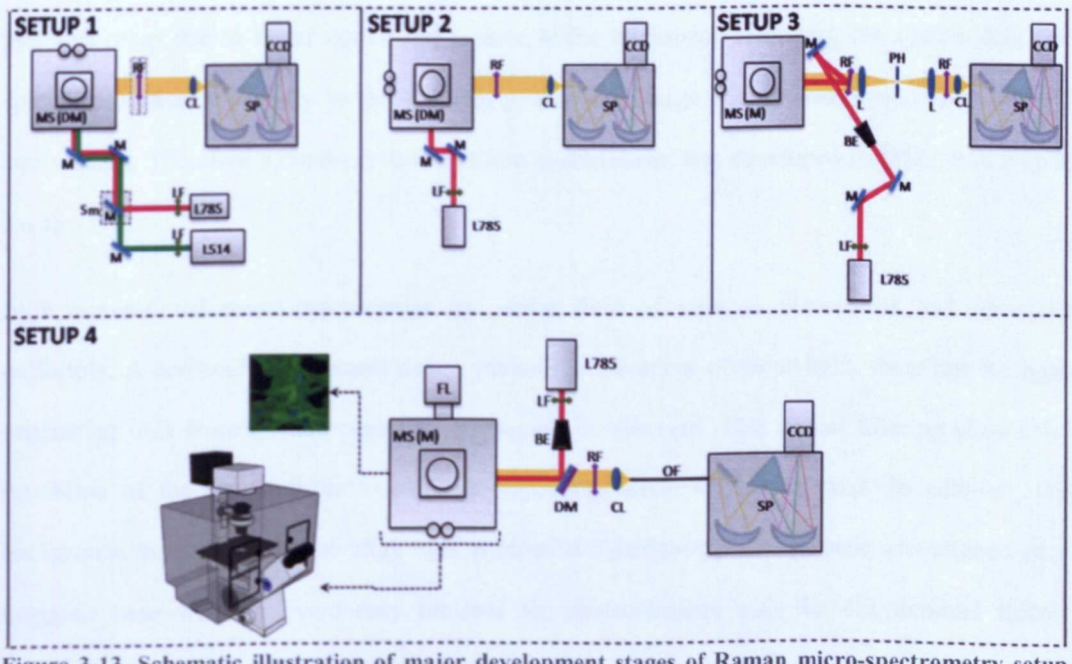

Figure 3-13. Schematic illustration of major development stages of Raman micro-spectrometry setup where MS – microscope with (DM) – dichroic mirror inside, (M) – 99% NIR reflectivity mirror inside; L785 and L514 lasers with excitation wavelength indicated; SP – spectrograph; CCD – camera; LF – laser line filter; M –mirror; Sm – step-motor; RF – Rayleigh scatter cutting filter; CL – collecting lens; L – lens; PH – pinhole; BE – beam expander; DM dichroic mirror; OF – optical fiber; FL – fluorescence excitation lamp.

At first our aim was to build a Raman spectrometer for studies of cells and for identification of other samples (SETUP 1, Figure 3-13). Accordingly we employed three lasers (633nm He-Ne

laser, 488/514nm Argon laser and 785nm diode laser) allowing a choice of wavelength depending on the application; a step-motor, which is a device with a fine accuracy moving platform on which optical components could be attached, was used to switch between the laser wavelengths, Dichroic mirrors and notch filters were placed in the microscope so that they could be changed according to the wavelength used in each experiment. However having one spectrometer for many applications forced compromises on the optics (e.g. mirrors, lenses, gratings), which brought more losses in the system. In addition, switching between lasers created several instabilities in focusing and slight realignment was needed prior to almost every measurement. Therefore, a spectrometer dedicated only to biomedical experiments with a NIR 785 nm laser as the sole excitation source was built.

The laser beam was guided through a side port of the microscope and then focused on the sample through a dichroic mirror. The signal was then collected through the back port of the microscope (SETUP 2 in the Figure 3-13). The signal to noise ratio achieved was much higher than in the previous setup due to better optics and a more stable alignment. However, the system had low spatial resolution, especially in the Z-plane, producing a large background signal from the cell surrounding. Therefore a confocal Raman micro-spectrometer was developed (SETUP 3 in Figure 3-13).

In a conventional micro-spectrometer the entire field of view is illuminated and observed uniformly. A confocal arrangement uses a pinhole to block out-of-focus light, therefore the light originating only from a small region of the sample is observed. This spatial filtering allows the resolution of the spectrometer to increase, especially along the optical axis. In addition, the background noise cause by the stray light is reduced significantly. The pinhole was aligned on a magnetic base which allowed easy removal for measurements with the conventional micro-spectrometry setup. To improve the focused laser spot size in the XY plane a beam expender was included in the laser path. A beam expander ensures that the objective entrance is completely filled by the laser and therefore focussing to a tighter spot size. Furthermore, a 99% reflectivity NIR mirror was used to guide the light into the microscope and ensure that any loses of excitation and scattered light are reduced. Thus the excitation laser light and collected scattered light were guided

through the back port of the microscope. This setup had a superior signal-to-noise ratio and was suitable for cell and tissue sample measurements. However, using the back-port was not ideal because the need for wide-field fluorescence and the installation cell incubator over the microscope. This maintained the proper conditions for Raman measurements (we encounter several problems with sample contamination) and fluorescence microscopy of individual live cells allowing further confirmation of the Raman findings. Additionally, several instabilities were noted when changing the pinholes. Therefore in the next setup all the optics was installed in the special optical cages system and the scattered light guided by fibre optics into the spectrometer to increase the stability and performance of the system (SETUP 4, Figure 3-13).

The current setup uses a dichroic mirror to guide the light and an additional edge filter to remove all Rayleigh scattering. The light is then focussed onto an optical fibre which is attached directly into the spectrometer. The optical fibre core acts as a pinhole in this setup, therefore choosing fibres with different cores is equivalent to changing pinhole sizes (10 μm, 25 μm, 50 μm and 100 μm).

3.4 Software development

The final stage of the experimental setup involved the development of software to automate the data collection process. This software, developed in the Labview 7.1 programming language, allowed the collection of individual Raman spectra as well as Raman imaging.

Labview (Laboratory Virtual Instrument Engineering Workbench) is a graphically programmed computer language (G-language) for real-time instrumentation developed by National Instruments Corporation (Austin, Texas, USA). The Labview environment allows rapid software development due to large collection of user-friendly algorithms (displays, diagrams as well as library of functions to manage CCD). The disadvantage of using Labview is that compiled executables created by the Application Builder are not truly standalone programs; they require the Labview run-time engine to be installed on any target computer on which users run the application. This can make the program less stable and also slow down the process of acquiring the data.

Figure 3-14 illustrates the basic flow chart of the program when scanning the sample in raster pattern mode and Figure 3-15 shows the user interface of the software with major area indicated for further explanation.

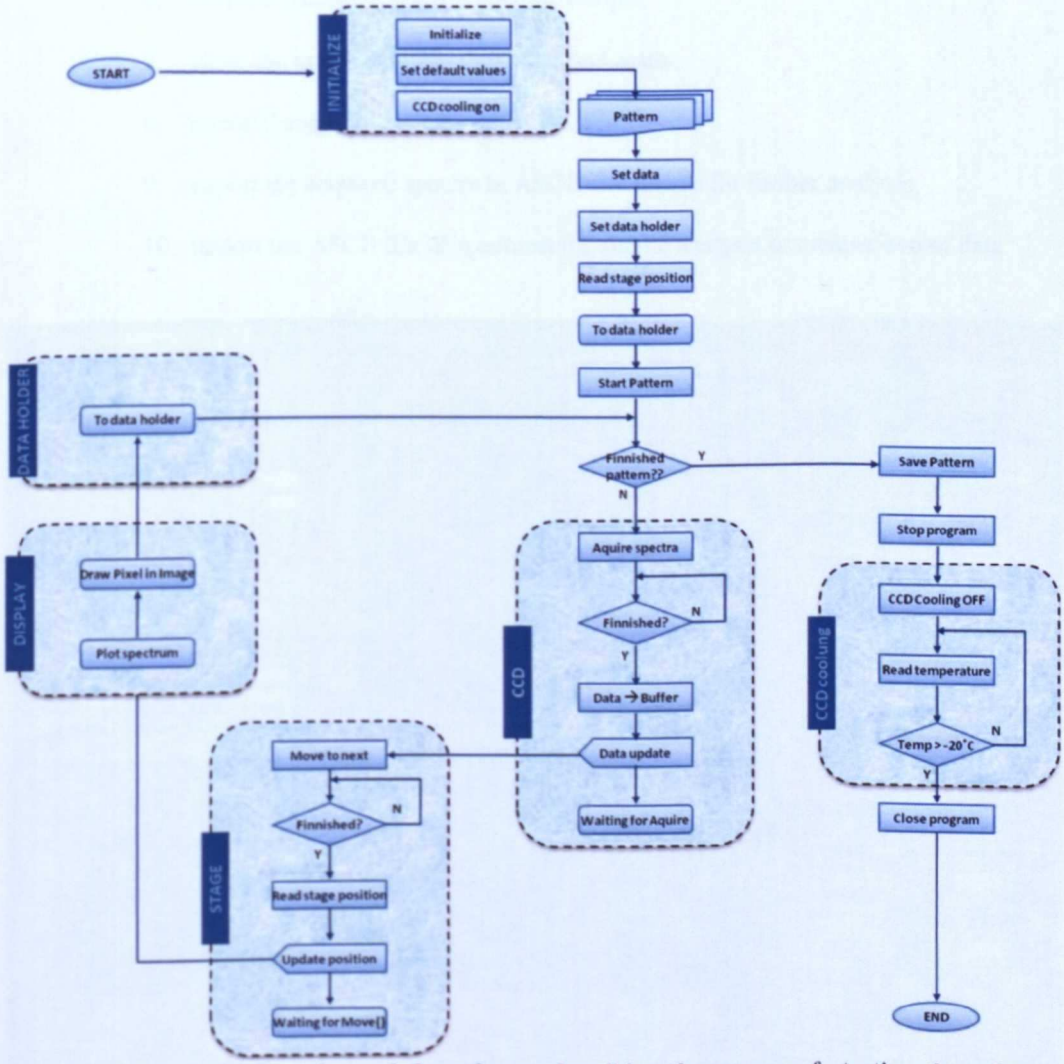

Figure 3-14 Schematic flow chart of the software describing the process of starting the software, applying a scanning pattern, saving data and then turning the program off.

The main functions of the software are:

1. control, adjust and monitor the temperature of the CCD cooling system,
2. acquire Raman spectra and capture images from the CCD detector,
3. display the Raman spectrum

4. perform calibration that converts pixel number into the Raman shifts or wavelength unit,
5. control the stage movement and allow monitoring of its current position,
6. perform patterned scans across the sample,
7. show the image created from patterned scans,
8. move/change the gratings when needed,
9. export the acquired spectra to ASCII file format for further analysis,
10. import the ASCII file of spectrum for simple analysis or comparison of data

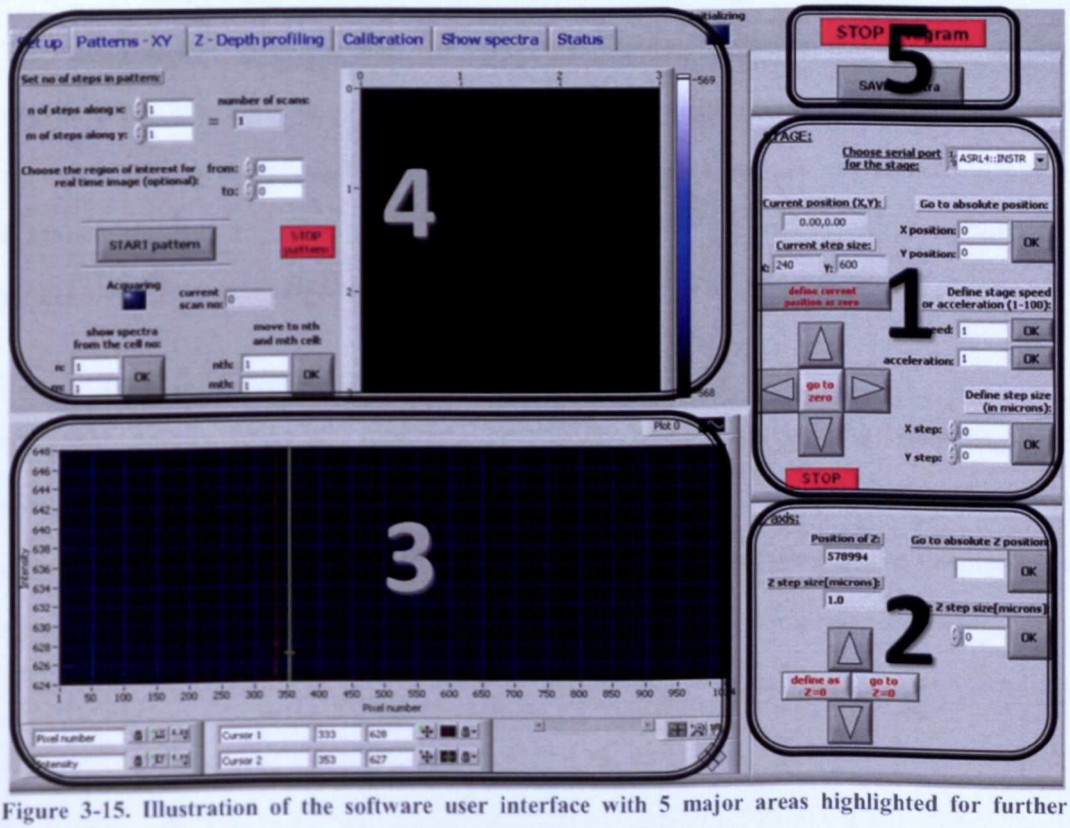

Figure 3-15. Illustration of the software user interface with 5 major areas highlighted for further explanation.

3.4.1 The XY-Stage control (1)

The XY stage is attached to the microscope platform and used to control the movement of the sample above the objective focus. In our system we use a ProScan™II Motorized XY Stage System (Prior Scientific Instruments Ltd. , Fulbourn, UK), which has sub-micron resolution (the smallest step size is 40nm), ±1 μm precision, high speed and wide travel distance (7 cm x 11 cm). The stage

is ideally suited for imaging applications where high precision and accuracy are essential. The ProScan II microscope stage is connected via a serial port to the computer and controlled using drivers provided by manufacturer.

3.4.2 The Z-Control (2)

The stepping motor and a motor controller can be attached to the focussing knob of the microscope (H122 Focus Motor, Prior Scientific Instruments Ltd., UK). This feature is useful for depth measurement in confocal setup with accuracy of 0.1μm.

3.4.3 The Display (3)

The display section shows the most recent spectrum acquired by the system. The vertical axis represents the intensity (count) of the spectrum while the horizontal axis represents the pixel number which may be replaced by the Raman shift or Wavelength when the appropriate calibration is applied. The spectrum can be zoomed in or out and two cursors (red and yellow) are available for further investigation of the spectrum (e.g. to measure the position of certain peaks in the spectrum).

3.4.4 The Configuration and Acquisition Tabs (4)

The panel comprised of six selection tabs: set up, patterns-XY, Z-depth profiling, calibration, show spectra and status. These tabs allow users to set up experimental parameters, such as, the CCD exposure time, the area of the scan etc. Figure 3-16 illustrates each of these tabs. A description of the controls, displays and their functions for each tab are detailed in the following section.

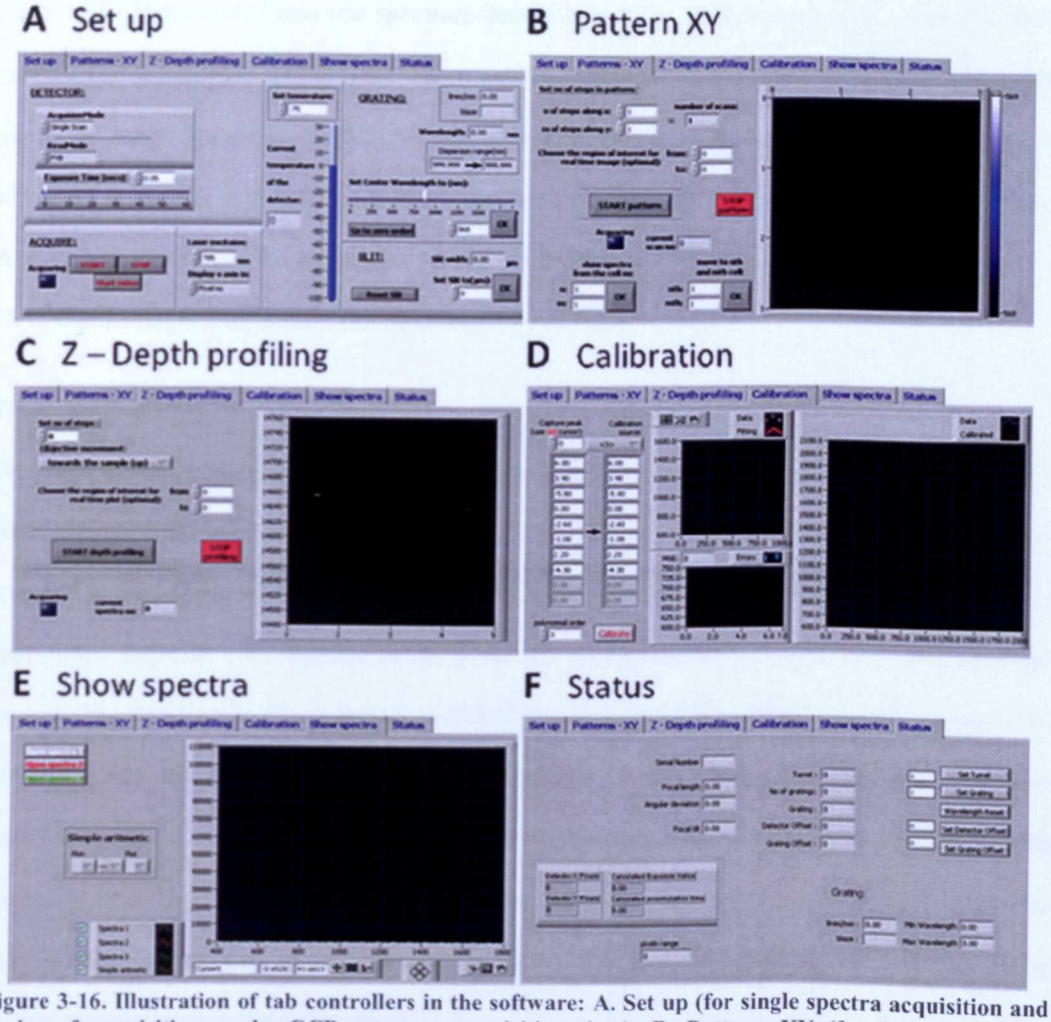

Figure 3-16. Illustration of tab controllers in the software: A. Set up (for single spectra acquisition and choice of acquisition mode, CCD setup or acquisition time); B. Patterns-XY (for Raman spectral images); C. Z-depth profiling (for acquisition of spectra with different position of the focus); D. Calibration (for calibration of x-axis); E. Show spectra (for primary analysis of acquired spectra: visual and basic arithmetic methods between spectra) and F. Status (showing status data of the detector, spectrometer and the microscope stage).

The set up tab

The first tab control is the setup where the controls are categorized into four main groups: the CCD configuration, single spectra acquisition, temperature control and spectrograph configuration parameters such as gratings and slit width. The CCD configuration allows users to change the measurement configuration with the acquisition mode, the read mode, and the exposure time. The acquisition mode can be switched between single scan, where the CCD performs single measurement, and accumulation where more than one spectrum is collected in a single measurement. The read mode allows users to configure how the collected data is read from the CCD. There are three modes available, FVB (full vertical binning), where the values of all vertical

pixels of CCD are stored into one spectrum data, single track, where data is read from a selected track of pixels specified by the track centre and track height parameters and finally image mode, where the image appearing on the CCD panel is acquired. The exposure time control is used to adjust the collecting period for each single measurement. The temperature control allows users to manage and to monitor the temperature of the CCD cooling system. The default temperature is -75°C, but the target temperature can be changed by the user.

The pattern tab

The stage is used in micro-Raman mapping measurements to move the sample across the excitation laser, thus the Raman spectra can be collected from different positions and processed to create a image. The movement of the stage is made in a raster pattern (Figure 3-17). The user selects an appropriate step-size (this equates to the pixel size in Raman images) and the speed on stage control. The step-sizes in the x- and the y-directions can be set independently as well as number of pixels in every direction. The number of steps (pixels) in X and Y and acquisition time over every step has to be set in the tab controls. After the measurement the user can load a single Raman spectrum from different positions of the pattern by giving appropriate x- and y- coordinates. Additionally, the stop pattern control is an emergency buttons allowing the user to stop performing further measurement in the pattern scan.

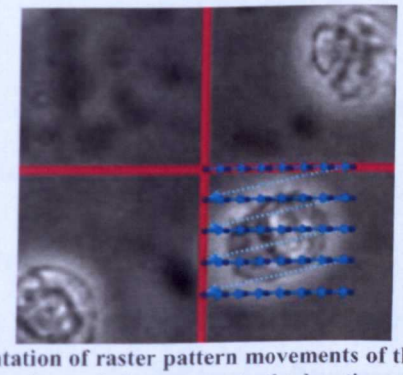

Figure 3-17. Schematic representation of raster pattern movements of the microscope stage (in blue) set over the image of the cell. The red crosshair represents the location of the laser focus at the starting point of the pattern.

The Z-profile tab

Depth measurements of the sample can be needed in some experiments and this feature allows automatized acquisition of spectra with different vertical positions of the focus. The plotting of area

under pre-chosen Raman band is possible simultaneously and the objective movement can be made both towards and away from the sample.

The Calibration

The default unit in the horizontal axis is the pixel number; however, users can transform this unit into the Raman shift or wavelength by applying the correct calibration. To carry out the calibration, users need to collect a Raman spectrum from samples were the Raman bands are well-defined, for example, Tylenol. Then, the pixel numbers corresponding to the wavelength column need to be entered into the pixel number column in the table. In the software the predefined values of 10 peaks for 4 samples are available (Tylenol, BSE, naphthalene and polystyrene). However, the user could choose a different sample (for example Hg lamp) and less calibration points. After setting up the order of polynomial function and clicking on the calibrating button, the software will calculate the coefficients as well as showing the result in the text box area along with original and calibrated spectra on the tab display. The calibrated axis is applied to the display automatically.

The simple analysis

The "show spectra" tab allows users to load recent spectrum (mean of all spectra when the pattern loaded) or saved spectrum files in order to compare spectra visually and/or perform simple arithmetic (+, -, *, /) analysis. Up to 4 different spectra could be loaded.

The status

The status tab displays status data for the detector, spectrometer and the microscope stage. This tab can also be used to change gratings on the motor turret.

3.4.5 The Save and Stop Program controls (5)

Save control is used for saving both patterns or single spectra depending which tab is open (single spectra or Raman image). The stop program button allows turning off the software without damaging CCD (the temperature of the chip is rise up in controlled manner).

3.4.6 Pros & cons of the software

The software development was an incremental process with step-by-step testing used to attain the best performance. The CCD camera cooling and single measurements in every mode (image, FVB and single track) can be performed very well, with the latter working in both single or accumulation approach. The software also functions well in pattern mode as well as in Z-profiling setup examples of results obtained in both of these modes are shown in Figure 3-18 and Figure 3-19. The pattern scans are performed on polystyrene bead using a large step size (1 μm) Figure 3-18A and small step size (0.25 μm) Figure 3-18B. Z-profilling data is shown for two different samples: oil layer (step size 1 μm) and a polystyrene bead (stepsize 0.5 μm) Figure 3-19A and B respectively.

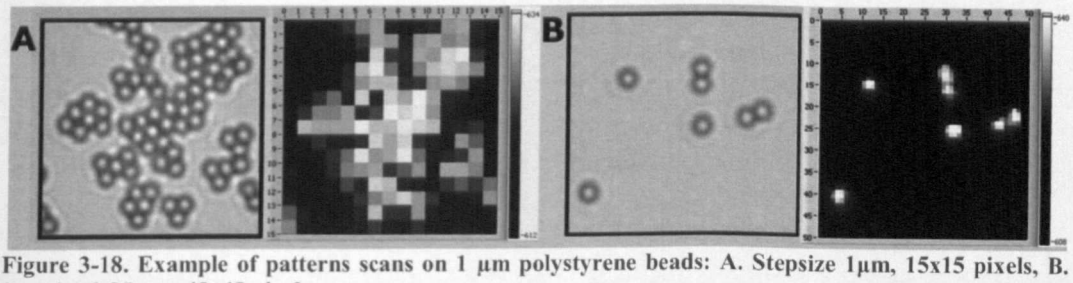

Figure 3-18. Example of patterns scans on 1 μm polystyrene beads: A. Stepsize 1μm, 15x15 pixels, B. Stepsize 0.25 μm, 48x48 pixels.

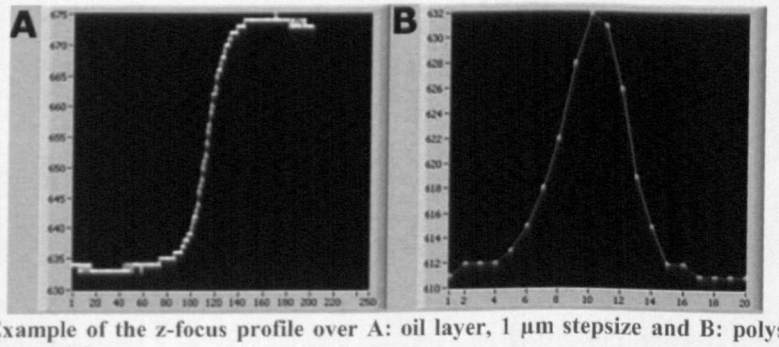

Figure 3-19. Example of the z-focus profile over A: oil layer, 1 μm stepsize and B: polystyrene bead, focus moved every 0.25 μm.

Despite the functionality of the software an undesirable delay is added to each measurement during data acquisition in scanning pattern mode. The delay is currently of the order of ~300ms and probably is related to communication between stage - computer and detector - computer during the scan. This delay slows down the software performance which can dramatically extend the duration of the experiment and in some cases affect the results. Furthermore, faster software implementation

would allow larger sizes of pattern scans to be performed and allow high resolution images to be obtained. Some components in the software need to be redesigned in order to reduce the delay and solve this problem.

Chapter 4.

Performance of the Raman micro-spectrometer and data analysis

"We are stuck with technology when what we really want is just stuff that works"

Douglas Adams (1952 – 2001)

In this chapter performance of the system in terms of spatial and spectral resolution will be shown and experimental techniques will be discussed. The latter include the wavenumber calibration of the spectrometer, which has to be applied before every experiment, the sample retro-positioning method in order to find exactly the same cells for investigation with supplementary techniques and an explanation of spectra processing and data analysis methods.

4.1 Confocal parameters of the system

In Raman micro-spectroscopy the object is illuminated through a high magnification objective and examined by the same objective. The total scattered light is therefore influenced by the structural details of the object, such as the dimensions and changes in refractive index within the studied specimen. In our case the objects under investigation are cells, which are larger than the beam diameter. Refractive index of cells varies due to organelles, types and biochemistry. In average the refractive index of cytoplasm, which fills most volume of the cell, is ~1.360 [9] .

In a Raman microscope all scattered light from the illuminated region of the sample will be detected by CCD. The confocal setup uses a pinhole in front of the detector to produce field-stop and eliminate out-of-focus light. The image quality is usually improved in both the lateral and axial plane. Figure 4-1 shows schematically the blocking of out-of-focus light in the confocal configuration. The lateral resolution is influenced by the field-stop which shortens the field of view for the detector and the axial resolution is determined by reduction of out-of-focus signal.

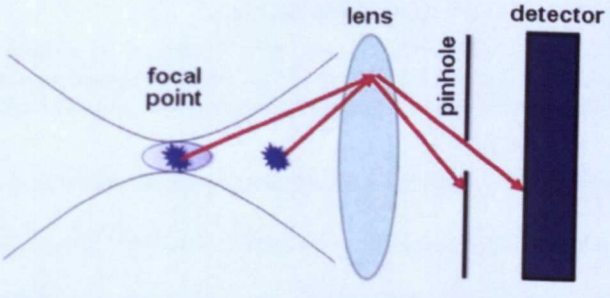

Figure 4-1. Schematic illustration of blocking out-of-focus light by pinhole.

The choice of pinhole depends on the spatial resolution desired and signal intensity. A smaller pinhole improves resolution but reduces the amount of light at the detector, thus reduces signal strength. Apart from improving resolution, the pinhole has the benefit of reducing the background signal originating from the cells surrounding. Figure 4-2 shows Raman spectra of a typical cell in two different setups: conventional (without pinhole) and confocal (with 150μm pinhole). Both spectra were taken with an acquisition time of 3 seconds. The signal drop in confocal setup is significant in comparison to the conventional one, but also the background and baseline is enormously reduced. For better recognition of confocal setup ability the spectra is zoomed in and

displayed in the smaller window in Figure 4-2. For non-confocal setup the spectrum lies on a high background and two peaks corresponding to the quartz coverslip are observed (marked with asterix). However, the spectrum obtained by the confocal setup has a flat baseline and no peaks from the surroundings of the cell are seen.

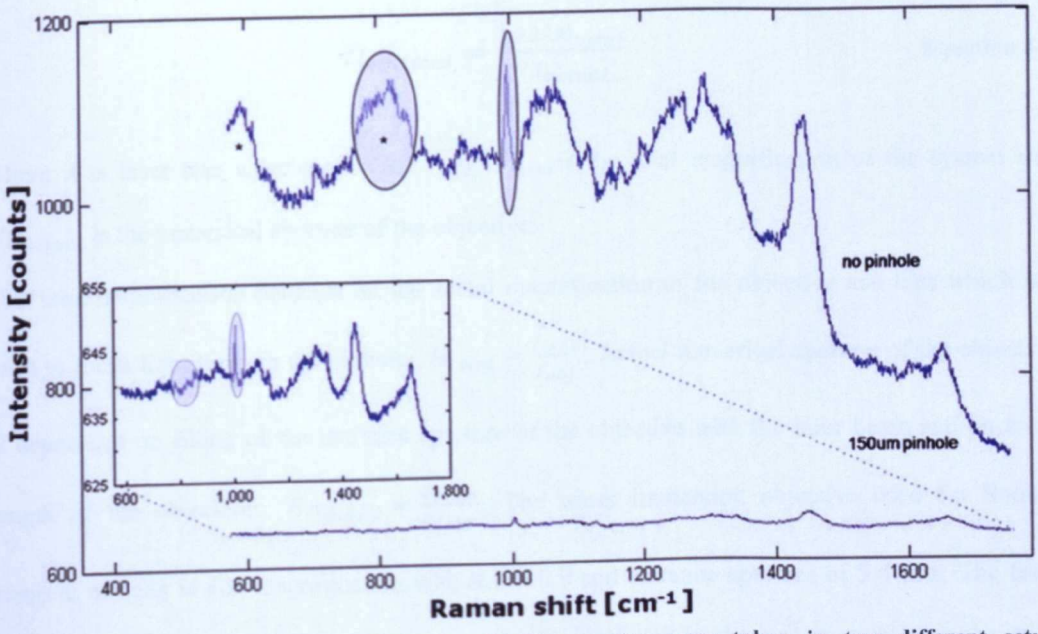

Figure 4-2. Raman spectra of a typical cell. The spectra were taken in two different setup arrangements: conventional, without pinhole and confocal, with 150 μm pinhole (+ zoomed in spectrum is displayed in the smaller window). The spectra are shown as a raw data, without any processing.

To compare the reduction of the background signal, the ratios of a peak corresponding to the cell and of quartz were calculated. The peaks chosen were the ring breathing mode of phenylalanine (1003 cm^{-1}), which is sharp and narrow peak originating from proteins contained inside the cell and the second broad peak originating from quartz (Si-O-Si asymmetric stretch [160] at ~800 cm^{-1}), as a measure of background. The peaks are marked with circles on the Figure 4-2. The ratios obtained were 0.76 for conventional micro-spectrometer and 3.928 for confocal setup with 150 μm pinhole in place. This result means that background contributions are cut off enormously in confocal system even with a relatively large pinhole.

The choice of pinhole size in confocal Raman spectroscopy is a balance between signal intensity and resolution desired. In the case of Raman imaging of cells the purpose of confocal setup was mainly reduction of surrounding background and improving the resolution in z-axis. The first

confocal arrangement used a pinhole and two lenses (condensing and collecting). In a later design, fibre optics of different diameters was used to offer higher stability of the system.

The choice of the pinhole or fibre optics diameter depends on the wavelengths and optics used in the system. The optimal pinhole can be calculated by:

$$D_{optimal} = \frac{1.22\lambda M_{total}}{NA_{actual}} \qquad \textbf{Equation 4-1}$$

where λ is laser line wavelength (785 nm), M_{total} is the total magnification of the system and NA_{actual} is the numerical aperture of the objective.

The total magnification depends on the actual magnification of the objective and lens which are used to focus light through the pinhole: $M_{total} = \frac{f_{lens}}{f_{obj}}$. Actual numerical aperture of the objective is dependent on filling of the entrance aperture of the objective with the laser beam and on focal length of the objective: $NA_{actual} = \frac{d_{beam}}{2f_{obj}}$. The water immersion objective used for Raman imaging of cells is 60x magnification with $NA = 0.9$ and entrance aperture of 5.4 mm. The laser beam diameter is 2.2mm but the beam expander is employed in the system to enlarge the laser beam before the objective to ~4 mm. Focal length of the objective is given by $f_{obj} = \frac{tube\ length}{magnification} = \frac{180mm}{60} = 3mm$. Subsequently, $M_{total} = 66.66$ for conventional confocal setup ($f_{lens} = 200\,mm$), and $M_{total} = 13.33$ for fibre-based confocal setup (focal length of focussing lens is $f_{lens} = 40\,mm$). Actual numerical aperture of the objective equals 0.66.

Consequently, the optimal sizes of the pinhole are 95.77 μm and 19.15 μm for conventional and fibre-based setup respectively. Additionally, it should be taken into account that the wavelength of Raman signal of interest is slightly higher than the excitation laser line (scattered Stoke shifted Raman light in the fingerprint region falls between 820-920 nm) and theoretical formula applied here consider perfect Gaussian laser beam and optics without any spherical aberrations. Therefore the optimal size of pinholes should also be slightly larger than the theoretical values. For that reason the pinholes we have taken for consideration for imaging the cells were 100 μm and 150 μm for conventional and 25 μm and 50 μm for fibre-based confocal setup.

The 50 μm core fibre was used in the experiments presented in this thesis as it was found to give the best balance between signal-to-noise ratio achievable in 1 s acquisition time and the resolution. The short acquisition time is important for imaging of cells. For comparison, cell spectra obtained with 25 μm and 50 μm fibre optics core is shown in Figure 4-3

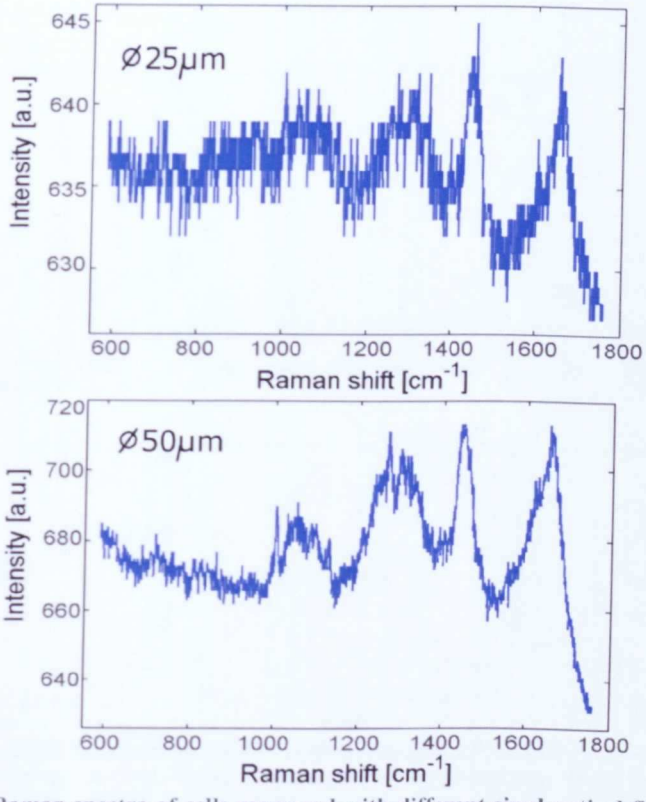

Figure 4-3. Typical Raman spectra of cells measured with different sized optical fibres of 25 μm (top) and 50 μm (bottom) (acquisition time of 1 s).

4.1.1 Spatial resolution

Spatial resolution describes the ability of an imaging system to resolve spatial detail in the object. It is important to measure the spatial resolution of the Raman micro-spectrometer and its ability to distinguish features in both axial (z-plane) and lateral (xy-plane) dimensions. The resolution can be obtained experimentally in various ways.

The results presented in the following sections were measured for three different experimental arrangements of SETUP 3 (Figure 3-13). This was the non-confocal arrangement (without pinhole) and confocal arrangement with two pinhole sizes: 100 μm and 150 μm.

Axial resolution

There is still no consensus on how best to measure the axial resolution in confocal Raman microscopes. Therefore, three different samples were measured to obtain axial (Z-axis) resolution of the spectrometer: thin layer of oil, flat graphite surface, and 1 μm size polystyrene beads (Sigma Aldrich, UK).

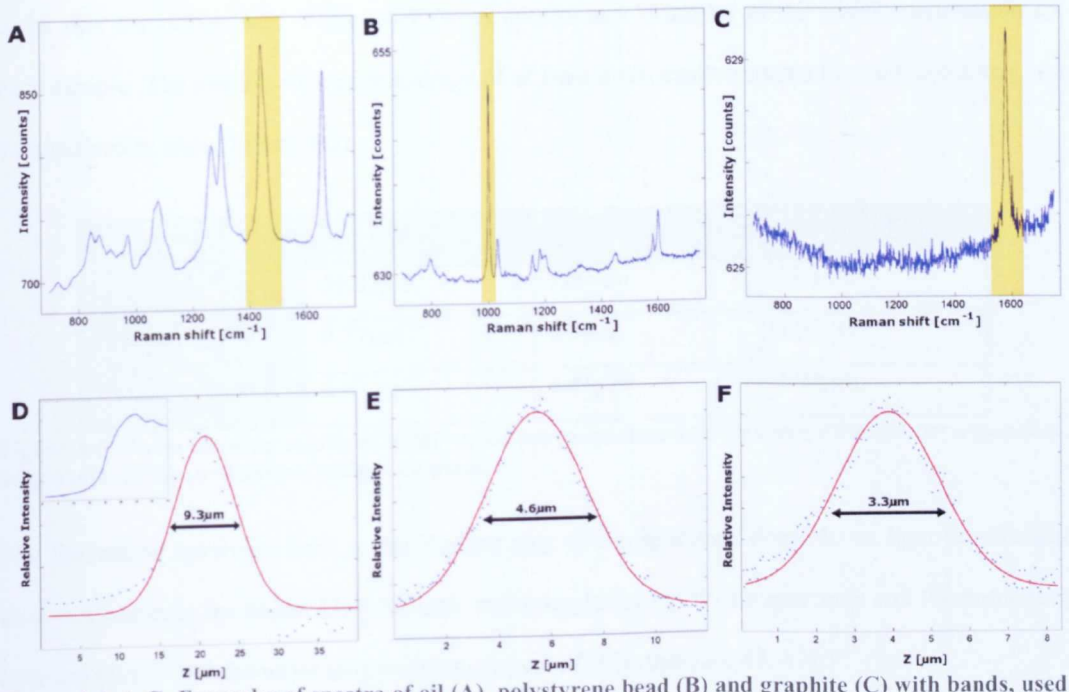

Figure 4-4. A-C: Examples of spectra of oil (A), polystyrene bead (B) and graphite (C) with bands, used to obtain response curves for the Raman spectrometer (highlighted): D-F: response curves and calculated FWHM for: D – oil (1st derivative, inset = raw data), 150 μm pinhole, stepsize 1 μm; E – polystyrene bead, pinhole 150 μm, stepsize 0.1 μm; F – graphite, pinhole 100 μm, stepsize 1μm

Oil is a transparent material and maximum signal intensity will be collected when the laser focus is somewhere in the middle of the layer, as the largest contributions will result from places around the laser focus. Oil was chosen as transparent material with matching refractive index for the coverslip. This approach avoids spherical aberrations when refractive index mismatch is encountered. Graphite on the other hand is opaque and has a quite reflective surface, which means that the Raman signal will be maximum when the scattered light is collected from the light focused on the surface. The last sample, polystyrene beads, is especially important as it is the most related to probing organelles inside cells. It is a good approximation to a point object, as the signal from a bead drops much quicker when moved out of the focus plane than in planar objects (oil and

graphite). This is because there is no contribution from the regions directly above or below the bead. Therefore when working with bigger objects, e.g. tissues, the resolution determined with small particles could be underestimated.

The FWHM of the most intensive vibrational peak areas measured. Depending on the sample and response curve obtained, the resolution was determined by the FWHM of the data (graphite, bead) or its first derivative (oil). Figure 4-4 shows spectra and examples of the FWHM estimation for each sample. The results, which are average of at least three measurements for each condition, are summarised in table (Figure 4-5)

	oil layer	polystyrene bead	graphite surface
no pinhole	50.35μm	7.42μm	43.3μm
150μm pinhole	9.77μm	5.3μm	5.67μm
100μm pinhole	6.82μm	4.41μm	2.98μm

Figure 4-5. Table showing results of axial resolution of spectrometer in three different arrangements: no pinhole, 150μm and 100μm pinhole on place.

The theoretical resolving limit in the Z-plane axis of the specimen depends on light wavelength used to illuminate the object (λ_0= 785nm), refracting index (η) of the specimen and the numerical aperture (NA = 0.90 for water immersion objective) of objective [20, 48, 49]:

$$z_{min} = 2\frac{\lambda_0 \eta}{(NA)^2} \qquad \textbf{Equation 4-2}$$

Taking into account the refractive indices of oil ~1.47 [161], and polystyrene ~1.59 [162] the calculated values for z_{min} are 2.8μm and 3.1μm respectively. Due to the opaque and lustrous nature of graphite a refractive index cannot be obtained [163]. Nevertheless, the assumption was that amongst the tested samples the axial resolution would be the smallest for graphite, which was proved experimentally. Additionally, it has to be stated that quartz slide on which polystyrene beads and oil layer rest was not taken to the account. Furthermore, the average refractive index of cell cytoplasm is 1.360 [9], thus theoretical z_{min} for cell measurements is 2.6 μm.

In conclusion, the resolution along the axial direction is strongly improved by confocal arrangement. The obtained value was close to the theoretical value when the 100 μm pinhole was used. These results in terms of axial resolution fulfil our requirements, since adherent cells are generally < 5 μm in height. Consequently, most molecules in cell volume will be within the laser focus. However, this does not allow measurement of Raman spectra at different depths inside living cells.

Lateral resolution

The theoretical laser spot size in the sample plane depends on the beam quality of the laser and on the focussing optics in the system. The diameter of the laser spot on the sample is given by:

$$S = \frac{4(M^2)\lambda_0 f_{obj}}{\pi d_{beam}} \qquad \textbf{Equation 4-3}$$

where M^2 is the quality factor of the laser beam, λ is the laser wavelength (785 nm), f_{obj} is the focal length and d_{beam} is the laser beam diameter at the entrance of the objective. The M^2 of the laser used in our system was 1.7. Therefore, the calculated diameter of the laser spot on the sample with 60x water immersion objective and beam enlarged with the beam expander is 1.2 μm. The laser spot size on the sample determines the size of the scanning volume; however, this value does not represent the achievable lateral resolution. The numerical aperture of the system and the laser wavelength has to be considered when verifying lateral resolution.

The resolving power of the optical system of infinity small object points is itself limited by Airy diffraction discs. This is seen as central bright disc with progressively weaker concentric dark and bright rings [20, 48, 49]. The radius r_{Airy} of first dark ring depends on wavelength (λ_0) used to illuminate the object and numerical aperture (NA) of the objective:

$$r_{Airy} = 0.61\frac{\lambda_0}{NA} \qquad \textbf{Equation 4-4}$$

The Rayleigh criterion states that when the distance (d) between two equally bright points is greater or equal to the Airy radius, $d \geq r_{Airy}$ the points can be resolved [48]. The calculated Airy

radius for our system for water immersion 60x magnification objective was 532 nm (NA = 0.9) or 719 nm when actual NA = 0.66 is taken to account (objective entrance not fully-filled with light).

The lateral resolution was measured experimentally by obtaining Raman images of 1 μm polystyrene beads. Varieties of stepsizes (this dictates the pixel size in the image) were applied for each setup ranging between 250 nm and 1 μm. The images were produced by plotting the area of the sharp polystyrene Raman band of 1004 cm^{-1}. Figure 4-6 shows typical Raman images produced by different stepsizes with a 'no pinhole' spectrometer arrangement.

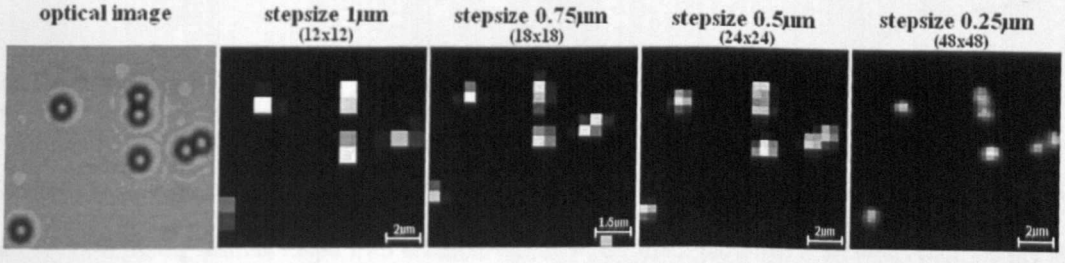

Figure 4-6. Optical image and Raman micro-spectroscopy images of polystyrene 1μm beads on quartz. The Raman images are colour coded intensities (peak areas) of the 1004cm^{-1} band.

The response curves of spectrometer can be revealed by choosing appropriate lines in the Raman images of polystyrene beads and then used to calculate the resolution in X and Y axis. Examples of these curves and estimations of the resolution (FWHM calculations) in the planar axes are shown at Figure 4-7. These images show that for a step size of 0.25 μm neighbouring 1 μm polystyrene beads can be still distinguished in the Raman images.

Nevertheless, when comparing the curves measured with different pinhole sizes (100 μm, 150 μm or no pinhole) and FWHM obtained from these different arrangements no noticeable improvement was obtained. This could be due to the specimens chosen, which were too big (1 μm diameter) to be on the edge of the resolution capability of the spectrometer. However, this evaluation is relevant to cell studies as the organelles within the cells which will be studied are usually > 1 μm. The lateral resolution measured was (1 ± 0.2) μm.

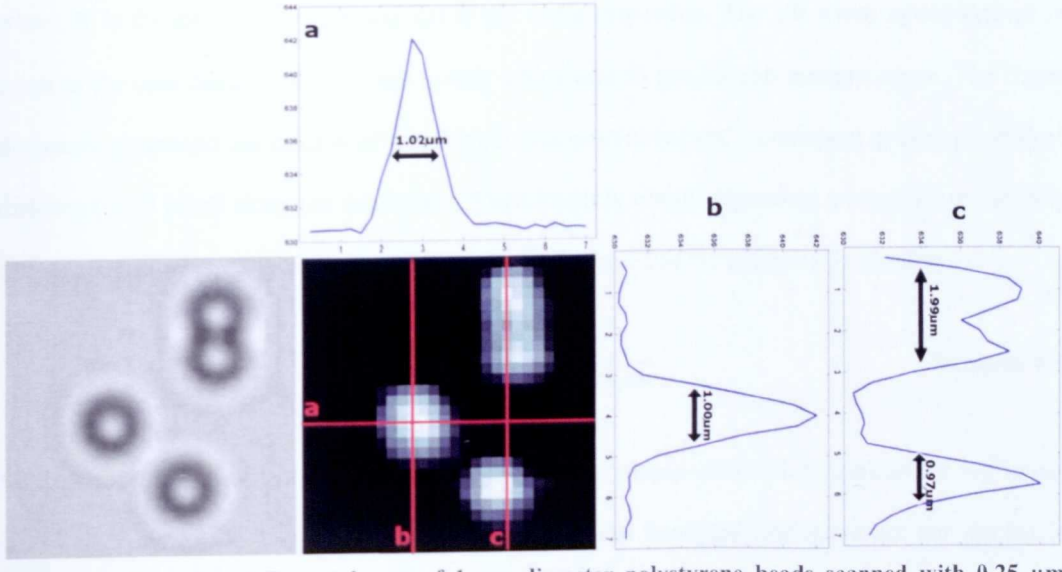

Figure 4-7. Optical and Raman image of 1 µm diameter polystyrene beads scanned with 0.25 µm stepsize. Profile curves of spectrometer produced in X and Y plane (150 µm pinhole).

Although the measurement of XY resolution were not performed on the small enough particles the ability of building Raman maps with different stepsizes on small particles is shown. Additionally it is revealed that the lateral resolution of the Raman system is ~1µm and fulfils our target resolution for live cells imaging.

4.1.2 Spectral resolution

The spectral resolution is a measure of the spectrometer ability to resolve features in the Raman spectrum. There is a limit on how close two Raman bands can be before they cannot be differentiated from each other and are just seen as one large band. Spectral broadening could be determined from the spectrometer's entrance (i.e. slit width) and the grating groove density (lines/mm). Spectral resolution increases as groove density increases, but at the expense of spectral range and signal strength, and also as slit width decreases, but at the cost of signal strength [48, 115].

Both the bandpass and FWHM of the wavelength resolution are used as an estimation of an instrument's ability to separate adjacent spectral lines. The bandpass can be calculated by following:

$$BP = W * LD \qquad \text{Equation 4-5}$$

where W is the slit width in μm and LD is the linear dispersion. The slit width in our system is equal to the core diameter of the fibre optics, which was 50 μm for cell measurements. The linear dispersion represents the number of wavelength intervals (nm or cm^{-1}) contained in each interval of distance (CCD pixel) along the focal plane. Therefore it is simply dependent on spectral range (SR) and size and number of detector elements in the focal plane. For our system it is equal to:

$$LD = \frac{SR}{1024*26\mu m} \qquad \text{Equation 4-6}$$

SR depends on the gratings resolving power and can be simply obtained by subtracting beginning from end value of the x-axis of measured spectrum. The bandpass calculated for our system is 0.17 nm (2.2 cm^{-1}).

The FWHM of the instrumental profile can also be measured experimentally by measurements of spectral emission lines of mercury-argon calibration lamp. Figure 4-8 shows the spectrum of the calibration Hg-Ar lamp with FWHM of the bands obtained. The mean value of the experimental calculation of the spectral resolution is 0.18 nm (2.33 cm^{-1}), which is very close to the calculated bandpass.

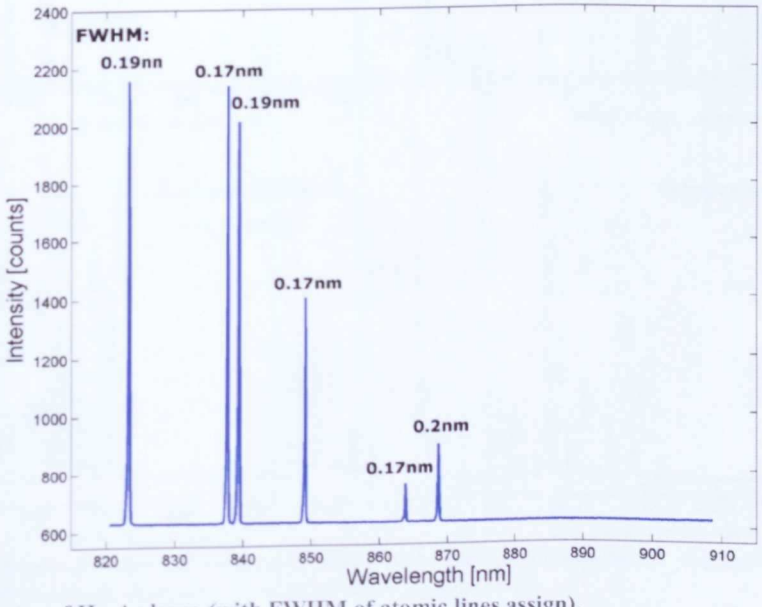

Figure 4-8. Spectra of Hg-Ar lamp (with FWHM of atomic lines assign).

4.2 Spectral calibration

The Raman spectrograph must be calibrated to ensure that the light scattered from the sample is correctly represented on the detector in terms of the wavenumber axis. There are two common methods for spectral calibration. The most conventional is to calibrate it against a spectral discharge lamp, based on absolute frequency standards, while mercury and argon lamps are the most common choices. Their emission lines are accurately known. Determination of the Raman shift with absolute wavelength standards requires the subtraction of two frequencies, those for the laser line used and for Raman scattering. However, the wavelength of a diode laser can vary slightly with temperature, therefore calibration inadequateness can occur due to laser wavelength variations [48, 164]. Therefore, it was preferable to calibrate the system against a reference material, whose Raman spectrum has been carefully measured.

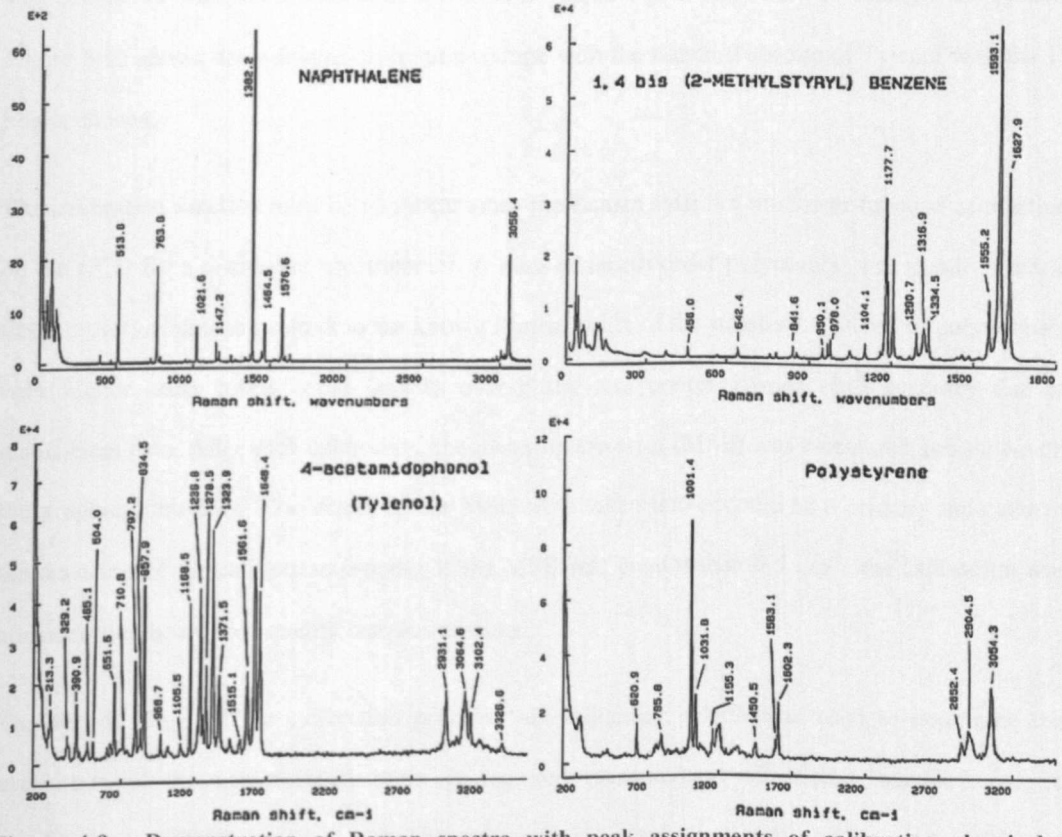

Figure 4-9. Demonstration of Raman spectra with peak assignments of calibration chemicals: naphthalene, BMB (Sigma-Aldrich), Tylenol and polystyrene [165].

Raman shift standards have the advantage of not depending on accurate knowledge of the laser frequency as Raman shift does not depend on the laser wavelength used. The American Society for Testing and Materials (ASTM) has adopted eight materials as Raman shift standards (ASTM E 1840) [165]. Four of those chemicals: naphthalene (Sigma-Aldrich), 1,4-bis(2-methylstyryl)benzene (BMB) (Sigma-Aldrich), 4-acetamidophenol (which has active ingredients of Tylenol) (Sigma-Aldrich) and polystyrene, were considered for calibration standard. The spectra of these chemicals with peaks indicated by the ASTM are showed in Figure 4-9.

The standard materials were tested under the same experimental conditions as subsequent experimental samples and cover at least the Raman shift range of interest when studying cells. Since Tylenol has sharp intense peaks that are relatively well distributed in the region of interest (see Figure 4-9 for comparison), the Raman shift calibration procedure for experiments on cells was completed with this chemical as a standard. Ten data points are used to calibrate the system. Figure 4-10 shows the software calibration routine with the standard spectra of Tylenol with the 10 points chosen.

The calibration function must be nonlinear since the Raman shift is a nonlinear function of position on the CCD for a dispersive spectrometer. A third or fourth-order polynomial was usually used to fit the observed detector output to the known Raman shifts of the standard. The use of polynomials with higher order terms could lead to over-fitting and poorer Raman shift accuracy due to insufficient data. After each calibration, the mean square error (MSE) was calculated and shown on the graphical interface. The values of the MSE were taken into account as a primary indicator of the accuracy of the calibration process. If the MSE was greater than 0.5 cm^{-1}, the calibration was considered to be of poor quality and was repeated.

The second stage of the calibration process was validation, which was used to determine the magnitude of the experimental error. It required measurement of another standard sample (naphthalene or BMB, usually both). This validation indicated an accuracy of the peak position of ~0.5 cm^{-1}.

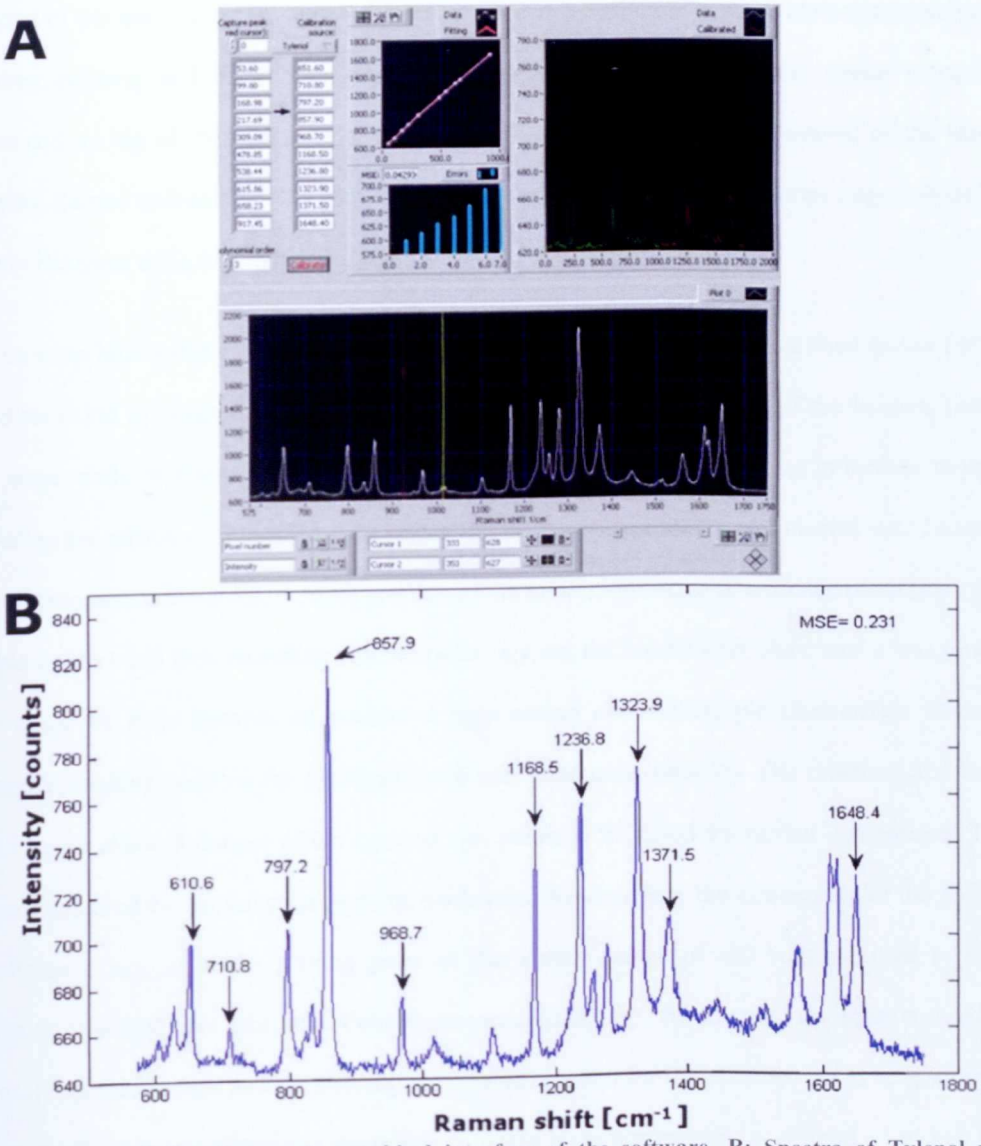

Figure 4-10. A: Calibration mode graphical interface of the software, B: Spectra of Tylenol with assignments of peaks used for calibration in the experimental setup.

4.3 Retro-positioning of samples

For complex samples, such as live cells, Raman spectra are also very complex, making band assignment difficult. One method for validation and confirmation of biochemical findings by Raman studies is to use an independent technique which is well recognized in cell biology. Fluorescence imaging is one of the most common techniques in cell biology, in which high chemical specificity is achieved by using fluorescent labels. Therefore, a wide field fluorescence imaging system was integrated on the Raman microscope system. This allowed fluorescence

imaging of the same cell after completion of the Raman measurements. The fluorescence technique requires staining and very often membrane permeabilization procedures, which cannot be performed on top of the microscope. Consequently, a protocol involving removal of the sample from the Raman microscope, labelling as required, replacing it on the microscope stage and finding exactly the same cells, had to be developed.

The purpose-built sample chambers for cell studies were manufactured as described earlier (details could be found in chapter 3, section 3.2.2: Sample holder). At the bottom of the holders, precise cuts were made to allow repositioning of the sample. The retro-positioning procedure required recording the positions of studied cells before the Raman measurement was carried out. To assign the primary axis defining $x_0y_0 = (0, 0)$ position of the microscope stage in a chosen place (the cut on sample holder) and then recording another point- x_1y_1 on the holder with other marks was crucial. This could be done because an additional light source allowed sample illumination from the underside, making possible the examination of non-transparent samples. The crosshair and bright field camera allowed images of the x_0y_0 and x_1y_1 points to be saved for further comparison. Then measurements of the chosen cells could be performed. Nevertheless, the information of the position coordinate (x_{cell} y_{cell}) of the starting point of the Raman image of cell was recorded to allow allocating this cell later (for wide-field fluorescence imaging). Afterwards, the sample could be taken off the microscope and the staining procedures required for fluorescence could be performed. Following the new coordinates of the reference marks were determined ($x'_0y'_0$ and $x'_1y'_1$) and the cells found by calculating the corrected position (x'_{cell} y'_{cell}) of the cell on this new axis of microscope stage:

$$x'_{cell} = x_{cell} \cos \propto - y_{cell} \sin \propto \qquad \textbf{Equation 4-7}$$

$$y'_{cell} = x_{cell} \sin \propto - y_{cell} \cos \propto \qquad \textbf{Equation 4-8}$$

where

$$\propto = \tan^{-1}\left(\frac{y_1' - y_0'}{x_1' - x_0'}\right) - \tan^{-1}\left(\frac{y_1 - y_0}{x_1 - x_0}\right) \qquad \textbf{Equation 4-9}$$

Precision of this retro-positioning method was found to be ~ 5 μm and is well suited for the cell studies as measured cells have diameters of ~10 – 60 μm.

4.4 Analysis of Raman spectra

The application of various statistical algorithms for processing spectra to gain practical information is performed in a vast number of spectroscopic techniques including Raman spectroscopy. In most cases some pre-processing of the spectral data is sufficient to improve visualization. But in most cases, especially when analysing large data sets, a more advanced statistical approach has to be applied. Pre-processing of the data still has to be applied before employing more complex data analysis.

Functions written in the Matlab (The MathWorks, Inc.) programming language are utilized for both the pre-processing of the data and further analysis. Most of these functions have been written in-house by members of our research group. The others are taken from toolboxes provided with Matlab.

4.4.1 Pre-processing of the data

Pre-processing depends on the quality of spectra. If a long acquisition time is used or a strongly Raman active sample is measured (e.g. polystyrene) there is no need for smoothing or improving signal-to-noise ratio. If short acquisition times are applied, like for cell imaging, the signal to noise ratio will be lower, therefore noise reduction and/or smoothing is required. In the Figure 4-11 Raman spectra of a cell measured at four different points is shown during different stages of data pre-processing.

Cosmic rays

Cosmic rays or spikes are high and narrow peaks generated by high energy particles inadvertently hitting the CCD detector. They have to be removed prior to any data analysis. Removals are quite easy to apply as the cosmic spikes are usually very narrow bands and it does not affect the position and intensities of the Raman peaks in the original data.

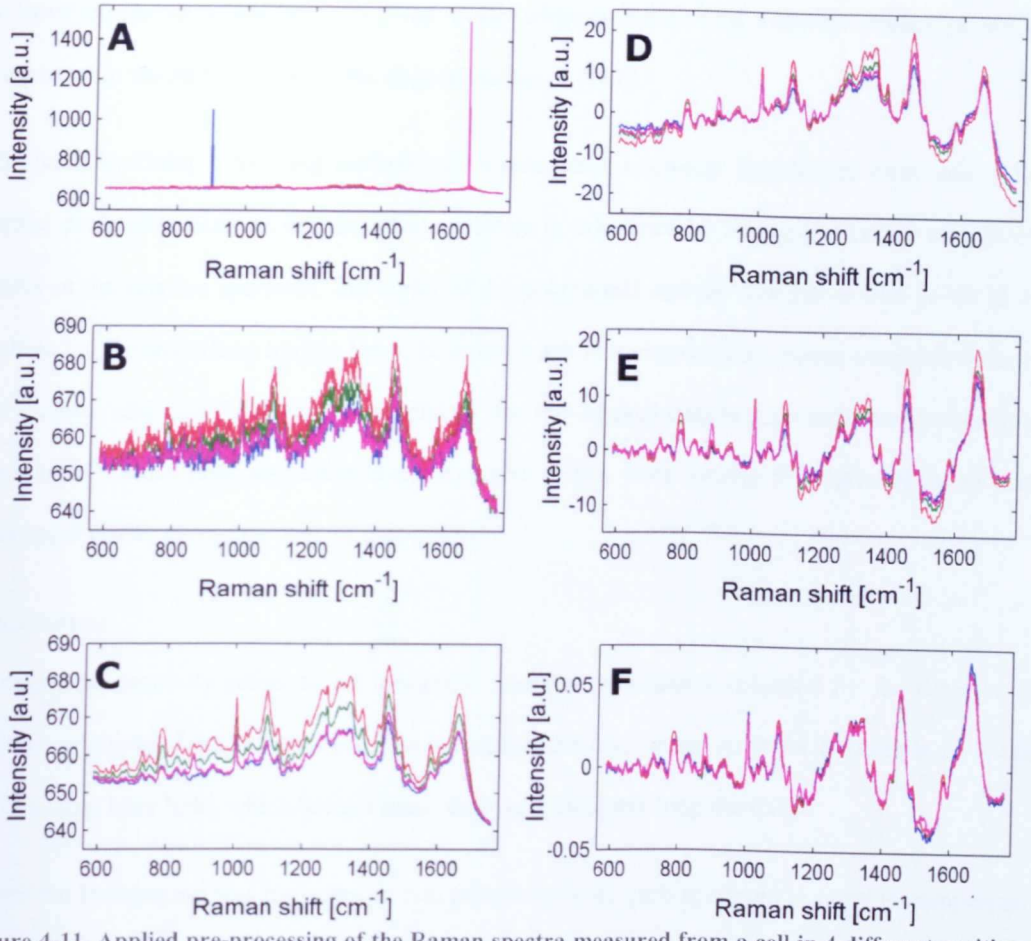

Figure 4-11. Applied pre-processing of the Raman spectra measured from a cell in 4 different positions with 1s acquisition time. A: unprocessed data, two spectra contain cosmic ray; B: after removing cosmic ray; C: after applying singular value decomposition; D: after background subtraction; E: subtracting the baseline; F: after normalization

De-noising and Smoothing

For improving the signal-to-noise (SNR) ratio of spectra, application of de-noising and smoothing routines is generally accepted. Two different methods were used; the singular value decomposition (SVD) and Savitsky-Golay smoothing algorithm. [84, 166, 167].

SVD de-noising is well established method used for image de-blurring and noise removal in spectral data. The noise reduction is applied by suppressing the noise-related components and retaining the signal space only. The SVD is performed on all spectra in the data matrix $A(m \times n)$ by dividing it into orthonormal bases. The singular value decomposition of a matrix is $A = USV^T$, where $U(m \times m)$ and $V(n \times n)$ are orthogonal matrices, and $S(m \times n)$ is a diagonal matrix containing the singular values. Typically, only first few components of SVD are used for preserving the signal

additive components and removing the noise additive ones. This reduced decomposition is performed in the matrix U and in the singular values S [167].

The Savitsky-Golay smoothing method uses a selectable, nonlinear function on each side of the central peak; each point in the smoothed spectrum is calculated by taking an average of adjacent points in the original spectrum. The order of the polynomial and the number of data points to be included in the smoothing routine has to be determined. It is important to choose a suitable order of polynomial, and also the averaging points, so that the original data is not over-smoothed and the position of Raman peak intensities is not changed. In this work usually 5^{th} degree of polynomial was applied with averaging over 11 data points.

Background

Background generally refers to all unwanted, non-Raman photons recorded by the detector. It usually originates from luminescence (fluorescence, thermal emission) from the sample or optics and on stray laser light, which has not been removed before reaching the CCD.

When the background was measured, it was subtracted from each spectrum in order to compensate for interfering signals originating from the optical elements in the light path. It is important that background spectrum is smooth to avoid adding additional noise to the data. It could be obtained for example by long exposure time or by averaging of several background spectra.

Baseline

Raman spectra of biological samples are typically overlapped on a broad fluorescence background. The baseline correction without changing the position and intensities of the Raman peaks is done by fitting and subtracting a polynomial (usually 5^{th} order) from the spectra.

Normalization

Normalisation is applied in order to reduce the impact of changes in the measuring conditions and instrumentation on the spectra intensity. This can be done by normalizing all the spectra to the same value. In this method, the intensity at each frequency in the spectrum is divided by the square root of the mean of each spectrum. The sum is over all frequencies. The disadvantage of this

method is that the background can make significant contributions to the normalization, therefore it is important to subtract the baseline of the spectra prior to normalization.

4.4.2 Analysis of large data-sets and Raman imaging

The result of Raman spectroscopy is a Raman spectrum which contains many overlapping bands. Hundreds of thousands of spectra account for Raman spectral image and a number of statistical approaches have been developed to analyze these data sets. Nevertheless, still the simplest and fastest approaches are univariate methods. Useful information about composition, secondary structure, and the interaction of, for example, DNA-protein complexes inside the living cells can be obtained from the positions, intensities, and line widths of the Raman peaks in the spectra. Therefore Raman imaging includes direct peak intensity, peak areas or ratio of intensities of pre-chosen bands. The *a priori* knowledge on the sample and Raman band assignment is usually needed to understand and compare the differences between the spectra. However, these methods cannot be applied when the Raman signal is too weak and they do not provide complex information on the sample as only pre-chosen bands are analysed.

Sometimes it is necessary to perform an advanced data analysis taking into account the whole spectral range [168]. The fundamental aim of multivariate analysis is dimensionality reduction. For most Raman experiments the number of observations (sample spectra) in the analysis is very small compared to the number of variables (Raman shifts). The whole set of variables may be regarded as a n-dimensional hyperspace. Data interpretation cannot be made by simple visual examination and alternative approaches are needed. This simplification occurs in one of two ways; using either an unsupervised or a supervised learning algorithm.

Supervised methods are based on existing knowledge of the sample in the construction of models or classes that will correctly associate some or all of the data with a known characteristic. Least square fitting (LSF) is one example of this methodology [169].

The method of least squares assumes that the best-fit curve of a given type (e.g. spectrum measured at a given position) is the one with the minimal sum of the deviations squared (least square error)

from a given set of spectra measured from pure chemicals. The downside of LSF is the extremely high sensitivity to the presence of unusual data points or shifts in the data used to fit a model. One or two outliers can sometimes seriously distort the results of a least squares analysis [49, 170].

Unsupervised methods are used to detect the differences and similarities between spectra. These methods are employed to uncover structure in data and can be used to gather samples into groups or clusters [86, 171, 172]. The well established analysis techniques, which have been successfully used for Raman analysis and spectral imaging of cells, include principal component analysis (PCA), k-means cluster analysis (k-means), fuzzy c-means (FCM) and hierarchical clustering algorithms (HCA).

PCA transforms a number of possibly correlated variables into a smaller number of uncorrelated variables called principal components. As a result, the first principal component reports for as much of the variability in the data as possible and each succeeding component accounts for the remaining variability. The results of a PCA are usually discussed in terms of component scores and loadings [173, 174].

K-means identifies regions of the sample with similar Raman spectra by minimising intra-cluster spectral differences and maximising inter-cluster differences. The main advantages of this algorithm are its simplicity and speed which allows it to run on large datasets. Its disadvantage is that it does not yield the same result with each run, since the resulting clusters depend on the initial, randomly-selected cluster centres [171, 175].

Similarly to k-means clustering, the FCM method starts with an initial guess for the cluster centres, but additionally it assigns every data point a membership grade for each cluster. Next, the cluster centres and the membership grades are updated iteratively based on minimizing an objective function that represents the distance from any given data point to a cluster centre weighted by that data point's membership grade [171, 176-179].

The basic process of hierarchical clustering is as follows: A distance matrix between all spectra is calculated and then most similar pair of spectra (clusters) is found and merged into a single cluster.

Distances (similarities) between the new cluster and each of the remaining objects are computed and the previous step repeated until all items are clustered into a single cluster. The traditional representation of this merging process is a tree-like diagram called a dendrogram. It shows a hierarchy of the grouped spectra, with individual elements at one end and a single cluster containing every element at the other. Cutting the tree at a given height will give a clustering at a selected precision, e.g. if k clusters are needed, just the k-1 longest links have to be cut [171].

The computational requirements of HCA are the major problem. It is especially important when analyzing large data sets as computational effort required scales with the square number of spectra. In comparison, the computational resources required for k-means clustering scales approximately linearly [171]. Thus this method is more efficient and less time consuming for large data sets.

Chapter 5.

Label-free molecular imaging of immunological synapse [1]

"There are two possible outcomes: if the result confirms the hypothesis, then you've made a measurement. If the result is contrary to the hypothesis, then you've made a discovery"

Enrico Fermi (1901–1954)

In this chapter the results of non-invasive chemical imaging of immunological synapses will be shown. Confocal Raman micro-spectroscopy was used to measure spectral images of junctions formed between living dendritic and T cells without using molecular labels or other invasive procedures. In agreement with the gold-standard invasive technique of immune-fluorescence, the Raman spectral images showed polarisation of actin at the immunological synapse junctions.

---

[1] This work was carried out in collaboration with Dr Ramneek Johal, Dr Samuel Garcia-Nieto and Dr Amir Ghaemmaghami from Allergy Research Group, School of Molecular Medical Sciences and Respiratory Biomedical Research Unit, University of Nottingham.

5.1 Introduction

We have used confocal Raman micro-spectroscopy (CRMS) to measure spectral images of immunological synapses formed between dendritic (DC) and T cells without using molecular labels or other invasive procedures. The purpose-built inverted confocal Raman micro-spectrometer allowed measurements on live cells maintained under physiological conditions (37°, 5% CO_2). After laser irradiation and collection of Raman data viability assays were carried out on the same cells using fluorescence staining. The integration of the wide-field fluorescence also enabled direct comparison between Raman spectral images and gold-standard immune-fluorescence images for specific molecules.

Dendritic and T-lymphocyte cells are part of white blood cells and are part of the immune system, which protects the body against both infectious disease and foreign materials by identifying and killing pathogens and tumour cells. The main function of dendritic cells is to process antigen material and initiate specific T-cell responses. In blood these cells can be found in an immature state and become activated in the presence of the foreign antigens (e.g. pathogens) which enter the body. Upon antigen capture DCs migrate to the lymph node where they process and present foreign antigens on their surface associated with major histocompatibility complex (MHC) molecules. T cells which are also present within the lymph node play a fundamental role in the subsequent cell-mediated immune responses that involves activation of the specific T-cells by DC and the release of various cytokines [74, 180] .

When T cell receptors (TCR) interact with the antigen-MHC complex on the DC surface a unique junction is formed between these two cell types known as the immunological synapse (IS). The IS forms a distinct structure also termed supramolecular activation clusters (SMACs). These clusters are composed of a series of concentric rings; the central supramolecular activation cluster (c-SMAC) the peripheral-SMAC (p-SMAC) and the distal (d-SMAC) which each contain a unique group of proteins. The c-SMAC contains the TCR binding to the antigen-MHC complex, surrounded by the p-SMAC containing the integrin LFA-1 which serves to stabilise the IS and finally the outermost region the d-SMAC which contains the phosphatase CD45 [181].

The cytoskeleton of DCs also plays an important role in the formation of the IS. Polarisation of F-actin is found in both DC and T cells at the contact zone [182-184]. Furthermore, nonmuscle myosin II is the actin-binding motor protein that is thought to be responsible for the many movements that occur in cells [185-187]. It is also identified to stimulate a flow of actin towards the synapse and interference with any of these proteins functions prevents the formation of the IS [185, 187, 188]. Recently it has been shown that when DC are exposed to the extracellular matrix proteins fibronectin (FIB) or laminin (LMN), prior to co-culturing with T cells, the T cell response is enhanced significantly [189, 190]. This enhanced T cell activation could be partly due to formation of more efficient and stable DC-T cell conjugates[189].

Understanding the molecular interaction which control the formation of IS could lead to new types of vaccines and therapies, and a better understanding of transplant rejection and allergic responses [191-195]. Currently, many different methods are used to study the IS, such as ELISA and flow cytometry. These techniques provide chemical information on the proteins involved but they often require cell fixation and membrane permeabilisation to allow specific labels (e.g. phalloidin) to be detected. Microscopy techniques are also utilized when studying the IS such as confocal fluorescence microscopy and scanning electron microscopy, but they have similar limitations due to the invasive procedures required. Conventional label-free imaging techniques (e.g., wide field, phase-contrast, dark field) can provide morphological information about cells, but they lack the chemical specificity needed for understanding molecular processes.

Therefore, the potential of Raman micro-spectroscopy imaging to provide quantitative information about the biochemical composition of the immunological synapses will be explored in this chapter. The technique is a non-invasive method for chemical and structural information of the sample and it is well suited for studying live cells. Water solutions (buffers and culture media) do not interfere with Raman experiments and there is no need for cell labelling or other cell modifications [46, 47, 68]. Raman micro-spectroscopy allows probing of the sub-cellular compartments and provides a unique spectral fingerprint of the molecular composition within cells. Different cell types in different morphological states will vary in their overall molecular composition and this is reflected

in the Raman spectra, as the intensity of the Raman bands depend upon the concentration of the biomolecules [58, 60]. Raman chemical imaging of cells has been reported previously including fixed [84-87, 89] and live cells [196, 197]. Furthermore, Raman studies of activated versus non-activated T cells [195, 198] and other white blood cells [199, 200] were conducted.

5.2 Experimental

Ethics Statement

Monocyte derived dendritic cells were derived from the peripheral blood of healthy volunteers which was obtained with prior written consent and The University of Nottingham Medical School Research Ethics Committee approval.

Generation of dendritic cells and T cells

Peripheral blood monocytes (PBMCs) were isolated from the heparinized blood of healthy volunteers by standard density gradient centrifugation on Histopaque (Sigma, Irvine, UK). DC and T cells were prepared as described before [201]. Briefly, monocytes were isolated from PBMCs using CD14 microbeads (Miltenyi Biotec, Bergisch Gladbach, Germany) and cultured in RPMI medium (Sigma) supplemented with L-glutamine, antibiotics and 10% fetal calf serum (FCS) containing 50 ng/ml of GM-CSF and 250 U/ml of IL-4 (R&D Systems, Oxford, UK) in 24-well plates for 6 days. T cells were isolated from the PBMC fraction using the Pan T cell isolation kit (Miltenyi Biotec, BergischGladbach, Germany) according to manufacturers' instructions.

Culture of immature DC with extracellular matrix proteins

Tissue culture plates were coated for 1.5 hours at 37 °C with 10 μg/ml laminin (Sigma, Irvine, UK) or 1% BSA prepared in PBS as previously described [189]. After incubation the protein solutions were aspirated followed by two washes with PBS. Immature DC were washed once, re-suspended in serum-free AIM V medium (Invitrogen, UK) and transferred to the coated wells for 48 hours at 37 °C.

DC-T cell conjugate formation

Laminin or BSA treated DC were harvested and centrifuged with autologous T cells in 1:3 ratio (DC : T cell) at 50xg for 5 minutes at 4 °C in a conical tube. After centrifugation cells were incubated at 37°C in a water bath for 30 minutes and gently suspended over titanium holders containing MgF_2 coverslips which had been coated with a 0.1% poly-l-lysine solution (Sigma, Irvine, UK) to improve adherence of cells to the surface.

Raman spectroscopy

Raman spectra were recorded using a home-built Confocal Raman micro-spectrometer optimized for live-cell studies as described previously (Chapter 3). The use of 785 nm laser for cell irradiation and an environmental enclosured integrated to the microscope ensured suitable physiological conditions for Raman spectral measurements of living cells over periods of several hours. Raman spectral imaging was performed by automated scanning of the cells through the laser focus in a raster pattern (0.5 μm step size) and acquiring Raman spectrum at each position (usually 1.5 s/pixel). The spectrometer wavenumber axis was calibrated prior to each experiment using tylenol (10 points) sample indicating an accuracy of 0.5 cm^{-1}.

Fluorescence imaging

Immuno-fluorescence imaging of cells was performed on the same cells after completion of the Raman spectral imaging experiment. Wide-field fluorescence imaging was integrated on the confocal Raman micro-spectrometer to allow molecular specific imaging using several fluorescent labels. The retrospective positioning and identification of the cells was based on two thin marks engraved on the cell chambers (retro-positioning accuracy was 5 μm).

Phototoxicity test: to check if the exposure of cells to 785nm laser induced apoptosis, after Raman imaging cells were stained using the Live/Dead cytotoxity kit (Molecular Probes, Paisley, UK) according to manufacturer's instruction. Briefly, the kit is comprised of two dyes: calcein, which is retained by living cells producing an intense green fluorescence and ethidium homodimer, which enters cells with damaged membranes and produces bright red fluorescence. Live cells without

exposure to the laser and cells treated with 4% formaldehyde (fixed and dead) were used as controls.

Immuno-fluorescence imaging of cell nuclei and actin: After Raman imaging of cell junctions the cells were fixed with 4% formaldehyde for 10 minutes then stained with two dyes to identify the actin filaments and the cell nuclei. After fixation, the cell membrane was permeabilised with Triton-X and then washed with PBS and stained for 30 minutes with Phalloidin-488 (diluted 1/100 with PBS, Sigma-Aldrich), washed again and stained with of 4',6-diamidino-2-phenylindole (DAPI, Sigma-Aldrich; 100ng/ml) for 5min. Confocal microscopy images of actin were acquired using a Zeiss laser-scanning microscope LSM 510, equipped with a Zeiss Axiovert 100 M microscope using the same staining and preparation procedures.

Data analysis

Pre-processing and data analysis was performed using in-house software in Matlab as described previously (Chapter 4). For imaging, an area under a selected Raman band was obtained by calculating the integrated intensity value of the band after subtraction of an estimated linear baseline and representing at each measurement position in the cell. Additionally, cluster fuzzy c-means (FCM) analysis method, which is a well established technique for producing spectral images of biological samples, was performed to group similar data. In addition, this technique also assigns every spectrum a membership grade for each cluster, providing a scaled image based on membership grade.

5.3 Results and discussion

5.3.1 Polarisation of actin in immunological synapse - confocal microscopy

Actin is the major component of the cytoskeleton of eukaryotic cells and is present mainly as fibrous polymer F-actin. There are many types of this protein but nonmuscle β- and γ-actins, also known as cytoplasmic actin, are predominantly present in non-muscle cells, while α-actins are found in muscle and are the most important components of the contractile machinery. Several studies show that actin polarisation plays major role in the process of immunological synapse

formation [182, 183, 189, 202]. The actin accumulation on the edges of DC is enhanced when they were exposed to extracellular matrix proteins (like fibronectin, laminin or collagen) prior to interaction with T cells. Indeed, recent work has shown that FIB or LMN treated DC exhibit stronger interaction with T cells [189]. To establish the impact of laminin treatment on the DC-T cell junction, confocal microscope images of control (un-treated) and laminin treated DC co-cultured with T cells, were taken after staining with the actin specific dye phalloidin (Figure 5-1). The intensity images revealed that treatment of DC with 10 μg/ml laminin led to an increase in polarization of actin filaments and formation of a more efficient IS at the junction between DC and T cells. However, these images also show that apart from requiring cell fixation, confocal fluorescence microscopy images are difficult for quantitative analysis of actin accumulation.

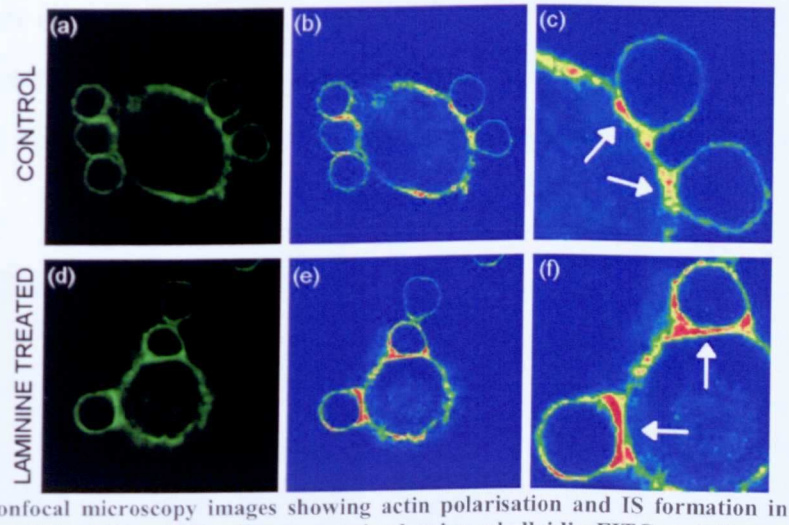

Figure 5-1. Confocal microscopy images showing actin polarisation and IS formation in control and laminin treated DC. DC and T cells were stained using phalloidin-FITC and figures (a) and (d) correspond to the true colour of control and laminin treated DC. Figures (b) and (e) show the staining intensity where blue to red is equivalent to low to high intensity. Figures (c) and (f) show the IS at a higher magnification. Results here show a more intense staining and thus accumulation of actin filaments in laminin treated DC. Arrows point to actin polarisation/IS formation.

5.3.2 Raman spectra of individual live dendritic cells

The aim of this study was to investigate the ability of Raman micro-spectroscopy imaging to monitor and assign biochemical changes in dendritic cells after treatment with laminin and then co-culture with T cells. However, biomolecules inside cells and culture media are sensitive to light and this makes the choice of laser wavelength crucial for studying living cells. Since the DC and T cells analysed in this study are potentially susceptible to laser damage, we have carried out viability tests

1 hour after laser irradiation. These tests confirm that the cells were healthy living cells as they only fluoresce with calcein dye and not ethidium homodimer dye, which confirms that the 785 nm 170 mW laser used for Raman spectral imaging did not affect cell viability. It is important to note that in CRMS imaging, cells are scanned through the laser focus; therefore irradiation is only 1-1.5 seconds at each position in the cell accounting the total irradiation time to be for example for T-cells (usually small in comparison to DCs) ~10 minutes.

Raman micro-spectroscopy imaging allows understanding of the biochemistry and morphology of specimens under investigation. Figure 5-2 shows typical brightfield, immuno-staining (actin and nucleus) and Raman spectral images of individual live DC and T cells obtained with two different techniques – peak intensity distribution and FCM clustering analysis. Additionally, typical spectra obtained from selected positions in cells at which fluorescence staining indicated high concentration of actin and DNA (marked with square and triangle respectively) are shown together with the Raman spectra of the FCM clusters corresponding to the same locations.

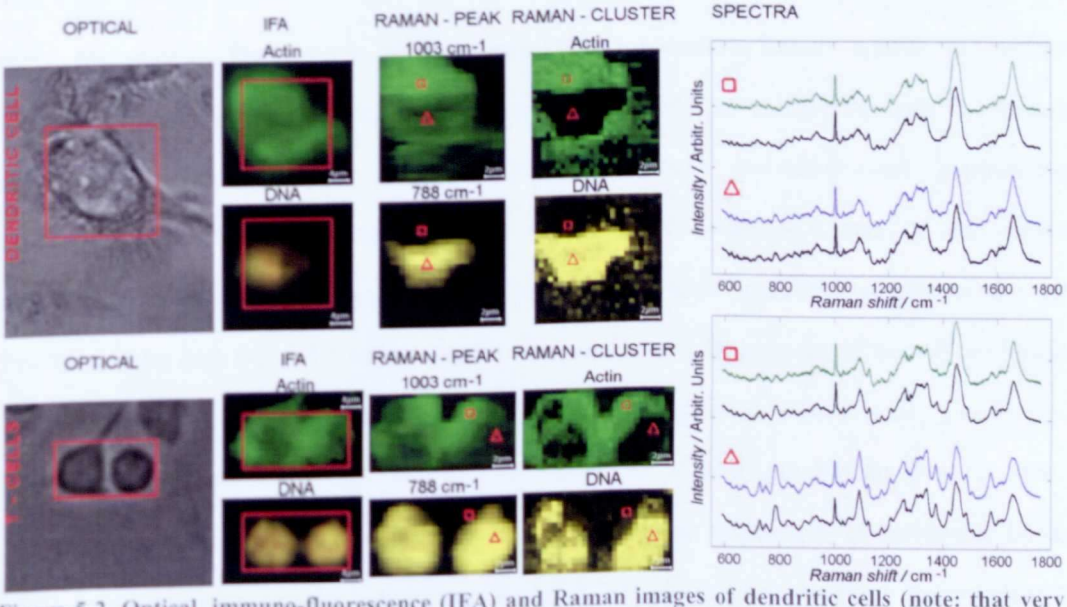

Figure 5-2. Optical, immuno-fluorescence (IFA) and Raman images of dendritic cells (note: that very thin dendrites are also visible on Raman image) and T-cells. Typical Raman spectra of control dendritic cell (top) and T-cell (bottom) taken from cytoplasm (marked with square) and nucleus (marked with triangle) along with corresponding cluster spectra is also shown.

The Raman spectra in Figure 5-2 demonstrate the high chemical heterogeneity of cells. Raman bands associated to proteins, nucleic acids, lipids and carbohydrates can be identified, and tentative assignment of these bands has already been reported and could be find in appendix 1. The large number of C-H bonds in proteins leads to a strong Raman band around 1450 cm^{-1},while certain amino acids produce strong Raman bands, such as phenylalanine (1003 cm^{-1}), tyrosine (854 cm^{-1}) and tryptophan (760 cm^{-1}). Additionally, 915-985 cm^{-1} C-C stretching and the protein amide Raman bands (Amide I - 1660-1670 cm^{-1}, Amide III - 1200-1300 cm^{-1}) could determine secondary structures of proteins. Nucleic acids are characterised by the vibrations of the sugar-phosphate backbone O-P-O of DNA (788 cm^{-1}). The vibration of the phosphodioxy group produces a relatively strong Raman band at 1095 cm^{-1}, which is rather insensitive to conformational changes of the nucleic acids. Additionally, Raman peaks corresponding to nucleotides can also be identified at 782 cm^{-1} (thymine, cytosine and uracil) 1373 cm^{-1} (thymine, guanine and adenine) and 1578 cm^{-1} (guanine and adenine).

The FCM images were obtained from full spectral datasets of dendritic cells and T-cell, using four clusters. The spectra of the clusters which resembled Raman spectra of nucleic acids and proteins are also showed in Figure 5-2 (in black) for comparison with the Raman spectra of cytoplasm and nucleus. Figure 5-2 shows that both univariate and multivariate imaging approaches provide images similar to the immuno-staining images of cell nuclei and actin. Raman spectral images using the 788 cm^{-1} band shows excellent correlation with the DAPI image for both DC and T cells. It is also worth noting that the intensity of the 788 cm^{-1} band is more intense in T cells compared to DC, confirming the higher level of DNA packing in T cells. Nevertheless, the univariate approach has its limitations as only one Raman band is used. Therefore, the univariate images of actin represent the intensity mapping of phenylalanine band, which is found in most proteins. However, the FCM images consist of the entire Raman spectra and reflect the main similarities between Raman spectra in cells obtained in an unsupervised automatic way. Therefore, the FCM imaging method was preferred over the univariate method.

5.3.3 Imaging of IS with CRMS

The Raman spectral images of junctions between live control DCs and T-cells are shown in Figure 5-3 alongside fluorescence staining for actin and cell nuclei carried out at the end of Raman spectral measurements and after cell fixation and staining. The spectral images of actin and DNA parallel the fluorescence staining.

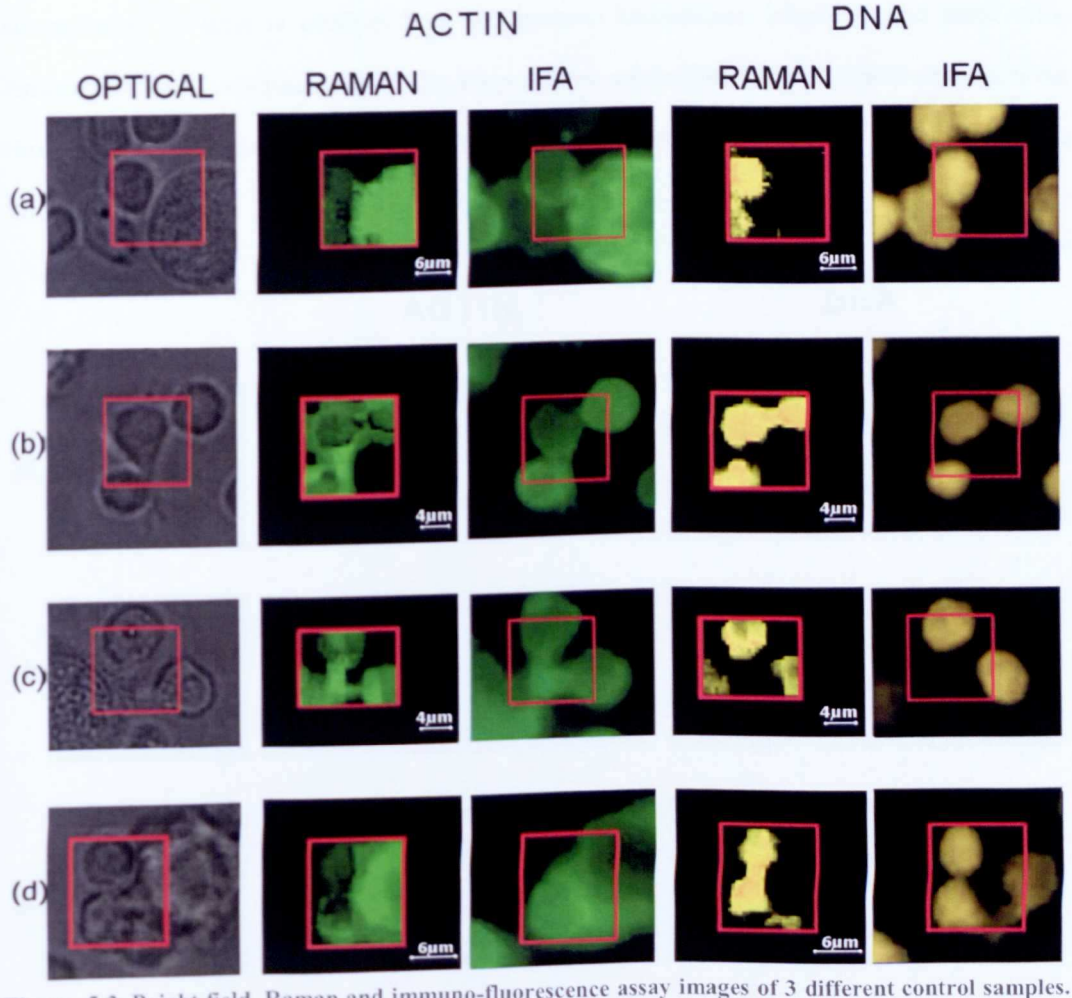

Figure 5-3. Bright field, Raman and immuno-fluorescence assay images of 3 different control samples. Raman images of actin and DNA distribution were obtained by FCM clustering method and fluorescence staining was performed with Phalloidin and DAPI respectively.

The Raman images corresponding to the actin cluster in FCM method revealed the actin distribution in the IS junctions for DC and T cells in exquisite detail. The Raman spectral images of proteins indicated a more homogeneous distribution of actin in the cytoplasm of dendritic cells. In contrast, the Raman spectral images corresponding to proteins of IS formed after pre-

treatment of DC with laminin (Figure 5-4) show an increase in proteins compared to control cells. The accumulation of actin is confirmed by the immuno-fluorescence images of the same cells.

In contrast, the Raman spectral images corresponding to proteins of IS formed after pre-treatment of DC with laminin (Figure 5-4) show an increase in proteins compared to control cells. The accumulation of actin is confirmed by the immune-fluorescence images of the same cells. Furthermore, these conclusions were also supported by confocal imaging of similar cell junctions. However, the main advantage of CRMS is that imaging can be performed on live cells without requiring cell fixation.

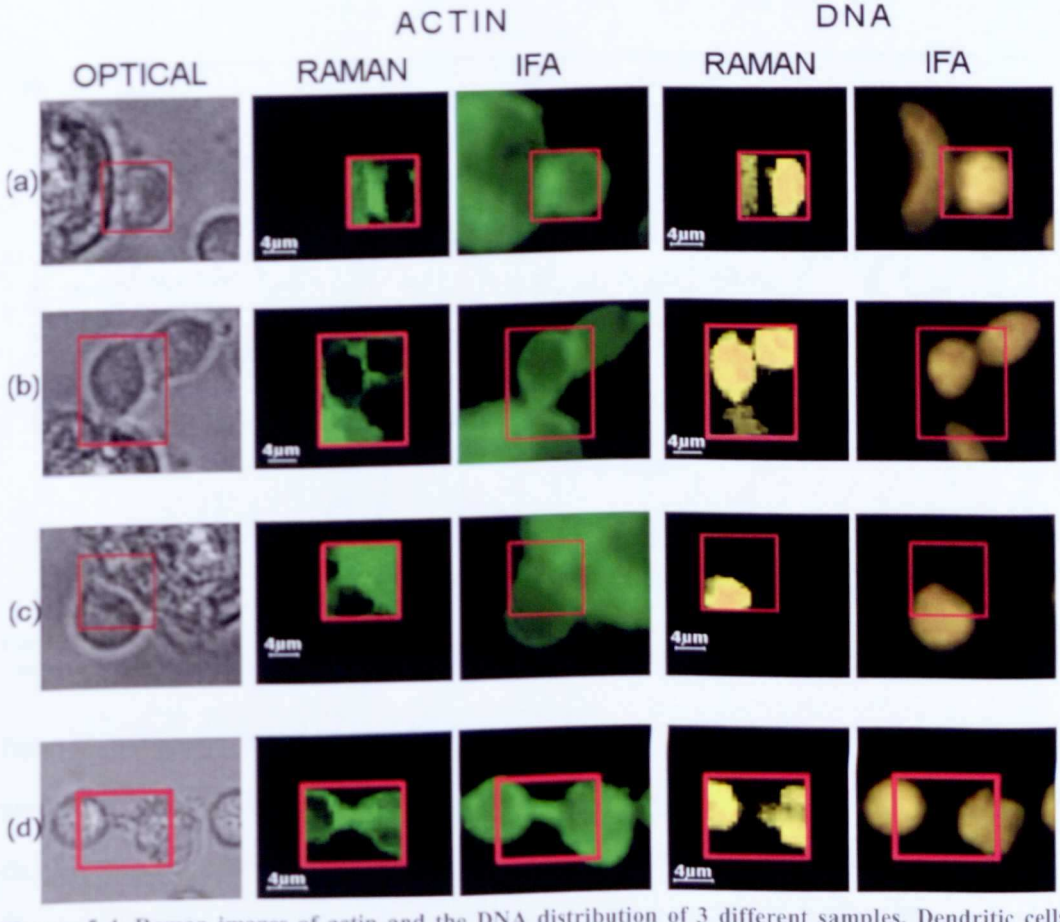

Figure 5-4. Raman images of actin and the DNA distribution of 3 different samples. Dendritic cells were exposed to laminin before co-culturing with T cells and forming immunological synapses. The Raman images are shown together with bright field optical and fluorescence staining images of actin (Phalloidin) and DNA (DAPI) of the same cells for comparison.

The Raman spectra of FCM clusters for control and LMN treated cells are shown in Figure 5-5A. Moreover, the Raman spectra of purified chemical have also been measured with the aim of identifying Raman bands specific to these molecules (Figure 5-5B). These were proteins involved in formation of IS [182, 183, 185]: actin (bovine muscle) and myosin (heavy chain from rabbit muscle), DNA (bovine muscle) and glycogen (bovine liver) as an example of carbohydrates.

Many cellular movements depend on the interactions between actins filaments and myosin. However, many different proteins account for both groups of these proteins types, moreover, their functions are still not fully understood [186, 188, 203]. Measured actin is of an unknown polymerisation state. Myosins are composed of α-helical heavy chains and several light chains [188].

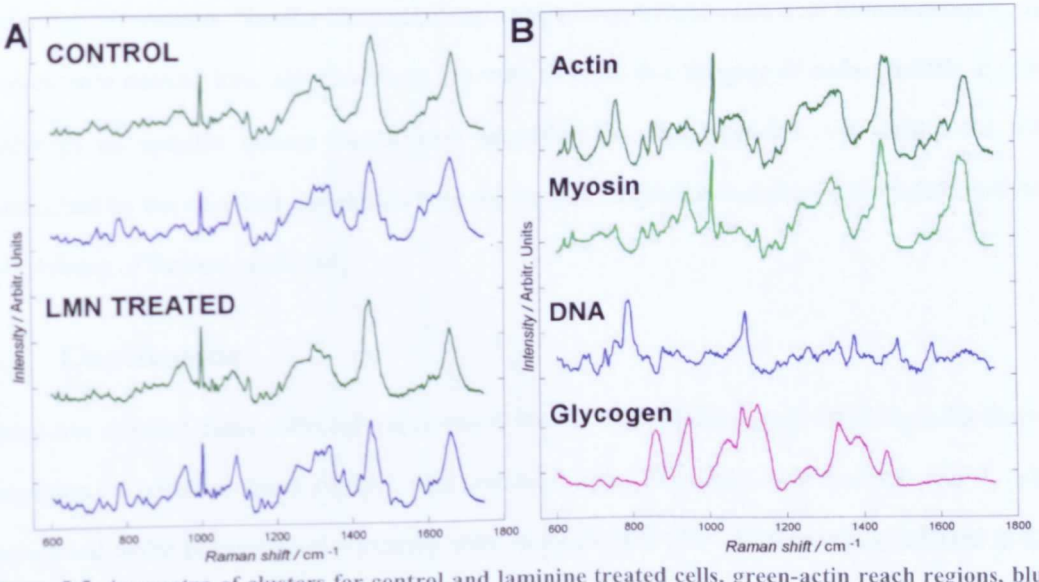

Figure 5-5. A: spectra of clusters for control and laminine treated cells, green-actin reach regions, blue – nucleus; B: spectra of pure chemicals: actin, myosin, DNA and glycogen.

Figure 5-5 B shows that Raman spectra of actin is similar to typical Raman spectra of other proteins and no specific Raman band can be identified. Nevertheless, comparison between the clusters spectra of control cells and cells treated with laminin shows an increase of proteins contributions in the spectra (for example 1003 cm^{-1} phenylalanine band). Additionally, increase of the 920-980 cm^{-1} band, indicates an increase of α-helical proteins. However, Raman spectra

corresponding to nucleus positions also indicated a significant bands from proteins, which could be assigned to histone proteins [68].

It is important to note that FCM Raman images in fact represent mapping of the membership grade for the spectral cluster which contains all main spectral features of proteins. No specific Raman bands were identified in the Raman spectra of actin or FCM. However, since an increase in actin polarization is expected in the area of IS and the FCM Raman images and immuno-staining images are in good correspondence, it is reasonable to suggest that the FCM images are indeed representation of actin accumulation. These conclusions were also supported by confocal imaging of similar cell junctions.

However, the main advantage of CRMS is that imaging can be performed on live cells without requiring cell fixation. Similar methods using comparisons between confocal Raman imaging and fluorescence staining have also have been reported for label-free imaging of mithochondria in cells. Although no specific Raman bands were identified for mithochondria, the assignment was established by the excellent correlation between Raman images produced by multivariate analysis and staining of the same cells [86].

5.4 Conclusions

Label-free spectral maps collected via confocal Raman micro-spectroscopy of living cells during formation of immunological synapse was presented here. Individual live dendritic and T cells maintained under physiological condition were analyzed and their viability was confirmed at the end of the Raman spectral imaging. Experimental conditions, particularly laser irradiation have been optimised to ensure that no damage was induced on cells.

Raman colour-coded spectral images corresponding to actin and DNA were in good agreement with fluorescence staining of nuclei of the same cells. Distinguishing between proteins which do not interact resonantly with the near infrared laser (needed to avoid cell damage) is very challenging since spectral differences between proteins are minute. Although no specific Raman bands have been identified in the Raman spectra of actin the results in combination with the

confocal fluorescence imaging indicate this is the most likely candidate. Furthermore, investigation of IS using CRMS indicated a higher accumulation/polarization of actin in the laminine pre-treated cells.

These results demonstrate that the main advantages of CRMS are the ability to obtain molecular images from live cells without staining and fixation. Therefore, further development of this technique for spectral imaging of the immunological events such as formation of IS in living cells represents a potential avenue for probing cellular processes such as cell-cell interaction, endocytosis, cell growth and drug–cell interactions.

PAGE NUMBERING AS ORIGINAL

Chapter 6.

Non-invasive time-course imaging of apoptotic cells [2]

"The beginning of knowledge is the discovery of something we do not understand"

Frank Herbert (1920 - 1986)

In this chapter the time course experiment on cells undergoing the drug induced cell death will be presented. Raman spectral images of the same cells were collected at two hours intervals over 6 hours duration. Immuno-fluorescence assays were carried after Raman measurements to confirm that cells were undergoing the apoptosis process. Raman spectral images for various biochemicals were built to establish cellular changes.

---

[2] This work was conducted in collaboration with Prof Poulam Patel group from Clinical Oncology City Hospital Nottingham, School of Molecular Medical Sciences, Faculty of Medicine & Health Sciences

6.1 Introduction

Confocal Raman micro-spectroscopy was used to measure time-course spectral images of live cells undergoing apoptosis without using molecular labels or other invasive procedures. Human breast cancer cells (MDA-MB-231 cell line) were exposed to 300μM etoposide to induce apoptosis and Raman spectral images were acquired from the same cells at two hours intervals over a period of 6 hours. The purpose-built inverted confocal Raman micro-spectrometer integrated an environmental enclosure and wide-field fluorescence imaging. These key instrumental elements allowed the cells to be maintained in culture media under sterile physiological conditions and enabled viability and apoptosis assays to be carried out on the cells at the end of CRMS measurements.

Apoptosis is one of the most important cellular processes, in which a cell commits suicide and breaks down its structure in a well organized manner to ensure minimum toxicity to the neighbouring cells [204]. Apoptosis, also known as programmed cell death (PCD), differs from necrosis (cell death due to cellular injury, infection or trauma), where the cellular debris can damage the organism. Although apoptosis occurs as a natural process in living organisms, alterations in molecular mechanisms associated with apoptosis in cells have been linked to many diseases, in particular cancer [205]. However, the development of molecular interactions in cells during apoptosis, particularly at early stages, is not fully understood. Apoptosis is a time-dependent biological process spanning over several hours, involving cytoskeleton modifications, condensation of the nucleus, formation of apoptotic bodies and cell breakdown. The observation of discrete and dynamic biochemical events in living cells during apoptosis is still a challenging task due to the lack of non-invasive molecular specific imaging techniques. Such techniques are required to follow the same group of cells undergoing apoptosis and record the time-resolved biochemical changes with high spatial resolution over time periods as long as several hours.

Most techniques available for imaging individual cells provide only single snap-shots because of the invasive procedures they require. Molecular specific techniques based on antibody conjugation (e.g., fluorescence imaging), require cell fixation as most molecules of interest in apoptosis are found inside the cell. Transgenic strategies to express markers, such as green fluorescent protein,

from specific promoters have been recently developed [27]. However, genetic manipulation of cells requires laborious protocols to be developed to ensure molecular specificity, which may interfere with normal behaviour of cells. In addition, fluorescence imaging is not a quantitative method because it relies on measurements of emission intensity, which suffers of high variability related to preparation protocols or photo-bleaching. Conventional imaging microscopy techniques (e.g., phase-contrast, dark field) can provide morphological information about cells over extended periods of time even with video-capture abilities. However, these techniques lack the chemical specificity needed for understanding molecular processes.

Label-free chemical imaging of cells could be obtained by vibrational spectroscopy techniques such as Fourier transform infrared spectroscopy (FTIR), which deals with absorption spectrum of the bond or group that vibrates and Raman micro-spectroscopy (RMS), based on inelastic scattering of light by vibrating molecules. FTIR was used previously for the visualization of the distribution of chemical components on cells that are dried [206]. Imaging of living cells by FTIR is difficult because of the strong absorption of water in the mid-infrared region and it is difficult to achieve high spatial resolution due to relatively large spot size of the IR light on the sample. However, attenuated total reflection FTIR (ATR-FTIR) spectroscopic imaging was recently reported for studying individual live human cancer cells in an aqueous environment. The high quality chemical imaging was achieved by minimizing the effective path length of the IR light in the sample [207].

Compared to infrared absorption spectroscopy, water has a low Raman scattering cross section thus it does not interfere with the measurements. Therefore cells can be maintained in culture media under sterile physiological conditions during measurements and spectral information could be obtained from live cells in a non-invasive way, without the need of labels or other contrast enhancing invasive methods [46, 68]. RMS has been used for studies of subcellular components such as nucleus [68], heme moieties in erythrocytes [208] and cytotoxic granules in human killer T cells [209]. Biochemical differences in cells *in vitro* cultures related to cell cycle and proliferation showed spectral differences related to nucleic acids, lipids and proteins [61, 66, 210-213].

Additionally, RMS have been used for discrimination between healthy and cancerous cells [159, 214-216] or between embryonic stem cells and derived-cardiomyocytes [215]. RMS has also been used to detect biochemical changes in cells related to interaction between cells and toxic chemicals and drugs [70, 71, 73], including apoptosis [92, 217, 218].

Confocal Raman micro-spectroscopy (CRMS) combines the high chemical specificity of RMS with the high-spatial resolution of confocal optical microscopes to produce "Raman spectral images" corresponding to specific molecules in cells. This techniques has been used for high-spatial resolution imaging of fixed cells, such as imaging of organelles [86], distribution of proteins [84], lipid vesicles [219] and deposits [125], as well as cells exposed to cytotoxic chemicals [85]. CRMS has also been used to map the distribution of biochemicals at various cell cycle stage, including mitosis[88]. Spectral imaging of fixed apoptotic cells was also reported, showing changes in nucleus size and DNA condensation in late stages of apoptosis [69, 85]. More recent studies have also reported Raman spectral imaging of live cells maintained in buffer saline. [196, 197, 220]. Additionally, coherent Anti-Stokes Raman scattering (CARS) spectroscopy, a technique which enhances Raman scattering from molecules to produce spectral images at selected frequencies has been shown to produce high spatial resolution images of lipids in fixed [221] and live cells [131].

However, the ability to perform time-course spectral imaging on the same group of live cells, a unique feature of CRMS, has been reported only for short time periods (20 minutes) and on cells not maintained under physiological conditions [97, 99]. The aim of this study was to measure non-invasively time-course molecular changes in cells during apoptosis. Apoptosis was induced by exposing breast cancer cells to etoposide, one of the most effective drugs used in chemotherapy for treatments of many malignant tumors, including breast cancer [222]. Etoposide induces DNA double-strand breaks in living cells by inhibiting the activity of topoisomerase II during DNA duplication. Apoptosis occurs as an effect of the irreversible DNA damage induced to the cells [223].

Groups of selected cells (control cells and cells exposed to etoposide) were monitored over 6 hours by CRMS and molecular specific images of DNA and lipids were measured at 2 hour interval.

These images allowed the detection of time-dependent spectral changes which were related to cell biochemistry alterations during apoptosis.

6.2 Materials and methods

Cell culture

The human breast cancer cells (MDA-MB-231 cell line) were purchased from European Collection of Animal Cell Culture (ECACC). For CRMS measurements, cells were grown in purpose built sterile chambers of titanium with a transparent bottom window (0.17 mm thick MgF_2 coverslip, Global Optics, Bournemouth, UK). The cell chambers were 10 mm in height and 25 mm in diameter to ensure a suitable volume of culture medium for cell growth. The chambers enabled observation of individual live cells by a water immersion objective on an inverted Raman microscope. The cells were grown in MEM culture medium supplemented with 10 % DMSO, 30 % fetal calf serum (Gibco, UK) and 1% L-glutamine at 37 °C 5 % CO_2. A solution of 300 μM etoposide (Sigma-Aldrich, UK) was prepared in the same culture medium and the treatment was carried out by replacing the growing culture medium with the etoposide solution.

Immuno-cytochemistry

Immuno-fluorescence imaging of cells was performed on the same cells after completion of the time-course Raman spectral imaging experiment. Wide-field fluorescence imaging was integrated on the confocal Raman micro-spectrometer to allow molecular specific imaging using several fluorescent labels. The retrospective positioning and identification of the cells was based on two thin marks engraved on the cell chambers (retro-positioning accuracy was 5 μm).

The MDA-MB-231 cells were stained with three different compounds: 6-carboxyfluorescein diacetate (6-CFDA), Annexin V-Cy3 and 4',6-diamidino-2-phenylindole (DAPI). The procedure involved washing cells twice in calcium buffer and then exposing for ~25 minutes to the solution of 6-CFDA and the Annexin V compound in the calcium buffer. Cells were fixed in 4% formaldehyde for 15 min and after washing with PBS the cells nuclei were stained with DAPI for 5 min. The 6-CFDA, which is the non-fluorescent complex, enters the cell and is hydrolyzed by the esterases

present in living cells to the fluorescent compound 6-carboxyfluorescein, indicating that the cells are viable. Annexin V binds in the presence of calcium to phosphatidylserine, a phospholipid which becomes translocated to the external surface of the cell membrane in early stages of apoptosis. The combination of these two stains allows the discrimination between early apoptotic cells (annexin V positive, 6-CFDA positive), necrotic cells (annexin V positive, 6-CFDA negative), and viable cells (annexin V negative, 6-CFDA positive).

All chemicals used for immunocytochemistry were purchased from Sigma-Aldrich.

Confocal Raman micro-spectrometer

As described previously in detail (chapter 3) an optimized confocal Raman micro-spectrometer for molecular imaging of individual live cells over extended time periods of time (several hours).

It is based on an inverted optical microscope with an environmental enclosure (37 °C and 5 % CO_2) and a 785 nm ~170 mW (before objective) laser coupled. Under these conditions, Raman spectral measurements of individual live cells maintained in their original culture media were possible over periods of tens of hours without disturbing the cells and avoiding bacterial contamination. The spectrometer wavenumber axis was calibrated using a tylenol sample to an accuracy of 0.5 cm^{-1}. Raman spectral imaging was performed by automated scanning of the cells through the laser focus in a raster pattern (1 μm step size) using a high-precision step-motor stage and acquiring Raman spectra at each position (1 s/pixel for MDA-MB-231 cells). The lateral resolution of the instrument was measured to be ~1 μm (spectral images of 1 μm polystyrene beads in contact).

Data analysis

Pre-processing and data analysis was performed using in-house software in Matlab. Firstly, peaks caused by cosmic rays were removed on the affected spectra. Due to a CCD artefact, the spectral region 1250-1295 cm^{-1} was removed. Spectra which had the 1449 cm^{-1} band intensity below a chosen threshold were removed from data sets and considered background signal. The mean of the background spectra was subtracted from each individual Raman spectrum and singular value decomposition and Savitsky-Golay algorithms were used for noise reduction [69, 99]. Afterwards,

all spectra were baseline corrected using a 5th order polynomial. A Raman spectral image corresponding to a selected Raman band was obtained by calculating the area under the band after subtraction of an estimated local linear baseline and representing the integrated intensity value at each measurement position in the cell. Additionally, the averaged spectra of cells were studied with PCA method to highlight the differences between spectra of cells.

6.3 Results

6.5.1 Typical spectrum of MDA-MB-231 cells

Figure 6-1 shows typical Raman spectra measured from MDA-MB-231 live cells at different positions inside the cells (1 second integration time), before and after pre-processing. Figure 6-1B demonstrates the effectiveness of the singular value decomposition and Savitsky-Golay methods which enabled reduction of noise without distorting the Raman bands, thus allowing accurate estimation of the local baseline when calculating the area of Raman bands.

The Raman spectra in Figure 6-1 agree with the Raman spectra of other cell types and demonstrate the high chemical heterogeneity of cells [46, 68, 69, 88, 219]. Detail assignment of the Raman bands could be found in appendix 1. Raman bands associated to nucleic acids include backbone vibrations (O-P-O at 788 cm^{-1} and PO_2^- at 1095 cm^{-1}) and vibrations specific to nucleotides (thymine, cytosine and uracil at 782 cm^{-1} and guanine and adenine at 1578 cm^{-1}). Raman bands corresponding to proteins are found in the ranges 1660-1670 cm^{-1} (Amide I), 1450 cm^{-1} (C-H bending), 1200-1300 cm^{-1} (Amide III), 1003 cm^{-1} (phenylalanine), 854 cm^{-1} (tyrosine) and 760 cm^{-1} (tryptophan). C-O-C vibrations of the glycosidic bonds and ring vibrations in carbohydrates produce specific Raman bands in the 800-1100 cm^{-1} range. All lipids are characterised by intense Raman bands at 1449 cm^{-1} (C-H bending vibrations), 1301 cm^{-1} (CH_2 twisting), 1000-1100 cm^{-1} spectral range (C-C stretching), while Raman bands characteristic of unsaturated lipids can be found at 1658 cm^{-1} (C=C stretching). Membrane phospholipids also exhibit Raman band in the 700-900 cm^{-1} spectral range assigned to different residues at the phosphate-ester headgroup [209].

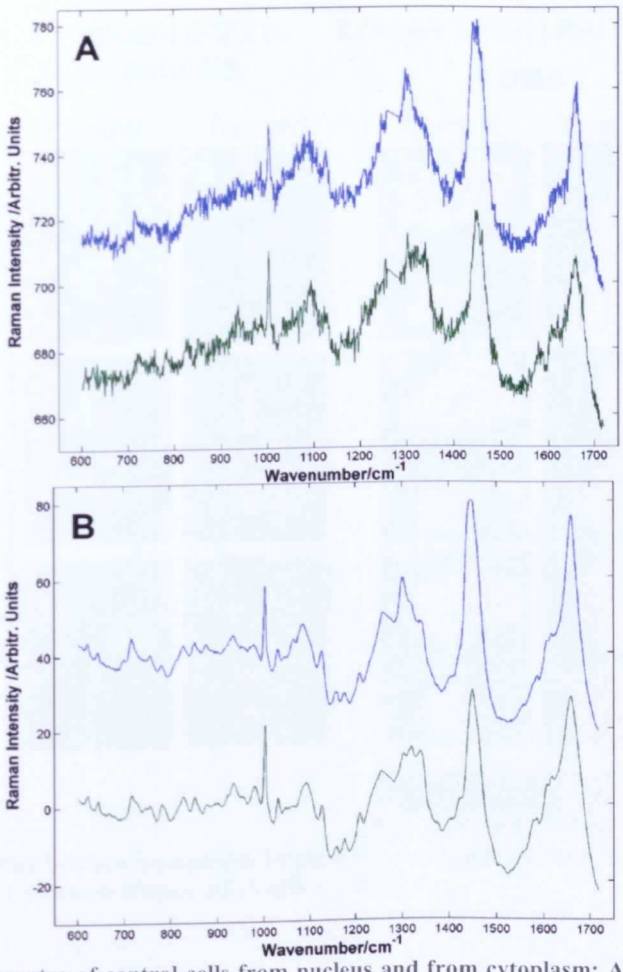

Figure 6-1. Raman spectra of control cells from nucleus and from cytoplasm: A: raw spectra, B: after pre-processing.

6.5.2 Time-course spectral imaging of apoptotic cells

Figure 6-2 compares typical time-course bright-field and Raman spectral images corresponding to DNA for two control (untreated) MDA-MB-231 cells and two MDA-MB-231 cells exposed to 300 μM etoposide. The time-course Raman spectral images of the DNA (ratio of 788 cm^{-1}/ 1003 cm^{-1} band) show a ~1.5 fold increase in the intensity of the Raman bands associated to DNA in all cells exposed to etoposide for 6 hours.

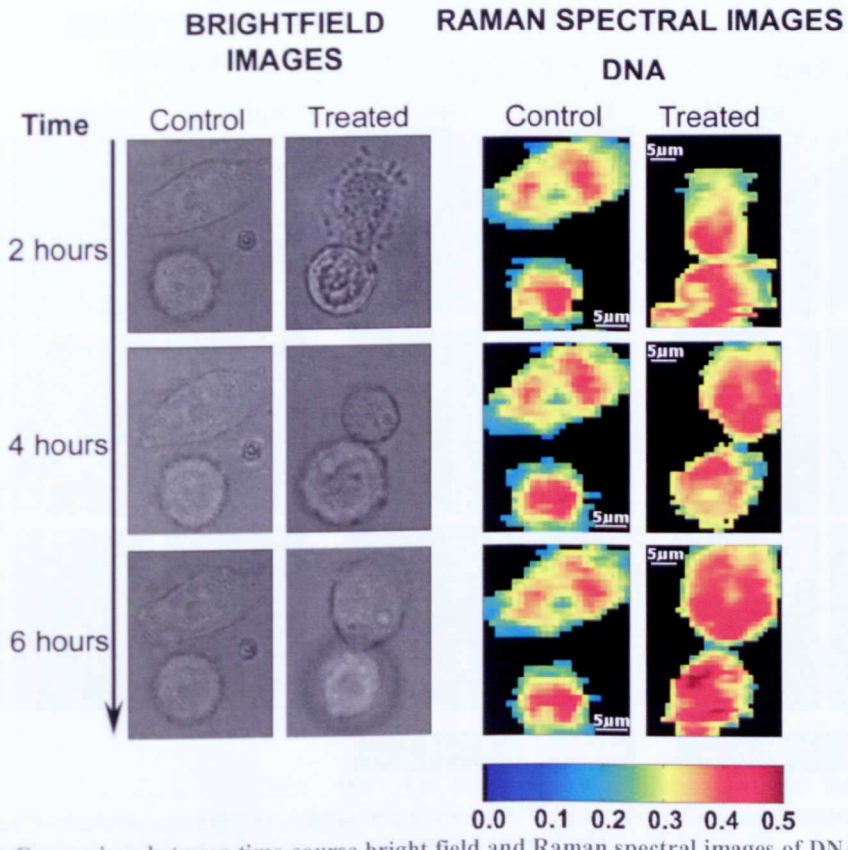

Figure 6-2. Comparison between time-course bright field and Raman spectral images of DNA (788 cm^{-1} band) for control and etoposide treated MDA-MB-231 cells.

However, the most dramatic cellular changes in the MDA-MB-231 cells treated with 300 µM etoposide are revealed by the time-course Raman spectral images of lipids (Figure 6-3). These images were produced by representing the ratio between the Raman signal corresponding to the lipids (1659 cm^{-1} and 719 cm^{-1}) and proteins (1003 cm^{-1}) bands at each position of the cells. The 1003 cm^{-1} Raman band has contribution only from proteins (phenylalanine symmetric ring stretching) and was not affected by etoposide treatment, therefore was used as a reference. The 1659cm^{-1} band has contributions both from proteins (Amide I band) and C=C stretching vibrations in unsaturated lipids while 719 cm^{-1} represents phospholipids.

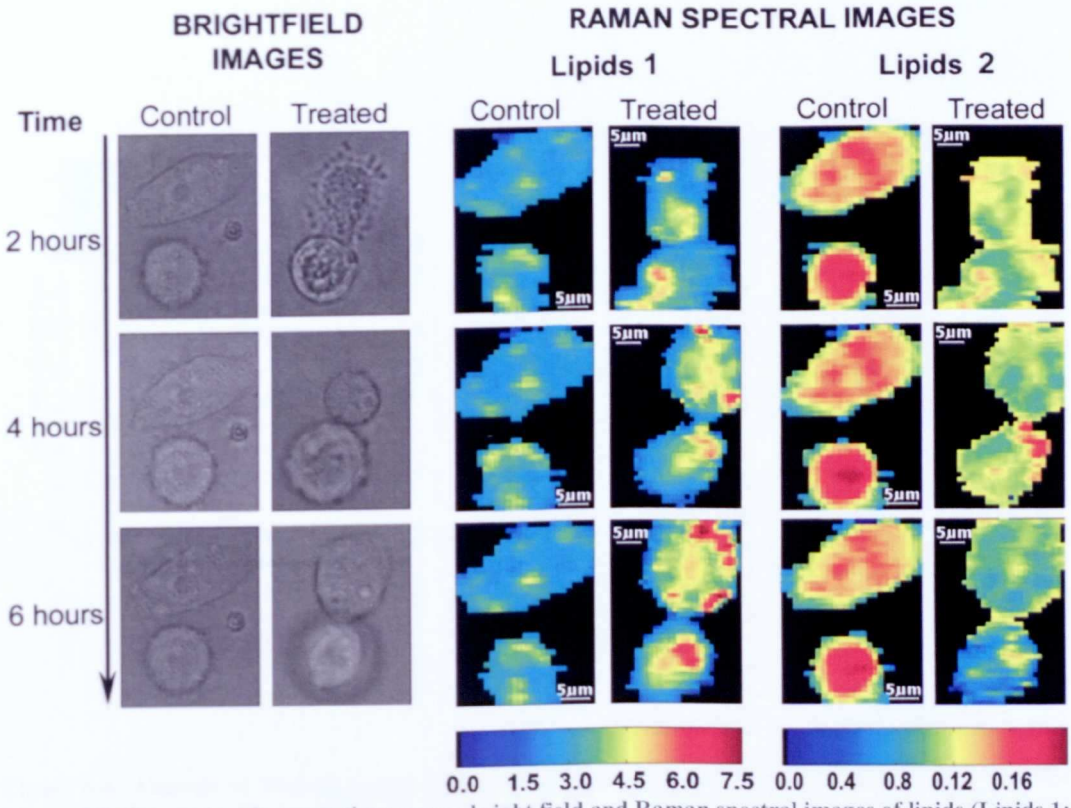

Figure 6-3. Comparison between time-course bright field and Raman spectral images of lipids (Lipids 1: 1659 cm^{-1} and Lipids 2: 719cm^{-1}) for control and etoposide treated MDA-MB-231 cells.

Figure 6-3 shows that regions rich in lipids were found in all healthy MDA-MB-231 cells. Analysis of Raman spectra corresponding to these regions indicate the presence of the 719 cm^{-1} Raman band corresponding to the choline group and a moderate level of saturation typical to cell membrane phospholipids [209]. Therefore, these results indicate that the lipid regions in healthy MDA-MB-231 cells are dominated by membrane phospholipids.

However, after etoposide treatment, Raman spectral images show a high build up of lipids in the cytoplasm of apoptotic cells, while no differences were observed in the control cells. The signal strength of the 1659 cm^{-1} band (C=C stretching) in MDA-MB-231 cells exposed to etoposide increased ~1.5 (±0.3) fold at 4 hours and ~2 (±0.3) fold at 6 hours after treatment. Analysis of the Raman spectra corresponding to the cytoplasmic lipid-rich regions in apoptotic cells provides information regarding the chemical composition of these regions.

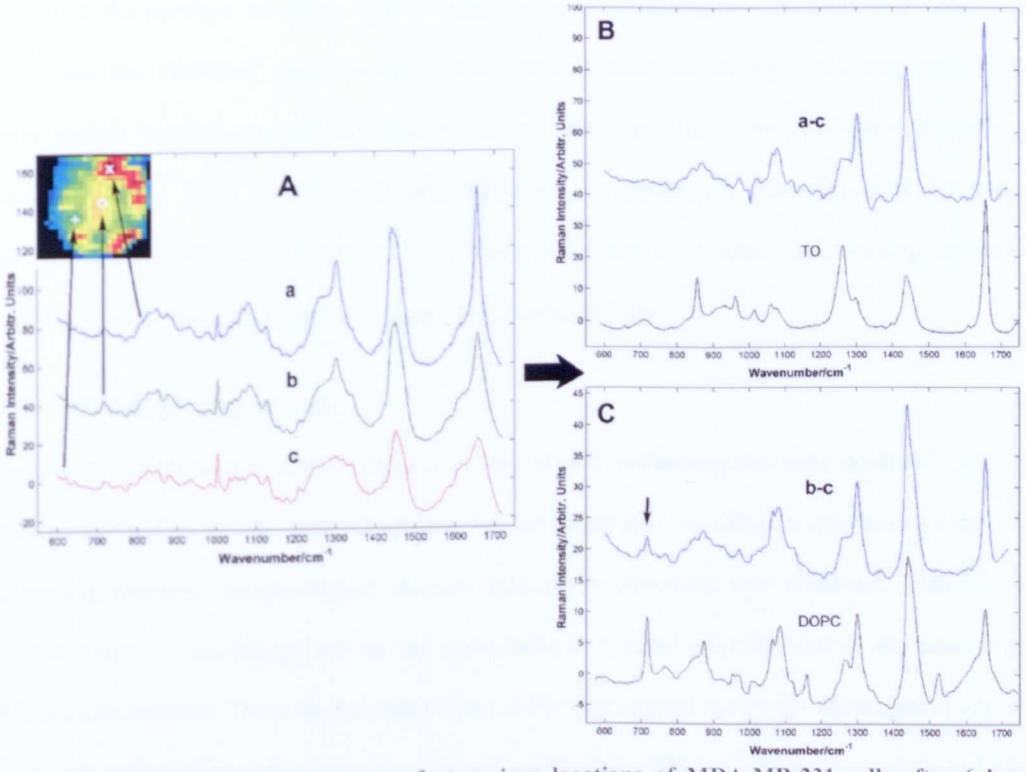

Figure 6-4. Analysis of Raman spectra of at various locations of MDA-MB-231 cells after 6 hours treatment with etoposide as indicated by arrows and white marks. A: Raman spectra taken from regions rich in unsaturated non-membrane lipids (a), membrane moderate lipids (b) and cytoplasm (c); B: The computed subtracted spectra a-c compared to Raman spectra of pure trilinolenin (TO); C: The computed subtracted spectra b-c and phosphatidyl choline (DOPC). Black arrow indicates the position of the 719 cm^{-1} Raman band corresponding to the choline group.

Figure 6-4 A shows Raman spectra at different positions inside the cells exposed to etoposide for 6 hours. Computed difference spectra when a Raman spectrum typical to the cytoplasm (spectrum c) was used for reference are shown in Figure 6-4 B and C. The computed difference spectra (a-c and b-c) corresponding to the lipid-rich regions show intense Raman bands specific to lipids at 1659 cm^{-1} (C=C stretching), 1441 cm^{-1} (CH_2 defromation), 1303 cm^{-1} (CH_2 twisting) and 1000-1100 cm^{-1} (C-C stretching). However, there are significant differences between the spectra at different locations. Certain lipid-rich regions (position b) contained phospholipids with a moderate level of unsaturation (the 1659 cm^{-1} band lower than the 1449 cm^{-1} band) and indicated the presence of the 719 cm^{-1} (symmetric stretching of $N_1(CH_3)_3$ of choline group) [209]. Comparison between difference Raman spectra and the Raman spectra measured of purified phosphatidyl choline (DOPC) indicates that these regions have a significant higher content of plasma membrane phospholipids than in healthy cells [209]. However, Raman spectra of other regions (e.g., position

a) showed the presence of lipids with a higher level of unsaturation (the C=C 1659 cm^{-1} band higher than the 1449 cm^{-1} band) but lacked any Raman band below 800 cm^{-1}, a spectral region where Raman bands associated to vibrations of phosphate and headgroups of phospholipids are found [209, 219, 224]. Figure 6-4B also compares the difference spectrum with the Raman spectrum of pure trilinolenin (TO) (3 C=C bonds), suggesting that these lipid-rich regions consist mostly of unsaturated non-membrane lipids (triglycerides) [209].

6.5.3 Viability/ apoptosis test

No morphological changes in the control cells was noticed, indicating that laser irradiation required for measurement of Raman spectral images did not affect cell viability. In contrast, for the cells undergoing apoptosis morphological changes specific to apoptosis was observed. Viability and apoptosis assays were carried out on the same cells at 2 hours after the end of the time-course CRSM measurements. These assays (see Figure 6-5) were carried out by the fluorescence staining of the cells and confirmed that control cells were viable and healthy (annexin V negative, 6-CFDA positive). The apoptosis and viability fluorescence assays carried out at the end of Raman spectral measurements on cells exposed to 300 μM etoposide confirmed that these cells were apoptotic: annexin V positive and 6-CFDA positive.

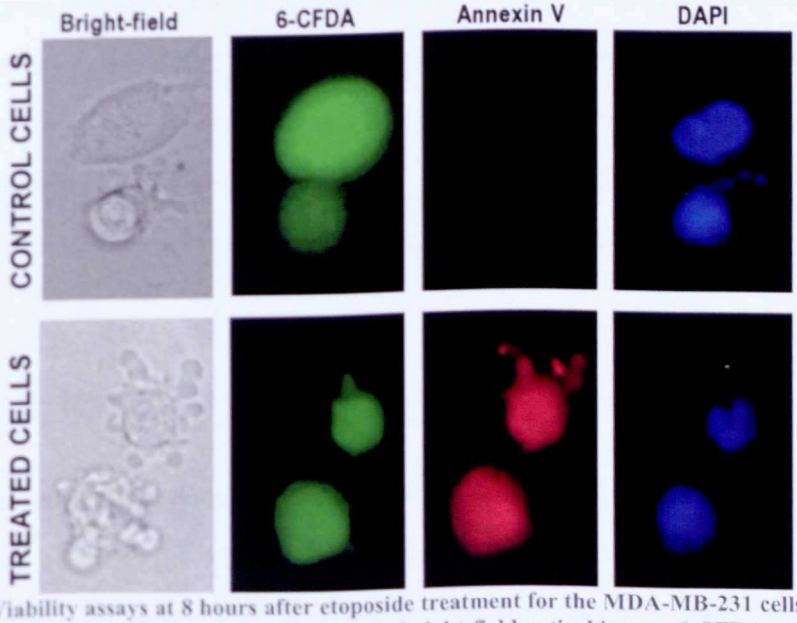

Figure 6-5. Viability assays at 8 hours after etoposide treatment for the MDA-MB-231 cells analysed by CRMS (2 hours after last Raman spectral imaging): bright-field optical image; 6-CFDA- viability assay; Annexin V- apoptosis assay; DAPI-nucleus staining.

6.5.4 Healthy and apoptotic cells grouping

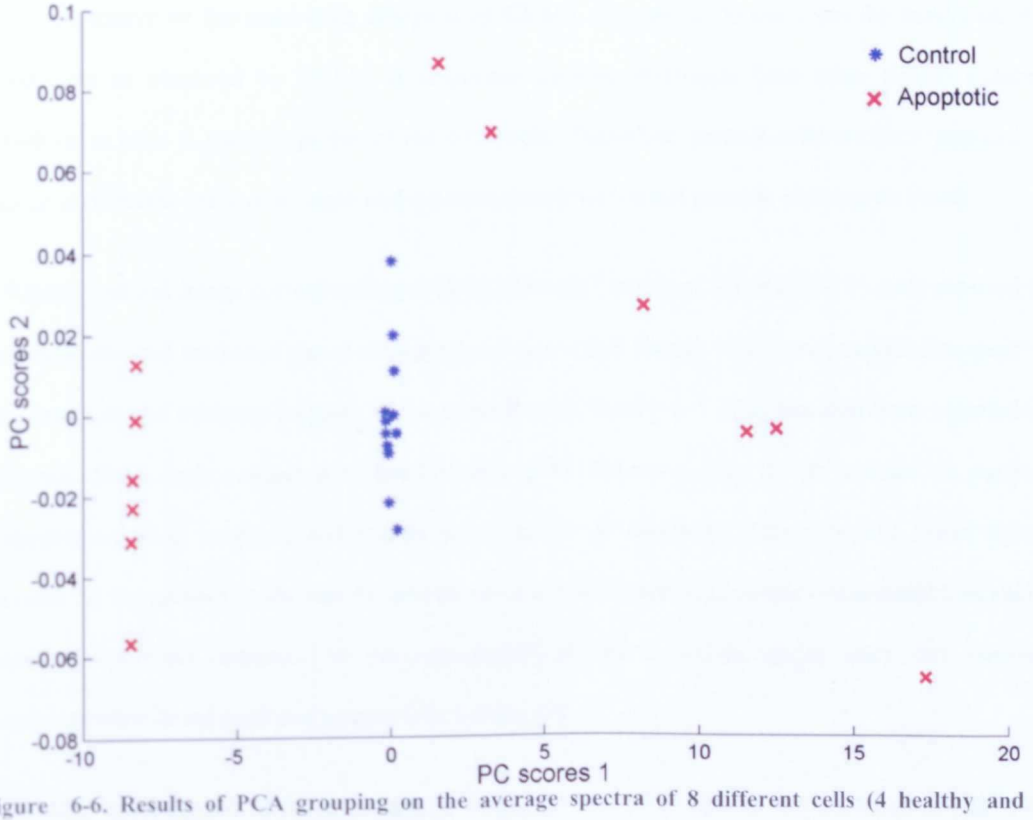

Figure 6-6. Results of PCA grouping on the average spectra of 8 different cells (4 healthy and 4 undergoing apoptosis).

Figure 6-6 shows the outcome of PCA analysis of averaged spectra of 8 different cells (4 healthy and 4 undergoing apoptosis) at 3 different time points (2,4,6 hours). The result indicates that non-treated healthy cells are clustered together (blue cluster) while treated cells are grouped separately. This result indicates that no overall changes happened in control cells over the time of studies, while the spectral changes are distinguishable in the averaged spectra of apoptotic cells. Unfortunately the distinction between different stages of apoptosis (different time-points) were not clearly apparent.

6.6 Discussion

6.7.1 Time-course spectral imaging of apoptotic cells

The integration of a CRMS (inverted microscope and near-infrared laser) with an environmental enclosure enabled the measurement of time-course spectral images of individual cells during

apoptosis. The wide-field fluorescence imaging system allowed retrospective cell viability and apoptosis assays on the same cells analysed by CRMS. The ability to carry out the assays on the same cells as observed by CRMS is important because etoposide (and other drugs) induces apoptosis in cells at specific points of the cell cycle. Therefore, various cells within a population will be at different cell cycle stages and a generic assay would not provide an accurate result.

A Raman spectral image corresponding to DNA (788 cm^{-1} band) of MDA-MB-231 cells exposed to etoposide showed increased signal strength (~1.5 times at 6 hours), which was assigned to nuclear condensation. An intensity increase of the same Raman band (~4-5 fold) has also been reported in apoptotic HeLa cells compared to healthy cells [69]. However, this report focused on nuclear fragments of fixed apoptotic HeLa cells at late stages of apoptosis. Therefore, the lower signal increase in the current study can be attributed to a lower level of nuclear condensation in early stages of apoptosis compared to previous studies at late apoptosis stages when cell nucleus fragments were found enclosed in apoptotic bodies [69].

In healthy cells, Raman spectral images of lipids show regions rich in membrane phospholipids (moderate level of unsaturation and intense band assigned the $N_1(CH_3)_3$ choline group at 719 cm^{-1} [209]) mainly in the vicinity of the cell nuclei. Cytoplasmic regions rich in lipids with similar Raman spectra have already been reported by RMS, both in healthy and apoptotic cells [69, 212, 219, 224, 225]. These regions were related to lipid vesicles, mithochondria or endosomal system [86, 219, 224]. Lipid rich regions characterised by strong 719 cm^{-1} band was also found in undifferentiated alveolar epithelial cells, and were assigned to alveolar vesicles storing surfactant proteins [212]. However, considering the location of the membrane lipid regions in healthy MDA-MB-231 cells in the vicinity of the cell nuclei, it is likely that these regions correspond to endoplasmic reticulum and Golgi apparatus, cellular structures rich in plasma membranes [85].

The time-course Raman spectral images of etoposide treated MDA-MB-231 cells show a high accumulation of both membrane and non-membrane lipids (triglycerides) in the apoptotic MDA-MB-231 cells (no changes were observed in the control cells). It is interesting to note that the

locations of these lipid-rich regions were not the same as positions associated to endoplasmic reticulum and Golgi apparatus prior to etoposide treatment.

Formation of large numbers of lipid vesicles in apoptotic cells (including apoptosis induced by etoposide treatment) has been already reported but only by invasive techniques [10]. Moreover, the transmission electron microscopy utilised in these studies could not provide information regarding the chemical composition of these vesicles and was carried out on fixed cells. However, this study showed that the appearance of the vesicles was at an early stage of apoptosis, prior to visible condensation of cell nuclei. Therefore, this result is in agreement with the lower level of DNA condensation measured in our study compared to values found in nuclear fragments in apoptotic bodies [69].

While accumulation of membrane phospholipids can be associated to a process preceding formation of apoptotic bodies [10], accumulation of non-membrane lipids were also found. Accumulation of highly unsaturated lipids in cells has been reported by RMS only in few cases but not in apoptosis. Growth of cells in culture medium containing an excess of unsaturated lipids led to formation of lipid bodies [87]. Lipid reserves in mouse oocytes have been associated to the required availability of lipids for membrane formation during rapid cell division [225]. Earlier studies by RMS demonstrated that the cytotoxic granules in human killer T lymphocytes consisted of highly-unsaturated non-membrane lipids [209].

Accumulation of non-membrane lipids in apoptotic cells has been detected by ^{1}H nuclear magnetic resonance (^{1}H NMR) [226], including in cells induced to apoptosis by exposure to etoposide[227]. However, these studies were not at single cell level due to the limited spatial resolution of ^{1}H NMR. The increase in the ^{1}H NMR signal was attributed to mobile fatty acyl chains of triacylglycerades, rather then cholesteryl esters. The ^{1}H NMR experiments showed that accumulation of intracellular lipids is an early event in apoptosis as cells exposed to lower concentrations of etoposide (15 μM) produced high detectable ^{1}H NMR signals as early as 4-7 hours (51).

While lipid bodies consisting of triacylglycerols are found in healthy cells, stress can induce the formation of lipid bodies, for example in cells, exposed to acidic pH [228, 229], cells engaged in inflammation [230] or apoptotic cells [230, 231]. A potential explanation for the high accumulation of non-membrane lipids in apoptosis may be the disturbance in lipid trafficking, or inhibition of phosphatidylcholine biosynthesis and the activation of phospholipases [230, 232, 233]. However, further studies are required to elucidate these hypotheses.

6.7.2 Spectral imaging of live cells: effect of laser wavelength on cell viability, spatial resolution and imaging time

Lasers in the visible range are typically more advantageous for Raman measurements because the efficiency of Raman scattering by molecules is approximately proportional to the fourth power of excitation wavenumber. In addition, CCD detectors used for Raman spectroscopy have higher sensitivity in the visible range. Therefore, visible lasers allow shorter imaging times, with typical acquisition times per pixel of 100-500 ms [69, 88, 152], compared to 785 nm lasers: 1 s in this study or 10-20 s in other studies [85, 95]. In addition, the superior beam quality of single transversal mode solid-state (532 nm) and gas lasers (488 nm, 514 nm, 647 nm) have been shown to produce diffraction limited Raman spectral images of fixed or immobile cells (live cells in buffer saline at room temperature) [69, 88, 152]. However, in the case of live cells maintained under physiological conditions, cell motility was the limiting factor for spatial resolution rather than the lower beam quality of the 785 nm laser diode.

Despite producing stronger Raman signals, visible lasers have severe limitations when used in hours-long time-course experiments as cells must be maintained in culture media. In these conditions, visible lasers excited strong fluorescence emission by cells and culture media, which swamped the Raman bands. Measurement of Raman spectra on live cells in culture media with 488 nm, 514 nm and 532 nm lasers were also attempted but unsuccessful. However, recent studies on fixed and live cells in buffer solutions using visible lasers [69, 88, 99, 152] suggest that the fluorescence background may be more often caused by cell culture media rather than cellular

components. Therefore, the possibility that certain culture media may not produce fluorescence emission when excited by visible lasers cannot be excluded.

Besides not exciting fluorescence background from cells and culture media, near-infrared lasers (700-850 nm) are also known to induce less photo-toxicity to cells compared to visible lasers [56, 68]. Our results show that the 785 nm laser had no effect on cell viability, in agreement with previous studies comparing cell damage induced by lasers in the 700-1000 nm range [148, 149]. The only time-course CRMS experiments reported so far (duration 20 minutes) used a 532 nm laser to produce spectral images of HeLa cells with 3 minutes temporal resolution [97, 99]. However, this study did not comprise any viability checks of cells.

6.8 Conclusions

The first time-course experiment over several hours in which label-free molecular images of the same group of cells were measured by CRMS was reported. While not limited to a specific application, this experiment focused on detection of time-dependent molecular changes in cells during apoptosis. Time-course spectral images corresponding to Raman bands assigned to DNA indicated an increase in signal intensity (~1.5 fold at 6 hours) in apoptotic cells, which was attributed to nuclear condensation. However, the level of DNA condensation was lower compared to previous studies of nuclear fragments found in apoptotic bodies of HeLa cells. The Raman spectral images of lipids indicated a high accumulation of lipids in apoptotic cells. This finding is in agreement with previous reports by other techniques, such as electron microscopy and ^{1}H NMR. However, CRMS allows detection and imaging of the lipid bodies in individual cells without requiring invasive procedures and enables detailed analysis of the molecular composition of the lipid bodies. The CRMS results indicate that the lipid bodies contain both membrane phospholipids and highly unsaturated non-membrane lipids, and the signal strength corresponding to these bodies increased ~2-fold at 6 hours compared to control cells. However, further studies are required to establish the origin of these biochemical changes. Furthermore, grouping the cells with PCA indicates that the average spectra from apoptotic cells differ from control MDA-MB-231 cells. This study proves the feasibility of CRMS for non-invasive label-free molecular imaging of cells in

extended period of times. Therefore, future developments of this technique could also be used for in vitro toxicological studies, cells sorting, testing of new pharmaceuticals, and monitoring the differentiation of cells.

Chapter 7.

Conclusions

"One never notices what has been done; one can only see what remains to be done"

Maria Skłodowska-Curie (1867-1934)

The main aim of the work described in this thesis has been the development of confocal Raman micro-spectrometer for chemical imaging of live cells. Concluding remarks on that work will be presented here.

7.1 Summary of work

The work presented in this thesis has been motivated in part by the increasing interest in label-free chemical imaging of individual live cells. In particular, the investigation focused on the spectral imaging of live cells in their physiological conditions over extended time periods. Raman micro-spectroscopy is a highly suitable technique for *in vitro* applications as it is non-destructive, does not require the use of labels or other contrast enhancing agents. Although only a few attempts have been reported on imaging living cells, the feasibility of Raman micro-spectroscopy for imaging and detection of biochemical changes related to various cellular processes has been demonstrated in few recent articles.

The main aim of this thesis has been the development of a dedicated confocal Raman micro-spectrometer for high resolution chemical imaging of living cells. The instrument overcome the main limitations of commercial systems and enabled two different detailed studies on live cells. The integration of the fluorescence imaging system made it possible to confirm the Raman findings and check viability of cells after laser irradiation.

Chapter 3 describes the details on the development of the Raman micro-spectrometer. . The key elements allowing studies of cells in physiological conditions (cell media, 37 °C, 5 % CO_2) without inducing damage were the choice of the 785 nm laser and incubation enclosure integrated on the inverted microscope. Dedicated software, which allowed spectral imaging measurements of cells and automates the Raman system, was developed and its details explained. Chapter 4 presents an evaluation of the instrument, in terms of spectral and spatial resolution, calibration and data analysis methods.

Chapter 5 reports a detailed study using Raman spectral imaging and fluorescence microscopy to investigate synapse junctions between functional lymphocytes and dendritic cells (DC) in laminin treated and non-treated DCs. These results indicate that actin is a main contributor to the Raman spectrum of the cytoplasm of dendritic and T cells. While for control cells the Raman spectral images of proteins indicated a more homogenus distribution of proteins in the cytoplasm of

dendritic cells, they indicated a higher accumulation of proteins at the immunological synapses when dendritic cells were pre-treated with laminin. Actin accumulation has been demonstrated in cells previously but requires invasive procedures: fixation, membrane permeability and labelling. While further studies are needed to establish the specificity of Raman spectra to actin, this study demonstrates the potential of CRMS for label-free non-invasive imaging of live cells junctions. This could have huge implications in cell biology as dynamic effects may be observed in live cells, without disturbing the cells.

Chapter 6 describes time-course label-free imaging on individual living cells. Cancerous MDA-MB-231 cells were treated with anticancer drugs to induce apoptosis and then cells were observed for several hours by Raman imaging. The time-course spectral images corresponding to DNA Raman bands indicated an increase in signal intensity in apoptotic cells, which was attributed to DNA condensation. The Raman spectral images of lipids indicated a high accumulation of membrane phospholipids and highly unsaturated non-membrane lipids in apoptotic cells. The lipids accumulation in the apoptotic cells in the early phase of the apoptosis process was correlated to production of lipid bodies. Similar lipids accumulation in the early phases of apoptosis was demonstrated by CMRI in different studies. This study demonstrates the potential of confocal Raman micro-spectroscopy for label-free time-course imaging of individual live cells which may become a useful tool for *in vitro* toxicological studies and testing of new pharmaceuticals, as well as other time-dependent cellular processes, such as cell differentiation, cell cycle and cell-cell interactions.

Raman spectral characterization of different cells from primary cells (dendritic and T cells) and established immortalised cell-line (MDA-MB-231) was completed. The promising results of the experiments described in this thesis lead to conclusion that the application of Raman spectroscopy may soon become an important addition to methods used in cell biology. Applications could include the study of cellular processes where non-invasive molecular specific imaging is desirable, such as cell-cell interactions, tissue engineering or drug trafficking inside cells.

7.2 Future directions

Further developments are still required to reduce imaging time and increase sensitivity and specificity of the method. Specificity could be improved by getting better understanding of biological events in cells and building specific molecular data bases of biomolecules, which would allow better assignments of Raman bands and comparisons of obtained spectra. Additionally, new advanced analysis methods could be applied on datasets like machine learning algorithms or linear discriminant analysis.

Intensive research in photon detecting technologies could lead to CCD detectors in the NIR region with higher sensitivity. Such developments could reduce imaging time significantly without compromising on the signal to noise ratio. Additionally, different scanning modes could be applied. Line scanning confocal Raman imaging using 532nm lasers was already used in cell studies. The imaging time was reduced notably in those studies to achieve temporal resolution of ~3 minute per cells. The temporal resolution of pixel-by-pixel Raman imaging with 785nm laser used in this study was of ~10 minutes per cell. However, reshaping the laser beam to line shape reduces laser power on the sample; therefore the Raman scatter would be smaller, on the edge of detection of current NIR detectors. Another approach is the use of NIR solid state laser (i.e. Ti:sapphire) high power lasers in the Raman system where the power density could be maintained at the same level as in point scanning.

Bibliography

[1] A. Zapp Machalek, *et al.*, "Inside the Cells," US Department of Health and Human Science, National Institute of General Medical Sciences, 2005.

[2] B. Alberts, *Essential Cell Biology: An Introduction to the Molecular Biology of the Cell*, 1998.

[3] L. L. Hench and J. R. Jones, *Biomaterials, artificial organs and tissue engineering*: Woodhead Publishing Limited, 2005.

[4] B. A. Teicher, Andrews P.A., *Anticancer drug development Guide*: Humana Press, New-York, 2004.

[5] W. S. El-Deiry, *et al.*, "Imaging and Oncologic Drug Development," *Journal of Clinical Oncology*, vol. 24, pp. 3261-3273, july 2006.

[6] P. Wang, *et al.*, "Cell-based biosensors and its application in biomedicine," *Sensors and Actuators B: Chemical*, vol. 108, pp. 576-584, July 2005.

[7] D. J. Stephens and V. J. Allan, "Light Microscopy Techniques for Live Cell Imaging," *Science*, vol. 300, pp. 82-86, 2003.

[8] F. S. Ligler and C. A. Rowe Taitt, *Optical Biosensors:Today and Tomorrow*, 2 ed.: Science, 2008.

[9] R. Splinter and B. A. Hooper, *An introduction to biomedical optics*. New York: Taylor & Francis, 2007.

[10] J. Zhang, *et al.*, "Inhibition of caspases inhibits the release of apoptotic bodies: Bcl-2 inhibits the initiation of formation of apoptotic bodies in chemotherapeutic agent-induced apoptosis," *Journal of Cell Biology*, vol. 145, pp. 99-108, 1999.

[11] G. Wrobel, *et al.*, "Transmission electron microscopy study of the cell–sensor interface," *Journal of the Royal Society Interface*, vol. 5, pp. 213-22, feb 2008.

[12] Q. Z. Chen, *et al.*, "Bioglass-derived glass-ceramic scaffolds: Study of cell proliferation and scaffold degradation in vitro," *Journal of Biomedical Materials Research Part A*, vol. 84A, pp. 1049-1060, 2007.

[13] E. Karavas, *et al.*, "Combining SEM, TEM, and micro-Raman techniques to differentiate between the amorphous molecular level dispersions and nanodispersions of a poorly water-soluble drug within a polymer matrix," *International Journal of Pharmaceutics*, vol. 340, pp. 76-83, 2007.

[14] K. J. V. Vliet, *et al.*, "The biomechanics toolbox: experimental approaches for living cells and biomolecules," *Acta Materialia*, vol. 51, pp. 5881-5905, November 2003.

[15] G. P. Singh, "Raman Microspectrosopy of Optically Trapped Cells," Universitat Politecnica de Catalunya, Department of Electronic Engineering, 2006.

[16] C. M. Metzler and D. J. Sauke, *Biochemistry : the chemical reactions of living cells*, 2 ed. San Diego: Published by Academic Press, 2003.

[17] K. A. Hinds, *et al.*, "Highly efficient endosomal labeling of progenitor and stem cells with large magnetic particles allows magnetic resonance imaging of single cells," *Blood*, vol. 102, pp. 867-872, 2003.

[18] L. Ciobanu and C. H. Pennington, "3D micron-scale MRI of single biological cells," *Solid State Nuclear Magnetic Resonance*, vol. 25, pp. 138-141, 2004.

[19] K. Konig, "Multiphoton microscopy in life sciences," *Journal of Microscopy*, vol. 2, pp. 83-104, 2000.

[20] B. J. B. Pawley, *Handbook of biological confocal microscopy* vol. 2: Springer, 1995.

[21] D. J. Stephens and V. J. Allan, "Light Microscopy Techniques for Live Cell Imaging," *Science*, vol. 300, pp. 82 - 86, 2003.

[22] H. Schneckenburger, "Review: Total internal reflection fluorescence microscopy: technical innovations and novel applications," *Current Opinion in Biotechnology*, vol. 16, pp. 13-18, February 2005.

[23] J. Schmoranzer, Goulian M. Axelrod D. and S. Simon, "Imaging constitutive exocytosis with total internal reflection fluorescence microscopy," *Journal of Cell Biology*, vol. 149, pp. 23-31, 2000.

[24] D. Zenisek, Steyer J. and W. Almers, "Transport, capture and exocytosis of single synaptic vesicles at active zones," *Nature*, vol. 406, pp. 849-854, 2000.

[25] B. C. Kim and M. B. Gu, "A bioluminescent sensor for high throughput toxicity classification," *Biosensors and Bioelectronics*, vol. 18, pp. 1015-1021, 2003.

[26] H. Horry, *et al.*, "Optimization of a bacterial bioluminescent biosensor through experimental design," *Sensors and Actuators B: Chemical, vol. 127, pp. 649-657*, November 2007.

[27] L. Bouchier-Hayes, *et al.*, "Measuring apoptosis at the single cell level," *Methods*, vol. 44, pp. 222-228, 2008.

[28] R. Day and F. Schaufele, "Fluorescent protein tools for studying protein dynamics in living cells: a review," *Journal of Biomedical Optics*, vol. 13, 2008.

[29] R. Bizzarri, *et al.*, "Green fluorescent protein based pH indicators for in vivo use: a review," *Analytical and Bioanalytical Chemistry*, vol. 393, pp. 1107-1122, 2009.

[30] M. Setou, *et al.*, "Mass microscopy," *Seikagaku. The Journal of Japanese Biochemical Society*, vol. 79, pp. 874-879, 2007.

[31] E. Berman, *et al.*, "Preparation of single cells for imaging/profiling mass spectrometry," *Journal of the American Society for Mass Spectrometry*, vol. 19, pp. 1230-1236, 2008.

[32] C. Deng, *et al.*, "Unifying fluorescence microscopy and mass spectrometry for studying protein complexes in cells," *Molecular & Cellular Proteomics*, vol. 8, p. 1413, 2009.

[33] T. Masujima, "Live Single-cell Mass Spectrometry," *Analytical Sciences*, vol. 25, pp. 953-960, 2009.

[34] A. Svatos, "Mass spectrometric imaging of small molecules," *Trends in Biotechnology*, vol. 28, pp. 425-434, 2010.

[35] A. Bell, *et al.*, "The protein microscope: incorporating mass spectrometry into cell biology," *Nature methods*, vol. 4, pp. 783-784, 2007.

[36] M. Duncan, *et al.*, "The pros and cons of peptide-centric proteomics," *Nature Biotechnology*, vol. 28, pp. 659-664, 2010.

[37] D. Coldrich, "Applications and limits of Raman spectrosocopy in the study of colonic and pulmonary malformations," Universita degli Studi di Trieste, 2006.

[38] M. Diem, *et al.*, "A decade of vibrational micro-spectroscopy of human cells and tissue (1994–2004)," *Analyst*, vol. 129, pp. 880-885, 2004.

[39] E. B. Hanlon, *et al.*, "Prospects for in vivo Raman spectroscopy," *Physics in Medicine and Biology*, vol. 45, pp. 1-59, 2000.

[40] F. S. Parker, *Applications of infrared, raman, and resonance raman spectroscopy in biochemistry*. New York: Plenum Press, 1983.

[41] P. Dumas, *et al.*, "Review : Adding synchrotron radiation to infrared microspectroscopy: what's new in biomedical applications?," *Trends in Biotechnology*, vol. 25, pp. 40-44, January 2007.

[42] E. Brundermann, *et al.*, "Fast quantification of water in single living cells by near-infrared microscopy," *Analyst*, vol. 129, pp. 893-896, 2004.

[43] S. Boydston-White, *et al.*, "Cell-cycle-dependent variations in FTIR micro-spectra of single proliferating HeLa cells: Principal component and artificial neural network analysis," *Biochimica et Biophysica Acta (BBA) - Biomembranes Vibrational Microscopic Imaging: Towards Molecular Pathology*, vol. 1758, pp. 908-914, July 2006.

[44] A. J. Bentley, *et al.*, "Characterization of human corneal stem cells by synchrotron infrared micro-spectroscopy," *Mol Vis.*, vol. 13, pp. 237–242., Feb 2007.

[45] A. Downes, *et al.*, "A versatile CARS microscope for biological imaging," *Journal of Raman Spectroscopy*, vol. 40, pp. 757-762, 2009.

[46] I. Notingher and L. L. Hench, "Raman microspectroscopy: a noninvasive tool for studies of individual living cells in vitro," *Expert Review of Medical Devices,* vol. 3, pp. 215-234, 2006.

[47] M. Harz, *et al.*, "Vibrational spectroscopy- a powerful tool for the rapid identification of microbial cells at the single-cell level," *Cytometry A.*, vol. 75, pp. 104-13, february 2009.

[48] R. L. McCreery, *Raman Spectroscopy for Chemical Analysis*: Wiley, 2000.

[49] B. I. R. Lewis, *Handbook of Raman Spectroscopy: From the Research Laboratory to the Process Line*. New York: Marcel Dekker, 2001.

[50] V. Otieno-Alego, "75 Years on and Forensic Laboratories are Slowly but Surely Ramanising," *The Forensic Bulletin,* vol. Australia and New Zealand Forensic Science Inc. Summer Issue, pp. 20-23, 2004.

[51] H. G. M. Edwards and J. M. Chalmers, *Raman Spectroscopy in Art History and Archaeology*: Royal Society of Chemistry, London, 2004.

[52] H. G. M. Edwards, *et al.*, "Raman spectroscopic analyses of preserved historical specimens of human hair attributed to Robert Stephenson and Sir Isaac Newton," *Analyst,* vol. 129, pp. 956-962, 2004.

[53] M. H. Gniadecka, *et al.*, "NIR-FT Raman spectrosocpu of the mummiefied skin of Chrabaya mummies from Peru," *Chungara (Arica),* vol. 33, 2001.

[54] G. Keller, "In vitro differentiation of embryonic stem cells," *Current Opinion in Cell Biology,* vol. 7, pp. 862-869, 1995.

[55] G. Puppels, *et al.*, "Laser irradiation and Raman spectroscopy of single living cells and chromosomes: Sample degradation occurs with 514.5 nm but not with 660 nm laser light* 1," *Experimental cell research,* vol. 195, pp. 361-367, 1991.

[56] I. Notingher, *et al.*, "In situ characterisation of living cells by Raman spectroscopy," *Spectroscopy-an International Journal,* vol. 16, pp. 43-51, 2002.

[57] R. Tatra, *et al.*, "Comparable Raman Spectroscopy across different instruments and excitation wavelengths," NPL report2004.

[58] H.-U. Gremlich and B. Yan, *Infrared and raman spectroscopy of biological materials* vol. 24. New York: CRC Press, 2000.

[59] S. Koljenovic, "Towards Clinico-Pathological Application of Raman Spectroscopy," Erasmus Universiteit Rotterdam, *2008.*

[60] L. A. Reisner, *et al.*, "A prototype biosensor-integrated image-guided surgery system," *International Journal of Medical Robotics and Computer Assisted Surgery,* vol. 3, pp. 82-88, Mar 2007.

[61] K. W. Short, *et al.*, "Raman Spectroscopy Detects Biochemical Changes Due to Proliferation in Mammalian Cell Cultures," *Biophysical Journal,* vol. 88, pp. 4274-4288, 2005.

[62] T. J. Harvey, *et al.*, "Classification of fixed urological cells using Raman tweezers," *Journal of Biophotonics,* pp. 47-69, 2009.

[63] J. W. Chan, *et al.*, "The effect of cell fixation on the discrimination of normal and leukemia cells with laser tweezers Raman spectroscopy," *Biopolymers,* vol. 91, pp. 132-139, 2009.

[64] K. C. Schuster, *et al.*, "Single-cell analysis of bacteria by Raman microscopy: spectral information on the chemical composition of cells and on the heterogeneity in a culture," *Journal of Microbiological Methods,* vol. 42, pp. 29-38, 2000.

[65] P. Crow, *et al.*, "The use of Raman spectroscopy to differentiate between different prostatic adenocarcinoma cell lines," *British Journal of Cancer,* vol. 92, pp. 2166–2170, 2005.

[66] R. J. Swain, *et al.*, "Non-invasive analysis of cell cycle dynamics in single living cells with Raman micro-spectroscopy," *Journal of Cellular Biochemistry,* vol. 104, pp. 1427-1438, 2008.

[67] I. Notingher, *et al.*, "New detection system for toxic agents based on continuous spectroscopic monitoring of living cells," *Biosensors & Bioelectronics,* vol. 20, pp. 780-789, Nov 2004.

[68] G. J. Puppels, *et al.*, "Studying single living cells and chromosomes by confocal Raman microspectroscopy," *Nature,* vol. 347, pp. 301-303, 1990.

[69] N. Uzunbajakava, *et al.*, "Nonresonant confocal Raman imaging of DNA and protein distribution in apoptotic cells," *Biophysical Journal*, vol. 84, pp. 3968-81, 2003.

[70] I. Notingher, *et al.*, "Discrimination between ricin and sulphur mustard toxicity in vitro using Raman spectroscopy," *Journal of the Royal Society Interface*, vol. 1, pp. 79-90, Nov 2004.

[71] S. Verrier, *et al.*, "In situ monitoring of cell death using Raman microspectroscopy," *Biopolymers*, vol. 74, pp. 157-162, 2004.

[72] H. Hamaguchi, "Linear and Non-Linear Raman Spectroscopy and Imaging of Living Cells; Life and Death at the Cellular Level," in *2007 Pacific Rim Conference on Lasers and Electro-Optics*, Seoul, South Korea, 2007, pp. 191-192.

[73] C. A. Owen, *et al.*, "In vitro toxicology evaluation of pharmaceuticals using Raman micro-spectroscopy," *Journal of Cellular Biochemistry*, vol. 99, pp. 178-186, 2006.

[74] K. L. Brown, *et al.*, "Raman spectroscopic differentation of activated versus non-activated T lymphocytes: An in vitro study of an acute allograft rejection model," *Journal of Immunological Methods*, vol. 340, pp. 48-54, 2008.

[75] P. Rosch, *et al.*, "Chemotaxonomic identification of single bacteria by micro-Raman spectroscopy: application to clean-room-relevant biological contaminations," *Applied and Environmental Microbiology*, vol. 71, pp. 1626-1637, 2005.

[76] R. Rosch, *et al.*, "Identification of single eukaryotic cells with micro-Raman spectroscopy," *Biopolymers*, vol. 82, pp. 312-316, 2006.

[77] N. Gierlinger and M. Schwanninger, "Chemical Imaging of Poplar Wood Cell Walls by Confocal Raman Microscopy," *Plant Physiology*, vol. 140, pp. 1246-1254, 2006.

[78] C. Xie, *et al.*, "Optical trapping and Raman spectroscopy of single living cells and single organelles," in *QELS Quantum Electronics and Laser Science Postconference Digest*, 2003, p. 2.

[79] O. F. Dyson, *et al.*, "Raman tweezers provide the fingerprint of cells supporting the late stages of KSHV reactivation," *Journal of Cellular and Molecular Medicine*, vol. 13, pp. *1920-1932, 2008.*

[80] L. Puskar, *et al.*, "Raman *acoustic levitation spectroscopy* of red blood cells and Plasmodium falciparum trophozoites," *Lab On A Chip, vol. 7, pp. 1125-1131, 2007.*

[81] K. Van Vliet and P. Hinterdorfer, "Review: Probing drug-cell interactions," *Nanotoday*, vol. 1, pp. 18-25, 2006.

[82] V. Maquet, *et al.*, "Porous poly (alfa-hydroxyacid)/Bioglass composite scaffolds for bone tissue engineering. I: preparation and in vitro characterisation," *Biomaterials*, vol. 25, pp. 4185-4194, 2004.

[83] R. A. MacDonald, *et al.*, "Collagen-carbon nanotube composite materials as scaffolds in tissue engineering," *Journal of Biomedical Materials Research*, vol. 74A, pp. 489-496, 2005.

[84] N. Uzunbajakava, *et al.*, "Nonresonant Raman imaging of protein distribution in single human cells," *Biopolymers.*, vol. 72, pp. 1-9., 2003.

[85] C. Krafft, *et al.*, "Studies on Stress-Induced Changes at the Subcellular Level by Raman Microspectroscopic Mapping," *Analytical Chemistry*, vol. 78, pp. 4424-4429, 2006.

[86] C. Matthäus, *et al.*, "Label-Free Detection of Mitochondrial Distribution in Cells by Nonresonant Raman Microspectroscopy," *Biophysical Journal*, vol. 93, pp. 668-673, 2007.

[87] H.-J. van Manen, *et al.*, "Single-cell Raman and fluorescence microscopy reveal the association of lipid bodies with phagosomes in leukocytes," *Proceedings of the National Academy of Sciences of the United States of America*, vol. 102, pp. 10159-10164, July 19, 2005 2005.

[88] C. Matthaus, *et al.*, "Raman and infrared microspectral imaging of mitotic cells," *Applied Spectroscopy*, vol. 60, pp. 1-8, 2006.

[89] C. Matthaus, *et al.*, "New ways of imaging uptake and intracellular fate of liposomal drug carrier systems inside individual cells, based on Raman microscopy," *Molecular Pharmaceutics*, vol. 5, pp. 287-93, Mar-Apr 2008.

[90] A. Q. Liu, *et al.*, "Label-free detection with micro optical fluidic systems (MOFS): a review," *Analytical and Bioanalytical Chemistry*, vol. 391, pp. 2443-2452, Aug 2008.

[91] H.-J. van Manen and C. Otto, "Hybrid Confocal Raman Fluorescence Microscopy on Single Cells Using Semiconductor Quantum Dots," *Nano Letters,* vol. 7, pp. 1631-1636, 2007.

[92] H. Yao, *et al.*, "Raman spectroscopic analysis of apoptosis of single human gastric cancer cells," *Vibrational Spectroscopy,* vol. 50, pp. 193-197, 2009.

[93] J. Mason and T. O'Leary, "Effects of formaldehyde fixation on protein secondary structure: a calorimetric and infrared spectroscopic investigation," *Journal of Histochemistry and Cytochemistry,* vol. 39, p. 225, 1991.

[94] Z. Huang, *et al.*, "Effect of formalin fixation on the near-infrared Raman spectroscopy of normal and cancerous human bronchial tissues," *International Journal of Oncology,* vol. 23, pp. 649-656, 2003.

[95] F. Draux, *et al.*, "Raman spectral imaging of single living cancer cells: a preliminary study," *Analyst,* vol. 134, pp. 542-8, 2009.

[96] Z. Liu, *et al.*, "siRNA Delivery into Human T Cells and Primary Cells with Carbon-Nanotube Transporters," *Angewandte Chemie - International Edition,* vol. 46, pp. 2023-2027, 2007.

[97] Y. Harada, *et al.*, "Imaging of anticancer agent distribution by a slit-scanning Raman microscope," in *Conference on Biomedical Optical Spectroscopy*, San Jose, 2008, pp. 85308-85308.

[98] Y. Harada, *et al.*, "Intracellular dynamics of topoisomerase I inhibitor, CPT-11, by slit-scanning confocal Raman microscopy," *Histochemistry and Cell Biology,* vol. 132, pp. 39-46, 2009.

[99] K. Hamada, *et al.*, "Raman microscopy for dynamic molecular imaging of living cells," *Journal of Biomedical Optics,* vol. 13, 2008.

[100] A. Hermelink, *et al.*, "Phenotypic heterogeneity within microbial populations at the single-cell level investigated by confocal Raman microspectroscopy," *Analyst,* vol. 134, pp. 1149-1153, 2009.

[101] K. Meister, *et al.*, "Confocal Raman microspectroscopy as an analytical tool to assess the mitochondrial status in human spermatozoa," *Analyst,* vol. 135, pp. 1370-1374, 2010.

[102] V. Pully, *et al.*, "Microbioreactors for Raman Microscopy of Stromal Cell Differentiation," *Analytical Chemistry,* vol. 82, pp. 1844-1850, 2010.

[103] I. Notingher, "Raman Spectroscopy Cell-based Biosensors," *Sensors,* vol. 7, pp. 1343-1358, 2007.

[104] J. W. Chen, *et al.*, "Detection of adenosine using surface-enhanced Raman scattering based on structure-switching signaling aptamer," *Biosensors & Bioelectronics,* vol. 24, pp. 66--71, Sep 2008.

[105] K. Fujita and N. Smith, "Label-free molecular imaging of living cells," *Molecules and Cells,* vol. 26, pp. 530-5, Dec 2008.

[106] S. Wachsmann-Hogiu, *et al.*, "Chemical analysis in vivo and in vitro by Raman spectroscopy-from single cells to humans," *Current Opinion in Biotechnology,* vol. 20, pp. 63-73, March 4 2009.

[107] R. Swain and M. Stevens, "Raman microspectroscopy for non-invasive biochemical analysis of single cells," *Biochemical Society Transactions,* vol. 35, pp. 544-9, Jun 2007.

[108] Z. Movasaghi, *et al.*, "Raman spectroscopy of biological tissues," *Applied Spectroscopy Reviews,* vol. 42, pp. 493-541, 2007.

[109] C. Raman, "A new Radiation," *Indian Journal of Physics,* vol. 2, pp. 387-398, 1928.

[110] J. Fischer, "George Placzek - an unsung hero of physics," *CERN Courier, International Journal of High-Energy Physics,* vol. 45, Aug 23 2005.

[111] F. Adar, *et al.*, "Evolution of Instrumentation for Detection of the Raman Effect as Driven by Available Technologies and by Developing Applications," *Journal of Chemical Education,* vol. 84, p. 50, 2007.

[112] D. Schwartz, "Raman Spectroscopy: Introductory Tutorial," Department of Chemical Engineering, University of Washington.

[113] B. Weckhuysen, *et al.*, *Spectroscopy of transition metal ions on surfaces*. Leuven: Leuven University Press, 2000.

[114] G. Turrel and J. Corset, *Raman Microscopy: Development and Applications*. London: Elsevier Academy Press, 1996.

[115] E. J. Ayars, *et al.*, "Fundamental differences between micro- and nano- Raman spectroscopy," *Journal of Microscopy*, vol. 202, pp. 142-147, 2000.

[116] J. Ferraro, *et al.*, *Introductory raman spectroscopy*. London: Academic Press, 2003.

[117] I. Serdyuk, *et al.*, "Methods in Molecular Biophysics." Cambridge: Cambridge University Press, 2007.

[118] J. Chalmers and P. Griffiths, *Handbook of vibrational spectroscopy*. New York: Wiley, 2001.

[119] G. J. Puppels, *et al.*, "Description and performance of a highly sensitive confocal Raman microspectrometer," *Journal of Raman Spectroscopy*, vol. 22, pp. 217-225, Apr 1991.

[120] N. Uzunbajakava and C. Otto, "Combined Raman and continuous-wave-excited two-photon fluorescence cell imaging," *Optics Letters.*, vol. 28, pp. 2073-2075, 2003.

[121] C. Johannessen, *et al.*, "Resonance Raman optical activity and surface enhanced resonance Raman optical activity analysis of cytochrome c," *Journal of Physical Chemistry A*, vol. 111, pp. 7771-7776, Aug 2007.

[122] K. Brose, *et al.*, "Polarised Raman measurements on the core complex of crystallised photosystem II," *Physica Status Solidi (B)*, vol. 246, pp. 2813-2816, 2009.

[123] E. Ly, *et al.*, "Probing tumor and peritumoral tissues in superficial and nodular basal cell carcinoma using polarized Raman microspectroscopy," *Experimental dermatology*, vol. 19, pp. 68-73, 2010.

[124] K. Ramser, *et al.*, "Resonance Raman spectroscopy of optically trapped functional erythrocytes," *Journal of Biomedical Optics*, vol. 9, pp. 593-600, 2004.

[125] B. R. Wood, *et al.*, "Resonance Raman spectroscopy of red blood cells using near-infrared laser excitation," *Analytical and Bioanalytical Chemistry*, vol. 387, pp. 1691-1703, Mar 2007.

[126] B. Wood and D. McNaughton, "Resonance Raman spectroscopy in malaria research," *Expert Review of Proteomics*, vol. 3, pp. 525-44, Oct 2006.

[127] C. Onogi and H. Hamaguchi, "In vivo Detection of Ferrous Cytochrome c in Mitochondria of Single Living Yeast Cells by Resonance Raman microspectroscopy," 2010, pp. 362-363.

[128] M. Darvin, *et al.*, "Non-invasive in vivo detection of the carotenoid antioxidant substance lycopene in the human skin using the resonance Raman spectroscopy," *Laser Physics Letters*, vol. 3, pp. 460-463, 2006.

[129] M. Osada, *et al.*, "Near-infrared Fourier transform Raman spectroscopic analysis of proteins, water and lipids in intact normal stratum corneum and psoriasis scales," *Experimental dermatology*, vol. 13, pp. 391-395, 2004.

[130] L. G. Rodriguez, *et al.*, "Coherent anti-stokes Raman scattering microscopy: A biological review," *Cytometry Part A*, vol. 69A, pp. 779-791, 2006.

[131] X. Nan, *et al.*, "Vibrational imaging of lipid droplets in live fibroblast cells with coherent anti-Stokes Raman scattering microscopy," *Journal of Lipid Research*, vol. 44, pp. 2202-2208, 2003.

[132] H. A. Rinia, *et al.*, "Quantitative label-free imaging of lipid composition and packing of individual cellular lipid droplets using multiplex CARS microscopy," *Biophysical Journal*, vol. 95, pp. 4908-4914, Nov 2008.

[133] X. Nan, *et al.*, "Nonperturbative chemical imaging of organelle transport in living cells with coherent anti-stokes Raman scattering microscopy," *Biophysical Journal*, vol. 91, pp. 728-35, Jul 2006.

[134] H. Kano and H. Hamaguchi, "Supercontinuum dynamically visualizes a dividing single cell," *Analytical Chemistry*, vol. 79, pp. 8967-8973, Dec 2007.

[135] K. Shi, *et al.*, "Broadband coherent anti-Stokes Raman scattering spectroscopy in supercontinuum optical trap," *Applied Physics Letters*, vol. 90, 2007.

[136] Y. Lee, *et al.*, "Characterization of three-color CARS in a two-pulse broadband CARS spectrum," *Optics letters*, vol. 32, pp. 3370-3372, 2007.

[137] D. A. Stuart, *et al.*, "Biological applications of localised surface plasmonic phenomenae," *IEE Proceedings Nanobiotechnol*, vol. 152, pp. 13-32, Feb 2005.

[138] I. Nabiev, *et al.*, "Review: Applications of Raman and Surface-Enhanced Raman Scattering Spectroscopy in Medicine," *Journal of Raman Spectroscopy,* vol. 25, pp. 13-23, 1994.

[139] S. Lal, *et al.*, "Tailoring plasmonic substrates for surface enhanced spectroscopies," *Chemical Society Reviews,* vol. 37, pp. 898-911, May 2008.

[140] K. Fujita, *et al.*, "Time-resolved observation of surface-enhanced Raman scattering from gold nanoparticles during transport through a living cell," *Journal of Biomedical Optics,* vol. 14, 2009.

[141] J. Kneipp, *et al.*, "Optical probing and imaging of live cells using SERS labels," *Journal of Raman Spectroscopy,* vol. 40, pp. 1-5, 2009.

[142] J. Scaffidi, *et al.*, "SERS-based plasmonic nanobiosensing in single living cells," *Analytical and Bioanalytical Chemistry,* vol. 393, pp. 1135-1141, 2009.

[143] W. Xie and Z. Y. Wang L, Su L Shen A Tan J Hu J., "Nuclear Targeted Nanoprobe for Single Living Cell Detection by Surface-Enhanced Raman Scattering," *Bioconjugate Chemistry,* vol. 20, pp. 768-773, 2009.

[144] V. Biju, *et al.*, "Combined Spectroscopic and Topographic Characterization of Nanoscale Domains and Their Distributions of a Redox Protein on Bacterial Cell Surfaces," *Langmuir,* vol. 23, pp. 1333-1338, 2007.

[145] U. Neugebauer, *et al.*, "On the Way to Nanometer-Sized Information of the Bacterial Surface by Tip-Enhanced Raman Spectroscopy," *ChemPhysChem,* pp. 1428-1430, 2006.

[146] W. Demtröder, *Laser spectroscopy: basic concepts and instrumentation*. Berlin: Springer Verlag, 2003.

[147] W. Silfvast, *Laser fundamentals*. Cambridge: Cambridge University Press, 2004.

[148] H. Liang, *et al.*, "Wavelength dependence of cell cloning efficiency after optical trapping," *Biophysical journal,* vol. 70, pp. 1529-1533, 1996.

[149] K. Neuman, *et al.*, "Characterization of photodamage to Escherichia coli in optical traps," *Biophysical Journal,* vol. 77, pp. 2856-2863, 1999.

[150] M. Henini and M. Razegh, *Handbook of infrared detection technologies*. Oxford: Elsevier, 2002.

[151] R. Snook, *et al.*, "Raman tweezers and their application to the study of singly trapped eukaryotic cells," *Integrative Biology,* vol. 1, pp. 43-52, 2009.

[152] V. V. Pully, *et al.*, "Hybrid Rayleigh, Raman and two-photon excited fluorescence spectral confocal microscopy of living cells," *Journal of Raman Spectroscopy,* vol. 41, pp. 599-608, 2009.

[153] A. T. Tu, *Raman spectroscopy in biology: principles and applications*. New York: John Wiley and Sons, 1982.

[154] Semrock. (12.10.2010). *Semrock: LPD01-785RU-25.* Available: http://www.semrock.com/Catalog/Detail.aspx?FilterPartID=124&CategoryID=37

[155] Semrock. (12.10.2010). *Semrock: LP02-785RE-25.* Available: http://www.semrock.com/Catalog/Detail.aspx?FilterPartID=196&CategoryID=69

[156] M. Pelletier, *Analytical applications of Raman spectroscopy*. Malden: Wiley-Blackwell, 1999.

[157] Newport. (12.10.2010). *Newport Corporation, Richardson Gratings - Products: Table 1.*

[158] Andor. (12.10.2010). *Andor iDus Spectroscopy CCD - Camera Models.* Available: http://www.andor.com/scientific_cameras/idus/models/default.aspx?iProductCodeID=51

[159] I. Notingher, *et al.*, "In situ non-invasive spectral discrimination between bone cell phenotypes used in tissue engineering," *Journal of Cellular Biochemistry,* vol. 92, pp. 1180-1192, 2004.

[160] C. Moisii, *et al.*, "Raman spectroscopy of discrete silica supported vanadium oxide: assignment of fundamental stretching modes," *Journal of Materials Chemistry,* vol. 15, pp. 3519-3524, 2005.

[161] D. Rudan-Tasic and C. Klofutar, "Characteristics of vegetable oils of some Slovene manufacturers," *Acta Chimica Slovenica,* vol. 46, pp. 511-521, 1999.

[162] S. Kasarova, *et al.*, "Analysis of the dispersion of optical plastic materials," *Optical Materials,* vol. 29, pp. 1481-1490, 2007.

[163] A. Barnard, *The diamond formula: diamond synthesis - a gemmological perspective.* Oxford: Butterworth-Heinemann, 2000.

[164] D. Hutsebaut, *et al.*, "Evaluation of an accurate calibration and spectral standardization procedure for Raman spectroscopy," *Analyst,* vol. 130, pp. 1204-1214, 2005.

[165] ASTM, "Standard Guide for Raman Shift Standards for Spectrometer Calibration," vol. ASTM E1840-96: ASTM International, 2002.

[166] M. Lupek, *et al.*, "Noise reduction in Raman spectra: Finite impulse response filtration versus Savitzky-Golay smoothing," *Journal of Raman Spectroscopy,* vol. 38, pp. 1174-1179, 2007.

[167] H. Bohr, *Handbook of Molecular Biophysics: Methods and Applications*: Vch Verlagsgesellschaft Mbh, 2009.

[168] Slobodan, *et al.*, "A comparison of Raman chemical images produced by univariate and multivariate data processing—a simulation with an example from pharmaceutical practice," *Analyst,* vol. 129, pp. 1001 - 1007, 2004.

[169] I. Notingher, "Multivariate analysis of Raman spectra for in vitro non-invasive studies of living cells," *Journal of Molecular Structure,* vol. 744-747, pp. 179-185, 2005.

[170] C. A. Owen, *et al.*, *"Raman spectroscopy* as a tool for preliminary drug testing on human cells," *Journal of Pharmacy and Pharmacology, vol. 56, pp. S51-S52, 2004.*

[171] P. Lasch, *et al.*, "Imaging of colorectal adenocarcinoma using FT-IR microspectroscopy and cluster analysis," *Biochimica et Biophysica Acta,* vol. 1688, pp. 176-186, 2004.

[172] C. Krafft, *et al.*, "Disease recognition by infrared and Raman spectroscopy," *Journal of Biophotonics,* vol. 2, pp. 13-28, Feb 2009.

[173] M. E. Tipping and C. M. Bishop, "Probabilistic Principal Component Analysis," *Royal Statistical Society,* vol. 61, pp. 611-622, 1999.

[174] E. Marengo, *et al.*, "Review: Numerical approaches for quantitative analysis of two-dimensional maps: A review of commercial software and home-made systems," *Proteomics,* vol. 5, pp. 654-666, Jan 2005.

[175] S. Sasic, *et al.*, "Raman line mapping as a fast method for analyzing pharmaceutical bead formulations," *Analyst,* vol. 130, pp. 1530-1536, 2005.

[176] R. Perez-Pueyo, *et al.*, "A fuzzy logic system for band detection in Raman spectroscopy," *Journal of Raman Spectroscopy,* vol. 35, pp. 808-812, 2004.

[177] R. Perez-Pueyo, *et al.*, "Fuzzy Approach for Identifying Artistic Pigments with Raman Spectroscopy," *Applied spectroscopy,* vol. 63, pp. 947-957, 2009.

[178] X. Wang and J. Garibaldi, "A comparison of fuzzy and non-fuzzy clustering techniques in cancer diagnosis," in *2nd International Conference in Computational Intelligence in Medicine and Healthcare - The Biopattern Conference*, Lisbon, 2005.

[179] X. Wang, *et al.*, "Application of the fuzzy C-means clustering method on the analysis of non pre-processed FTIR data for cancer diagnosis," in *8th Australian and New Zealand Conference on Intelligent Information Systems*, Sydney, 2003, pp. 233-238.

[180] P. Guermonprez, *et al.*, "Antigen presentation and T cell stimulation by dendritic cells," *Annual Review of Immunology,* vol. 20, pp. 621-667, 2003.

[181] R. Evans, *et al.*, "Integrins in immunity," *Journal of Cell Science,* vol. 122, pp. 215-225, 2009.

[182] M. Al-Alwan, *et al.*, "Cutting edge: dendritic cell actin cytoskeletal polarization during immunological synapse formation is highly antigen-dependent," *The Journal of Immunology,* vol. 171, pp. 4479-4483, 2003.

[183] M. C. Montoya, *et al.*, "Cell adhesion and polarity during immune interactions," *Immunological reviews,* vol. 186, pp. 68-82, 2002.

[184] D. Davis and M. Dustin, "What is the importance of the immunological synapse?," *Trends in immunology,* vol. 25, pp. 323-327, 2004.

[185] C. Wülfing and M. Davis, "A receptor/cytoskeletal movement triggered by costimulation during T cell activation," *Science,* vol. 282, pp. 2266-2269, 1998.

[186] E. Chhabra and H. Higgs, "The many faces of actin: matching assembly factors with cellular structures," *nature cell biology,* vol. 9, pp. 1110-1121, 2007.

[187] J. Delon, *et al.*, "Antigen-dependent and-independent Ca2+ responses triggered in T cells by dendritic cells compared with B cells," *Journal of Experimental Medicine,* vol. 188, pp. 1473-1484, 1998.

[188] J. Jacobelli, *et al.*, "T cell trans-endothelial migration and homing to lymph nodes rely on Myosin-IIA mediated acto-myosin contractility," *The Journal of Immunology,* vol. 182, p. 94.25, 2009.

[189] S. García-Nieto, *et al.*, "Laminin and Fibronectin Treatment Leads to Generation of Dendritic Cells with Superior Endocytic Capacity," *Plos One,* vol. 5, 2010.

[190] T. Geijtenbeek, *et al.*, "Identification of DC-SIGN, a novel dendritic cell-specific ICAM-3 receptor that supports primary immune responses," *Cell,* vol. 100, pp. 575-585, 2000.

[191] P. Kalinski and H. Okada, "Polarized dendritic cells as cancer vaccines: Directing effector-type T cells to tumors," *Seminars in Immunology,* vol. 22, pp. 173-182, 2010.

[192] P. Mosca, *et al.*, "Dendritic cell vaccines," *Front Biosci,* vol. 12, pp. 4050-60, 2007.

[193] O. Proudfoot, *et al.*, "Dendritic cell vaccination," *Expert Review of Vaccines,* vol. 6, pp. 617-633, 2007.

[194] R. Steinman and J. Banchereau, "Taking dendritic cells into medicine," *Nature,* vol. 449, pp. 419-426, 2007.

[195] K. Brown, *et al.*, "Raman spectroscopic differentiation of activated versus non-activated T lymphocytes: An in vitro study of an acute allograft rejection model," *Journal of immunological methods,* vol. 340, pp. 48-54, 2009.

[196] Z. Liu, *et al.*, "Multiplexed Multicolor Raman Imaging of Live Cells with Isotopically Modified Single Walled Carbon Nanotubes," *Journal of the American Chemical Society,* vol. 130, pp. 13540-13541, 2008.

[197] V. V. Pully and C. Otto, "The intensity of the 1602 cm(-1) band in human cells is related to mitochondrial activity," *Journal of Raman Spectroscopy,* vol. 40, pp. 473-475, May 2009.

[198] K. Brown, *et al.*, "Differentiation of alloreactive versus CD3/CD28 stimulated T-lymphocytes using *Raman spectroscopy: A greater* specificity for noninvasive acute renal allograft rejection detection," *Cytometry Part A, vol. 75, pp. 917-923, 2009.*

[199] J. Chan, *et al.*, "Nondestructive identification of individual leukemia cells by laser trapping Raman spectroscopy," *Analytical Chemistry,* vol. 80, pp. 2180-2187, 2008.

[200] P. Zinin, *et al.*, "Visible, near-infrared, and ultraviolet laser-excited Raman spectroscopy of the monocytes/macrophages (U937) cells," *Journal of Raman Spectroscopy,* vol. 41, pp. 268-274, 2010.

[201] C. Horlock, *et al.*, "Analysis of proteomic profiles and functional properties of human peripheral blood myeloid dendritic cells, monocyte-derived dendritic cells and the dendritic cell-like KG-1 cells reveals distinct characteristics," *Genome Biology,* vol. 8, p. R30, 2007.

[202] M. Gordón-Alonso, *et al.*, "Actin dynamics at the immunological synapse," *Cell Health and Cytoskeleton,* vol. 2, pp. 33-47, 2010.

[203] M. Dustin and J. Cooper, "The immunological synapse and the actin cytoskeleton: molecular hardware for T cell signaling," *Nature Immunology,* vol. 1, pp. 23-29, 2000.

[204] R. C. Taylor, *et al.*, "Apoptosis: controlled demolition at the cellular level," *Nature Reviews Molecular Cell Biology,* vol. 9, pp. 231-241, 2008.

[205] T. G. Cotter, "Apoptosis and cancer: the genesis of a research field," *Nature Reviews Cancer,* vol. 9, pp. 501-507, 2009.

[206] P. Lasch, *et al.*, "FT-IR spectroscopic investigations of single cells on the subcellular level," *Vibrational Spectroscopy,* vol. 28, pp. 147-157, 2002.

[207] M. Kuimova, *et al.*, "Chemical imaging of live cancer cells in the natural aqueous environment," *Applied Spectroscopy,* vol. 63, pp. 164-171, 2009.

[208] B. R. Wood and D. McNaughton, "Micro-Raman characterization of high- and low-spin heme moieties within single living erythrocytes," *Biopolymers.,* vol. 67, pp. 259-62., 2002.

[209] Y. Takai, *et al.*, "Lipid structure of cytotoxic granules in living human killer T lymphocytes studied by Raman microspectroscopy," *Biochimica et Biophysica Acta (BBA) - General Subjects,* vol. 1335, pp. 199-208, 1997.

[210] I. Notingher, *et al.*, "In situ spectral monitoring of mRNA translation in embryonic stem cells during differentiation in vitro," *Analytical Chemistry*, vol. 76, pp. 3185-3193, 2004.

[211] I. Notingher, *et al.*, "Spectroscopic study of human lung epithelial cells (A549) in culture: Living cells versus dead cells," *Biopolymers*, vol. 72, pp. 230-240, 2003.

[212] R. Swain, *et al.*, "Spectral Monitoring of Surfactant Clearance during Alveolar Epithelial Type II Cell Differentiation," *Biophysical Journal*, vol. 95, pp. 5978-5987, 2008.

[213] G. Jell, *et al.*, "Bioactive glass-induced osteoblast differentiation: A noninvasive spectroscopic study," *Journal of Biomedical Materials Research Part A*, vol. 86A, pp. 31-40, 2008.

[214] T. Harvey, *et al.*, "Spectral discrimination of live prostate and bladder cancer cell lines using Raman optical tweezers," *Journal of Biomedical Optics*, vol. 13, 2008.

[215] J. W. Chan, *et al.*, "Label-Free Separation of Human Embryonic Stem Cells and Their Cardiac Derivatives Using Raman Spectroscopy," *Analytical Chemistry*, vol. 81, pp. 1324-1331, 2009.

[216] K. Chen, *et al.*, "Diagnosis of colorectal cancer using Raman spectroscopy of laser-trapped single living epithelial cells," *Optics Letters*, vol. 31, pp. 2015-2017, 2006.

[217] Z. Tao, *et al.*, "Using Raman spectroscopy to analyze apoptosis of gastric cancer cells induced by cisplatin," *Spectroscopy and Spectral Analysis*, vol. 29, pp. 2442-2445, 2009.

[218] G. Pyrgiotakis, *et al.*, "Cell Death Discrimination with Raman Spectroscopy and Support Vector Machines," *Annals of biomedical engineering*, vol. 37, pp. 1464-1473, 2009.

[219] C. Krafft, *et al.*, "Identification of organelles and vesicles in single cells by Raman microspectroscopic mapping," *Vibrational Spectroscopy*, vol. 38, pp. 85-93, 2005.

[220] S. Y. Arzhantsev, *et al.*, "Localization study of co-phthalocyanines in cells by Raman micro(spectro)scopy," *Journal of Raman Spectroscopy*, vol. 30, pp. 205-208, 1999.

[221] A. Zumbusch, *et al.*, "Three-Dimensional Vibrational Imaging by Coherent Anti-Stokes Raman Scattering," *Physical Review Letters*, vol. 82, pp. 4142-4145, 1999.

[222] G. W. Sledge, "Etoposide in the management of metastatic breast-cancer," *Cancer*, vol. 67, pp. 266-270, Jan 1991.

[223] C. B. Hendricks, *et al.*, "Effect of p-glycoprotein expression on the accumulation and cytotoxicity of topotecan (sk-and-f-10484), a new camptothecin analog," *Cancer Research*, vol. 52, pp. 2268-2278, Apr 1992.

[224] Y.-S. Huang, *et al.*, "Molecular-Level Investigation of the Structure, Transformation, and Bioactivity of Single Living Fission Yeast Cells by Time- and Space-Resolved Raman Spectroscopy," *Biochemistry*, vol. 44, pp. 10009-10019, 2005.

[225] B. R. Wood, *et al.*, "Shedding new light on the molecular architecture of oocytes using a combination of synchrotron Fourier transform-infrared and Raman spectroscopic mapping," *Analytical Chemistry*, vol. 80, pp. 9065-72, 2008.

[226] J. M. Hakumäki and K. M. Brindle, "Techniques: Visualizing apoptosis using nuclear magnetic resonance," *Trends in Pharmacological Sciences*, vol. 24, pp. 146-149, 2003.

[227] J. E. Schmitz, *et al.*, "1H MRS-visible lipids accumulate during apoptosis of lymphoma cells in vitro and in vivo," *Magnetic Resonance in Medicine*, vol. 54, pp. 43-50, 2005.

[228] I. Barba, *et al.*, "The Relationship between Nuclear Magnetic Resonance-Visible Lipids, Lipid Droplets, and Cell Proliferation in Cultured C6 Cells," *Cancer Research*, vol. 59, pp. 1861-1868, April 1, 1999 1999.

[229] A. A. Spector, *et al.*, "Lipid nutrition and metabolism of cultured mammalian cells," *Progress in Lipid Research*, vol. 19, pp. 155-186, 1980.

[230] P. T. Bozza, *et al.*, "Leukocyte lipid body formation and eicosanoid generation: cyclooxygenase-independent inhibition by aspirin," *Proceedings of the National Academy of Sciences of the United States of America*, vol. 93, pp. 11091-11096, October 1, 1996 1996.

[231] M. Di Vito, *et al.*, "1H NMR-visible mobile lipid domains correlate with cytoplasmic lipid bodies in apoptotic T-lymphoblastoid cells," *Biochimica et Biophysica Acta (BBA) - Molecular and Cell Biology of Lipids*, vol. 1530, pp. 47-66, 2001.

[232] H. Robenek, *et al.*, "Adipophilin-enriched domains in the ER membrane are sites of lipid droplet biogenesis," *Journal of Cell Science*, vol. 119, pp. 4215-4224, October 15, 2006 2006.

[233] R. A. Coleman and D. P. Lee, "Enzymes of triacylglycerol synthesis and their regulation," *Progress in Lipid Research,* vol. 43, pp. 134-176, 2004.

Appendix 1.

Assignments of major Raman peaks

Some of the most used Raman bands found in cells fingerprint region and their assignments are presented here. This list was based on [46, 47, 104, 106-108, 200, 219] source references.

Abbreviations used:

T, thymine; G, guanine; A, adenine; U, uracyl C, cytosine;

Phe, phenylalanine; Tyr, tyrosine; Met, methionine; Cys, cystine; Trp, tryptophan; Lys, lysine

str., stretch; def, deformation; nar, unspecified non-aromatic side-chains, br., breathing mode, sym, symmetric; asym., asymmetric bk, backbone

Raman Band	Nucleic Acid	Proteins	Carbohydrates	Lipids
621		Phe (C-C twist)		
643		Tyr (ring str.)		
645		Tyr, Phe (C-C twist)		
650		Met, Cys (C-S str.)		
658 - 665	T, G	(C-S str.)		
667	T, G	Met, Cys (C-S str.)		
717-719				phospholipids ($CN^{+}(CH_3)_3$ sym str.)

729	A			
746	T (ring br.)			
757		Trp (ring str.)		
760		Trp (ring br.)		
7821	T, U, C (ring br.,RNA)			
785	U, C, T (ring br.)			
788	O-P-O (str. DNA)			
811	O-P-O (str. RNA)			
828	O-P-O (asym.str.)	Tyr (ring br.)		
854		Tyr, Trp (ring br.)		
893		C-C bk str.		
878		Trp (ring str.)		
888-895		Lys (C-C,C-N str.)		
937-955		α-helix, C-C bk str.	C-O-C ring	C-C-N sym str.
980		β-helix, C-C str.		=CH bend
1003		Phe (sym. ring br.)		
1033		Phe (C-H in-plane)	polysaccharides	phospholipids (CH_2CH_3 bend)
1044			glycogen	
1054		nar. (C-N,C-O str.)		

1060-1095	PO_2 str.	nar. (C-C str.)	C-O, C-C str.	Chain C-C str.
1128		C-N str.	C-O str.	C-C bk str.
1150 - 1160		C-C / C-N str.	C-C str.	
1176	C,G	Tyr (CH_3 bend)		
1209	A,T	amide III Phe, Trp (C-C_6H_5 str.)		
1220 -1300	T, A	Amide III , α- and β-helix structures		=CH bend
1320	G	Amide III α-helix ,CH def		
1342	G	CH def	CH def	
1373	T,A,G			
1420 - 1480	G,A	CH_2 def	CH_2 def	CH_2 def
1485	G, A, (ring br.)			
1480-1575		Amide II (CN str.)		
1578	G, A	Trp, (C=C ring str.)		
1607		Phe, (C=C ring str.)		
1617		Tyr, (C=C ring str.)		
1655- 1680	T, G, C (ring br.)	Amide I		C=C str.
1736				C=O ester str.